UNIVERSITY OF CALIFORNIA

Santa Barbara

Advancements in Monitoring Urban Heat and Vegetation Using Multi-Source Optical and Thermal Remote Sensing

A dissertation submitted in partial satisfaction of the

requirements for the degree Doctor of Philosophy

in Geography

by

Michael Alexander Allen

Committee in charge:

Professor Joseph McFadden, Chair

Professor Dar Roberts

Professor Charles Jones

June 2021

The dissertation of Michael Alexander Allen is approved.

_____

Charles Jones

_____

Dar Roberts

_____

Joseph McFadden, Committee Chair

May 2021

Advancements in Monitoring Urban Heat and Vegetation Using Multi-Source Optical and Thermal Remote Sensing

ACKNOWLEDGEMENTS

I would like to thank my advisor Joseph McFadden and my committee members Dar Roberts and Charles Jones, as well as my examination committee member Stuart Sweeney. Thank you for your multi-faceted and unwavering support in completing this dissertation and degree. I sincerely appreciate your patience, mentorship, and enthusiasm and owe much of my career as a scientist, geographer, writer, and programmer to you.

Special thanks to David Miller for fielding a wide range of tree-related questions and for frequently reminding me (explicitly and otherwise) that completing a doctorate is a marathon, not a sprint.

My sincere gratitude to numerous colleagues, collaborators, and friends for critique, academic and nonacademic discussion, and general support: Erin Wetherley, Chris Kibler, Sarah Shivers, Susan Meerdink, Alana Ayasse, Rachel Green, Fernanda Ribeiro, Gabriel Antunes Daldegan, Germán Silva, Clare Saiki, Conor McMahon, Susan Burtner, Amelia Pludow, Deanna Nash, Enbo Zhou, Cascade Tuholske, Glynn Hulley, Emily Schaller, Jon Wang, Niky Taylor, Rainer Hilland, Dimuth Kurukula, Scott Krayenhoff, and James Voogt. Thank you for the support (in all forms) that you contributed.

Finally, thank you to Kelly and our dog Luna for their tremendous support over the past three years. I'd like to also thank my family: Mom, Dad, Jane, Grandma, and Grandpa for your support and for only rarely asking how many years I had left in my PhD. Without doubt, I could not have done this without you.

I acknowledge and appreciate financial support from the International Association on Urban Climate, the American Geophysical Union, and the National Aeronautics and Space Administration for providing funding in the form of summer stipends and travel grants in support of this work.

VITA OF Michael Alexander Allen

May 2021

EDUCATION

PhD in Geography, University of California, Santa Barbara, 2021 (expected)
MSc in Geography, University of Western Ontario, 2017
BA in Environmental Ethics and Policy, University of Portland, 2015

PROFESSIONAL EMPLOYMENT

2019 Research Mentor, NASA Student Airborne Research Program Graduate
2014 Environmental Data Analyst Intern, Vigor Industrial LLC

PUBLICATIONS

Michael A. Allen, D. A. Roberts, and J. P. McFadden. "Reduced urban green cover and daytime cooling capacity during the 2012-2016 California drought." Urban Climate, 2021, 36.

K. Whaling, A. Der Sarkissian, N. Larez, J. Sharkey, **Michael A. Allen**, K. Nylund-Gibson. Reduced child maltreatment prevention service case openings during COVID-19. Child Maltreatment, in review.

J. Lai, W. Zhan, F. Huang, J. Voogt, B. Bechtel**, Michael A. Allen**, S. Peng, F. Honga, Y. Liug, and P. Dug. Identification of typical diurnal patterns for clear-sky climatology of surface urban heat islands. Remote Sensing of Environment, 2018, 217, 203-220.

Michael A. Allen, J. A. Voogt, and A. Christen. Time-Continuous Hemispherical Urban Surface Temperatures. Remote Sensing, 2018, 10(1), 3.

AWARDS

2018 NSF/ICUC10 Working Group Travel Grant
2017 American Meteorological Society, Excellent Oral Presentation Award
2017 IEEE Joint Urban Remote Sensing Event Travel Grant
2017 E.G. Pleva Award for Teaching Excellence, University of Western Ontario
2016 E.G. Pleva Award for Teaching Excellence, University of Western Ontario
2016 American Geophysical Union Dr. Edmond M. Dewan Young Scientist Scholarship

ABSTRACT

Advancements in Monitoring Urban Heat and Vegetation Using Multi-Source Optical and Thermal Remote Sensing

by

Michael Alexander Allen

The sensitivity of urban heat and urban vegetation to regional and global climate phenomena such as drought, heat waves, and climate change is a key concern in climate policy, urban planning, public health, and water and energy use. These signals are often difficult to resolve as urban climates vary at fine spatiotemporal scales and have complex interactions with land cover, surface morphology, and background climates. In this dissertation, I used multi-source airborne and satellite imagery from optical and thermal sensors to evaluate urban drought impacts on urban vegetation and climate and to investigate the efficacy of a novel spaceborne thermal sensor for fine-scale 24-hour monitoring of urban heat and its relationships with environmental and morphological drivers over the course of a day. In Chapter 1, I explored interactions between urban vegetation cover and urban heat during the 2012 to 2016 California megadrought in urbanized Los Angeles County, CA, USA using an 8-year time series of optical and thermal imagery. Over the course of the drought, I found strong spatiotemporally variant losses in green vegetation cover and complex coupling between losses of green cover and urban heat. In Chapter 2, I exploited the

unique orbital characteristics of the NASA ECOsystem Spaceborne Thermal Radiometer Experiment on Space Station (ECOSTRESS) sensor to develop composited 24-hour urban land surface temperature (LST) imagery for diurnal analysis of urban heat. I found that ECOSTRESS composites were suitable for resolving fine-scale (in both space and time) interactions between environmental drivers and urban LST over a full diurnal cycle as well as higher order features such as variability in heating and cooling rates based on land cover type. Finally, in Chapter 3, I used fine-scale urban surface morphology data from LiDAR with a parameterization of subpixel sun-surface-sensor geometry to extract facet-scale urban LSTs (e.g., wall, roof, road) from a 2.5-year time series of ECOSTRESS imagery. I then tracked the diurnal course of thermal anisotropy in urbanized Los Angeles County and New York City, NY, USA finding strong spatiotemporal variability in angular effects on urban LST as a function of surface-sensor geometry and surface morphology as well as separation in facet-scale LST based on facet orientation and time of day. These findings highlight the sensitivity of urban vegetation and climate to drought and potential tradeoffs between efforts to increase urban green cover and water conservation needs under a warming and drying climate. In addition, this work suggests that satellite platforms with atypical sampling regimes (e.g., from a precessing orbit) can provide data that is unique and appropriate for characterizing otherwise undersampled dimensions of urban thermal climates.

TABLE OF CONTENTS

Introduction

The temperature of the land surface is a key determinant of the surface energy balance and of turbulent exchanges of energy, mass, and momentum in the lowest layers of the atmosphere (Oke, 1982). Land surface temperature (LST) is also one of the most widely measured climate variables, with a host of satellite, airborne, and ground-based sensors retrieving image and point-like estimates of LST over a variety of spatial and temporal scales and extents. Remote measurements of LST have been used to quantify vegetation function (e.g., evapotranspiration, moisture stress), soil water content, heatwave intensity, and snow cover (Bergeron and Strachan, 2012; Roberts *et al.*, 2015; Hulley *et al.*, 2019; Still *et al.*, 2021). In cities, LST imagery has been used extensively to measure spatiotemporal variability in the urban heat island effect (UHI), to investigate relationships between land cover and temperature, to estimate outdoor water use, and to inform targeted urban heat solutions such as siting cooling centers and cool pavement/roof installations (Li *et al.*, 2013; Wetherley *et al.*, 2018; Reyes *et al.*, 2020). A key finding from approximately 40 years of remotely sensed study of urban thermal climates is the strong relationship between urban vegetation cover and urban surface and air temperatures (Weng *et al.*, 2004; Shashua-Bar *et al.*, 2011).

Vegetation provides one of the strongest controls on urban LST as it has direct and indirect effects on the surface energy balance. These effects come in many forms and can have both amplifying and mitigating effects on spatiotemporal contrasts in urban microclimates (Oke *et al.*, 1989). Vegetation directly affects the radiation budget, and in turn the energy balance, by modifying the surface albedo. This has variable effects on urban microclimates depending on background climate (e.g., temperate, continental, arid, etc.) and

the surrounding surface materials (Zhao *et al.*, 2014). For example, urban greening programs can result in an increase in overall albedo as dark asphalt is replaced with brighter grass and sparse tree cover (Oke, 1987). In contrast, in arid environments, managed vegetation can decrease the surface albedo as the albedo of leaves is generally lower than that of dry soils and as plant canopies shade the surface (Rose and Levinson, 2013). In addition, plant phenology can cause strong seasonal variability in vegetation albedo, resulting in seasonal shifts in the radiation budget for urban patches with vegetation cover (Zhang *et al.*, 2004). Vegetation also directly impacts the energy balance through evapotranspiration, which increases latent heat exchange, reducing subsurface heat storage and changes in surface/atmospheric temperatures. Increased surface water availability in vegetated urban patches (via irrigation, shading, and transportation of water by plant roots) is associated with higher soil moisture, which has further effects on thermal mass, albedo, and latent heat. Finally, plants directly modify near-surface turbulence by deflecting near-surface flow and decreasing wind velocity.

These examples highlight the complexity of plant-climate interactions in cities, which involve myriad processes at multiple spatial and temporal scales. Despite this complexity, it is generally accepted that urban vegetation cover has overall net positive effects for city inhabitants (Bolund and Hunhammar, 1999; McPherson *et al.*, 2017), particularly in reducing temperature extremes and minimizing microclimatic variability (e.g., spatial hot spots). Thus, there is considerable attention paid to the climate impacts of urban vegetation to understand and quantify impacts from green space on phenomena such as the UHI and to predict effects from planned vegetation plantings. In recent decades, much of this work has integrated

remotely sensed thermal imagery as well as methods for describing urban cover and morphology (Weng *et al.*, 2004).

The use of LST imagery in the study of urban climates has increased rapidly over the last decade (Zhou *et al.*, 2019) due to increases of computing power that have expanded the availability of analysis-ready datasets (e.g., Landsat disaggregated LST products, Moderate Resolution Imaging Spectroradiometer (MODIS) Terra/Aqua LST products). However, while significant strides have been made in using thermal remote sensing to understand the spatial and to some extent temporal (e.g., seasonal, climatological) dimensions of urban LST and plant-climate interactions, there remain significant gaps in both data and knowledge at other scales and in other dimensions (i.e., geometric). Thermal sensors (and indeed multispectral sensors) are primarily launched into polar orbits, which allow for consistent acquisitions at specific times of day (e.g., 10:30 local time for Landsat, 1:30 and 13:30 for MODIS Aqua) and with overpass cycles that scale inversely with spatial scale and image extent (16 days for Landsat at 60-120m, 0.5 days for MODIS at 1000m at nadir). Geostationary orbiting satellites add to this array with nearly continuous thermal imagery at coarse spatial scale (4000m at nadir for Geostationary Operational Environmental Satellite LST products) and near-global coverage, but they are generally too coarse for urban analyses without significant downscaling (Sismanidis *et al.*, 2015; Hrisko *et al.*, 2020). Satellite thermal datasets are generally paired with multispectral visible-shortwave infrared (VSWIR) imagery, which allows for simultaneous and synergistic analyses of form and function with well-integrated thermal/VSWIR image products. Planned earth observation missions such as the NASA Surface Biology and Geology (SBG) mission operate under the same paradigm with paired VSWIR (in SBG's case, hyperspectral) and thermal imagery on a polar orbit that emphasizes

fine spatial scale over fine overpass cycles and large spatial extent (Cawse-Nicholson et al., 2021).

These datasets allow for analysis of urban climates and plant-climate interactions within a specific spatiotemporal window. This window generally emphasizes either temporally coarse and spatially fine scale analyses (e.g., intra-city, seasons to years) *or* spatially coarse and temporally fine scale analyses (e.g., intra-city, weeks to months). Both of these windows allow for analysis at only at specific times of the day (or night), and thus they cannot characterize diurnal patterns without modeling and/or downscaling. Moreover, narrow-field-of-view satellite thermography neglects geometric analysis (i.e., 3-dimensional surface temperatures) because no fine-scale sensor exists with a large enough spatial extent to facilitate off-nadir sampling for multi-directional sampling. This geometric undersampling causes a sampling bias towards horizontally-oriented surfaces and results in LST imagery that is fundamentally incomplete (Voogt and Oke, 2003). Because of this sampling bias, sensor position and surface morphology exert a strong influence on LST imagery, which causes a directional dependence of urban LST termed effective thermal anisotropy.

Thus, while there is a wealth of data to examine phenomena at specific spatiotemporal scales and of specific surfaces (i.e., roads, roofs, tree canopy tops), the scope of the available data is arguably quite limited and with respect to the complete 3-dimensional form of the surface and outside of spatiotemporal sampling windows. The satellite record of urban LST cannot represent many phenomena of interest such as fine-scale heatwave impacts, facet-scale temperatures, and diurnal vegetation-LST relationships. These gaps represent a significant (and often unquantified) challenge for urban remote sensing and undermine the applicability and comparability of urban thermal remote sensing to in-situ and

model-based assessments of urban microclimates. In addition, it opens significant potential for unconventional satellite platforms, airborne sensors, and novel remote sensing missions (such as unmanned aerial vehicles) for investigating the gaps inherent in spatial, temporal, and geometric sampling of urban microclimates. I posit that novel remote sensors with unconventional orbital/sampling parameters are imperative for justifying the relevancy of thermal remote sensing of urban areas, for full integration with in-situ measurements, and for uncovering emergent and process-informed relationships that are hidden by gaps in sampling.

This work has two main goals. First, I used a suite of satellite and airborne multispectral and thermal imagery to investigate the drought sensitivity of urban vegetation cover and plant-LST relationships. Second, I use data from a new satellite thermal imager (ECOsystem Spaceborne Thermal Radiometer Experiment on Space Station, ECOSTRESS), which has highly unique orbital parameters and spatiotemporal sampling, to derive two novel remotely sensed analyses of urban LST: First, I used composited thermal imagery to derive fine-spatial resolution diurnal time series of LST imagery. Second, I developed a rasterized sun-surface-sensor parameterization to calculate sub-pixel field-of-view proportions and to investigate facet-scale temperatures and diurnal patterns of directional contrasts in urban LST (i.e., thermal anisotropy) as a function of urban morphology. These analyses are split into three self-contained chapters that are outlined below.

In Chapter 1, I tracked impacts from the 2012-16 California megadrought on vegetation fractional cover and plant-climate interactions in urbanized Los Angeles county, USA using monthly estimates of sub-pixel fractional vegetation cover derived from multispectral satellite imagery (Landsat 5/8) with satellite/airborne LST imagery at multiple scales (MODIS MOD12 8-day LSTE and MASTER HyspIRI LST). Excluding large highly

managed vegetation patches, I found strong coupling between vegetation fraction, precipitation, and LST. I observed variability in drought impacts based on plant functional type, with stronger impacts on grass compared to tree but more lasting impacts in tree-dominated areas. Finally, I found that drought impacts on urban vegetation and plant-climate interactions are sensitive to small inputs of precipitation and while mean impacts were largest in the most drought-affected years, fractional vegetation cover often reached pre-drought levels following precipitation events. Thus, I posit that consistent time-series sampling is needed for comprehensive assessment of drought impacts on urban vegetation and plant-climate relationships.

In Chapter 2, I used a time series of ECOSTRESS imagery to derive fine spatial resolution diurnal estimates of urban LST and to investigate diurnal relationships between LST, sub-pixel fractional land cover, elevation, surface height above ground, and other drivers of urban microclimates in urbanized Los Angeles county, USA. I then compared the shapes of ECOSTRESS derived diurnal urban LSTs with modeled and in-situ measured assessments of diurnal LST curves from the literature finding strong agreement. I conclude that ECOSTRESS composites can resolve fine-scale features such as the development of a cool island in densely built high rise neighborhoods and asymmetry between morning heating rates and afternoon cooling rates. I end Chapter 2 by suggesting optimal diurnal bin sizes and positing several research directions for exploiting new diurnally and spatially explicit LST information.

In Chapter 3, I employed a rasterized sun-surface-sensor parameterization to calculate sub-pixel field-of-view proportions for a time series of ECOSTRESS imagery. I used these along with high resolution LiDAR-derived digital surface models estimate sub-pixel

fractional wall LSTs at city scale in urbanized Los Angeles county, USA and New York City, NY, USA. I then investigated the diurnal and spatial dimensions of the directional dependence of remotely measured LST and its relationship with surface morphology. I end Chapter 3 by suggesting surface morphology and surface-sensor geometry thresholds for minimizing angular effects on fine scale LST imagery.

Chapter 1: Reduced urban green cover and daytime cooling capacity during the 2012-2016 California drought

With Dar Roberts and Joseph McFadden

Reproduced with Permission from Urban Climate

Allen, M.A., Roberts, D.A., McFadden J.P., 2021. Reduced urban green cover and daytime cooling capacity during the 2012–2016 California drought. Urban Climate. 36, 100768. https://doi.org/10.1016/j.uclim.2020.100768

Abstract

Urban vegetation mitigates elevated temperatures in cities. Drought presents an important challenge to urban heat mitigation as prolonged dry periods cause reduced evapotranspiration and losses of green vegetation cover. To measure drought impacts on the urban environment and climate, we used visible short-wave infrared satellite imagery acquired throughout the 2012–16 drought in California to quantify effects on fractional vegetation cover in the Los Angeles urbanized region. We then used satellite thermal imagery with repeat high-resolution airborne thermal imagery to measure how drought-induced reductions of green vegetation cover affected urban land surface temperature (LST) and the cooling effect of urban vegetation. Green vegetation cover declined from 29.3% in 2011 to 24.6% in 2016 in urban Los Angeles County. Over the drought, the annual mean daytime LST increased from 34.4 °C in 2010 to 37.1 °C in 2014. Despite the large-scale homogenization of LST, tree- and grass-dominated areas differed in how they were affected by the drought, with larger losses of vegetation fractional cover and stronger reductions in cooling effect for grass compared to tree-covered areas due to different plant physiological responses and irrigation changes. Results suggest that drought presents a challenge to urban resiliency, as vegetation is often a main component of heat mitigation plans.

1. Introduction

Vegetation is an important component of the urban environment and a primary driver of urban climate. Urban climates typically experience elevated temperatures due to the urban heat island effect (UHI), which is caused by modified surface geometry and thermal, radiative, and moisture properties in cities (Voogt and Oke, 2003). Urban vegetation is of particular importance to the study of urban heat because green vegetation (GV) cover mitigates extremes of air (Sailor, 1995; Grimmond *et al.*, 1996) and surface (Aniello *et al.*, 1995; Leuzinger *et al.*, 2010) temperatures. Cooling by vegetation is driven primarily by increased latent heat exchange from plant evapotranspiration and by shading of urban surfaces from plant canopies. These effects have been studied extensively using remotely sensed measures of vegetation cover and land surface temperature (LST), which have shown that the effects of vegetation on LST vary with plant functional type (Wetherley *et al.*, 2018), time of day (Crum and Jenerette, 2017), and background climate (Georgescu *et al.*, 2011; Bechtel *et al.*, 2019). However, while increasing green vegetation cover has been identified as an effective urban heat mitigation strategy, there is little research on the sensitivity of cooling by urban green spaces to climate perturbations such as drought.

Drought affects the extent, composition, and function of vegetation cover. These effects have been described for natural and agricultural ecosystems (e.g., Asner et al., 2016; Dong et al., 2019; Shivers et al., 2018). However, there are few studies of drought in urban environments (e.g. Miller et al., 2020; Quesnel et al., 2019). Drought effects on urban vegetation may differ from those observed in natural and agricultural systems due to a number of factors: (1) Urban vegetation is commonly mixed with large fractions of impervious and constructed materials (Arnold and Gibbons, 1996; Wetherley *et al.*, 2017).

(2) Cities are generally warmer and drier than their surroundings, owing to modified surface energy and water budgets (Oke, 1982). (3) Plant composition in cities is often different from the surrounding natural and agricultural ecosystems (Avolio *et al.*, 2019). (4) Urban vegetation is managed and frequently irrigated (Clarke *et al.*, 2013) such that the spatial and temporal patterns of vegetation greenness can become decoupled from those of precipitation (Chen *et al.*, 2015; Quesnel *et al.*, 2019). In addition, irrigation of urban vegetation has been shown to directly impact spatial patterns of urban heat (Reyes *et al.*, 2018).

The above factors have the capacity to mitigate or exacerbate drought effects in cities, but the net effects of drought on urban vegetation and climate are poorly known. In addition, these factors are highly variable across a city, which may lead to strong spatial heterogeneity of drought impacts on different areas and human populations within a city. Variability in drought impacts on urban vegetation is particularly important in the context of climate change and urban population growth, the combined effects of which are projected to exacerbate the urban heat island effect (UHI) across North American cities (Broadbent *et al.*, 2020). Urban green spaces are often proposed as a solution for urban heat as they provide both heat mitigation and other co-benefits such as storm water retention and recreational amenities (Bolund and Hunhammar, 1999). However, the efficacy of urban vegetation for providing those benefits may change under altered precipitation and temperature regimes due to drought or long term climate change.

The 2012–2016 mega-drought in California was marked by extremely low precipitation and elevated ambient temperatures (AghaKouchak *et al.*, 2014). The year 2014 was estimated to be the most severe drought in the region in the last ~1200 years (Griffin and Anchukaitis, 2014). In natural ecosystems in California, the drought caused record low

snowpack and widespread forest mortality (Berg and Hall, 2017; Tane *et al.*, 2018). In urban areas, drought caused losses of vegetation cover due to tree canopy dieback and mortality of trees and herbaceous vegetation (Miller *et al.*, 2020). In addition, the drought prompted policy responses including restrictions on urban water use and incentives for lawn removal and xeriscaping (Palazzo *et al.*, 2017).

To understand how urban vegetation and climate respond to drought, we examined the effects of the 2012–2016 California drought on GV fractional cover and LST in urbanized Los Angeles county, USA. We used airborne and spaceborne remotely sensed imagery to do the following: (1) Document changes in subpixel fractional cover of GV over the drought using a time series of Landsat imagery; (2) Measure drought-induced changes in urban LST and the cooling effect of urban green cover using Moderate Resolution Imaging Spectrometer (MODIS) Aqua thermal imagery; (3) Quantify differences in the drought responses of tree- and grass-dominated areas using MODIS/ASTER airborne simulator (MASTER) thermal imagery.

2. Methods

2.1. Changes in fractional cover of vegetation

To analyze drought-induced changes in fractional cover of GV, we compiled a cloud-free time series of Landsat 5 and Landsat 8 Analysis Ready Data (ARD) Level-2 surface reflectance imagery covering 2011 and 2013 through mid-2019. The year 2012 was omitted from this analysis as it represents the gap between the operational periods of Landsat 5 and Landsat 8. Landsat 7 data from 2012 were not used because of missing data due to the failure of the instrument scan line corrector. After filtering for cloud cover and data quality, a total

of 80 Landsat 5 and 8 images were available for use in the study. The stack of images was then clipped to the study area (see "Study area and climate"), resulting in a dataset covering 1,876 km^2 of the urbanized area of the Los Angeles basin. A workflow diagram showing data acquisition, processing, and analysis steps is shown in Figure 1.

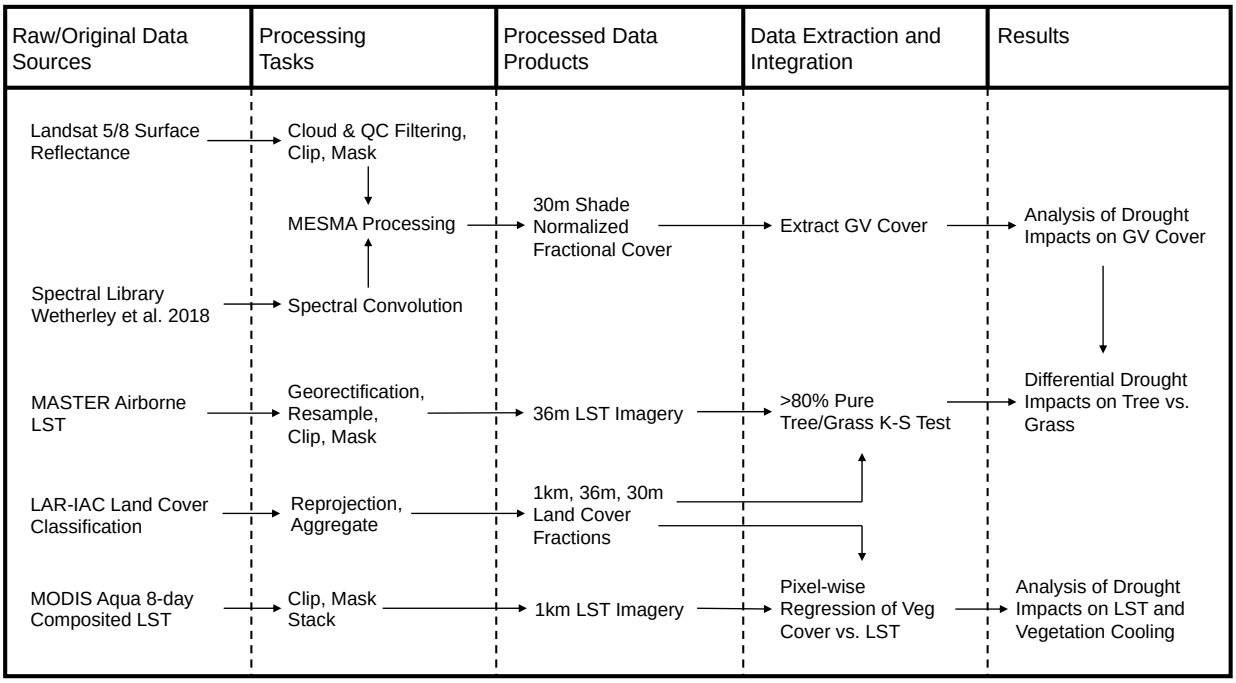

Figure 1: A summary of the workflow.

To derive fractional cover, we used Multiple Endmember Spectral Mixture Analysis (MESMA), which decomposes each pixel into its fractional areal components based on a comparison of a pixel's spectra against a library of representative spectra (or endmembers) of the target classes (Roberts *et al.*, 1998). We used a spectral library generated from Airborne Visible / Infrared Imaging Spectrometer (AVIRIS) imagery convolved to the band passes of Landsat Thematic Mapper (Landsat 5) and Landsat Operational Land Imager (Landsat 8) (Wetherley *et al.*, 2018). We chose this library because it was composed of spectra from the

same domain as our study area that were acquired near the midpoint of the drought in August 2014.

Using MESMA, we quantified sub-pixel fractions of GV, non-photosynthetic vegetation (i.e. senesced and dead plant material), soil, road, roof, and rock for each cloud-free Landsat image (Roberts *et al.*, 1993). Each pixel was modeled as the combination of up to three endmembers, plus shade. The results were shade normalized by subtracting the shade fraction and scaling the sum of all other fractions within each pixel to 100% (Dennison and Roberts, 2003). We then extracted the GV fractions for each pixel and averaged them over the study area to track drought-induced change in urban GV cover.

The use of MESMA-derived fractional cover has several advantages over traditional remote sensing methods for tracking vegetation status and vegetation–LST relationships. Per-pixel GV fraction represents an area on the ground within a given pixel. Spectral indices, such as the Normalized Difference Vegetation Index (NDVI) which is frequently used to quantify vegetation abundance in urban areas, represent ratios of reflectance rather than physical areas, and spectral indices do not scale linearly in areas with high levels of heterogeneity. In addition, NDVI is strongly influenced by plant functional type and it saturates in areas with high leaf area index (LAI) (Gu *et al.*, 2013). However, by estimating sub-pixel fractional cover for a variety of spectrally distinct land cover types, MESMA can be used to separate a change in GV cover from a change in non-vegetated land covers and it is robust to differences in LAI among plant functional types (Miller *et al.*, 2020). Changes in GV cover may be caused by direct effects of drought on plant growth and survival (e.g., increased vapor pressure deficit and reduced soil moisture) as well as human responses (e.g., landscape irrigation restrictions and lawn replacement programs). By quantifying GV cover

change over time, our analyses capture the net effect of these direct impacts and human responses over the course of the drought, which we then relate to micro-climatic effects on urban LST.

2.2. City-scale land surface temperature changes by time and vegetation type

To analyze drought-induced changes in urban LST and the cooling effect of urban vegetation, we used thermal imagery from MODIS and MASTER. MODIS satellite imagery were acquired from the Aqua platform with a daily overpass at ~13:30 PST. We used MODIS 8-day composited LST products (MYD11A2 Version 6) at 1 km spatial resolution from 2010 through summer 2019. The 8-day composited product was used to minimize anisotropic effects and effects from synoptic variability (by averaging over multiple view geometries and weather conditions). The MODIS data provided a coarse spatial resolution, but fine temporal resolution, view of drought induced changes in urban LST and cooling from urban green space.

MASTER airborne images, providing finer spatial resolution measurements of LST, were acquired as a part of the NASA HyspIRI Preparatory Campaign (HPC, Lee et al., 2015) with flights over the Los Angeles basin three times per year from 2013 to 2015 (spring, early summer, and late summer) and once per year from 2016 to 2018 in summer. MASTER imagery was acquired within +/– 3 hours from solar noon at a spatial resolution of 36 m. MASTER thermal imagery were processed to LST using temperature-emissivity separation by NASA Jet Propulsion Laboratory and clipped to the study. The accuracy of MASTER imagery acquired as a part of the HPC was estimated to be ≤0.33 K, with the range of per band precision estimated via noise equivalent differential temperature (NEdT) as 0.15–0.74

K (Wetherley *et al.*, 2018). To process the imagery, we orthorectified and resampled each MASTER image to 36 m using nearest neighbor resampling. We then corrected minor co-registration errors (maximum 2–3 pixel offset per image) by georectifying each image to 1 m National Agricultural Imagery Program (NAIP) imagery acquired in 2014 that was aggregated to 36 m.

The high spatial resolution of the MASTER LST imagery allowed for analysis of nearly pure (>80%) grass- and tree-covered pixels, which would not have been possible with coarser MODIS LST imagery due to the patchiness of urban vegetation. We selected a threshold of 80% pure composition for comparing urban vegetation types because it was the best compromise between homogeneity within the pixel and the number of samples of each type that would be available for analysis. Fine scale LST imagery also allowed for direct spatial comparison of LST against maps of GV fractional cover from Landsat by resampling the Landsat GV maps to 36 m using bilinear interpolation.

To examine drought impacts on LST of tree and grass covered areas, we used a fine resolution land cover classification derived from orthophotography (LAR-IAC, see "Urban vegetation types" below) to identify and extract LSTs of >80% pure tree and grass covered pixels. We used a Kolmogorov-Smirnov (K-S) test to examine differences between distributions of tree and grass LSTs over the drought, with higher values indicating larger differences between the two distributions of LST. To compare K-S values with changes in urban surface cover, we extracted mean fractional GV cover for the same >80% pure tree and grass pixels in each Landsat image.

2.3. Urban vegetation types

To analyze drought-induced changes in the cooling effect of urban green cover, we used a high spatial resolution (~0.22 m) land cover classification generated by Los Angeles Region Imagery Acquisition Consortium (LAR-IAC) near the midpoint of the drought (2014) (LAR-IAC, 2015). The classification contains three vegetation cover classes (tree, grass/shrub, and tall shrubs) that represent green land cover during non-water-limited periods, as well as classes for bare soil, water, and three impervious cover classes. The LAR-IAC classification was used to generate maps of sub-pixel green cover the same spatial resolutions as the Landsat, MODIS, and MASTER imagery. To generate maps of fractional cover for each of the green cover classes, the classification map was aggregated to the target resolution by dividing the number of pixels of the target class by the total number of pixels. Maps of fractional land cover of tree, grass/shrub, and all vegetation (the sum of tree and grass/shrub cover fractions) were used to quantify changes in the cooling effect of urban green cover over the drought as vegetation responded to reduced precipitation.

2.4. Quantifying Land surface cooling per unit change in green cover

To assess the cooling effect of urban green cover, we computed linear regressions of pixel-level LST (from MODIS or MASTER) versus fractional green cover (from LAR-IAC). The slope of this regression represented the amount by which LST decreased as green cover fraction increased. By regressing LST values observed during the drought against a fixed map of tree and grass cover, we were able to track drought-induced changes in the daytime cooling effect of urban green cover resulting from changes in both the form of urban green space (e.g. reduced vegetation cover, expressed as reduced GV cover fraction derived from

Landsat) and function (e.g. reduced evapotranspiration, expressed in elevated LST measured via MODIS and MASTER).

2.5. Study area and climate

We defined a study area as the portion of MASTER Line 7 of the NASA-HPC Southern California flight box (Lee *et al.*, 2015) that fell within the boundaries of Los Angeles county (Figure 2). This area covered the majority of urbanized Los Angeles County. Large bodies of water and areas outside of the urbanized boundary were excluded from the study area. Tree cover in the region is dominated by evergreen trees, with deciduous trees comprising 22% of total tree cover within the city of Los Angeles (Nowak *et al.*, 2011; Litvak *et al.*, 2017).

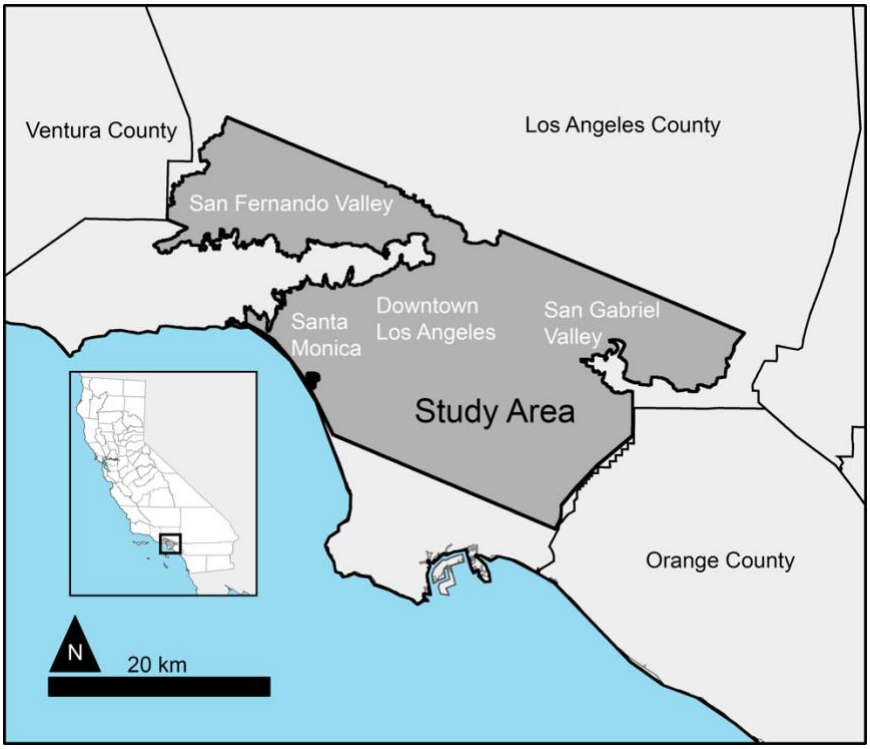

Figure 2: The Los Angeles County urbanized study area. The study area is bounded by the intersection of Los Angeles County with line 7 of the NASA-HPC Southern California flight box. Light grey shading indicates urbanized land cover in 2010 (Courtesy of ESRI, USGS, and the US Dept of Commerce). Non-urbanized areas within Los Angeles county (e.g. the Santa Monica Mountains) were excluded by manually digitizing neighborhood boundaries.

Data from the three imagery sources covered a range of pre-drought, drought, and post-drought conditions. The timing of Landsat, MODIS and MASTER imagery relative to drought can be shown using the Palmer Drought Stress Index (PDSI; Figure 3). PDSI estimates relative dryness using precipitation and temperature data with a range of values between –10 (dry) and +10 (wet) (Palmer, 1965).

Landsat 5 imagery covered pre-drought conditions in 2011. Landsat 8 acquisitions began in early 2013 and continue through mid-2019 through a range of drought conditions.

PDSI decreased from 2012 through late 2014 indicating increasing drought stress. PDSI varied seasonally with negative spikes during the summer months and positive spikes in the winter months from small inputs of precipitation. PDSI reached a negative peak in June 2014 with a gradual positive increase in PDSI in 2015 and early-to-mid 2016. Higher than average precipitation in late 2016 and early 2017 caused a strong decrease in drought severity, with PDSI increasing to nearly zero in February 2017. A lack of precipitation and high temperatures in mid-to-late 2017 and 2018 caused a strong decrease in PDSI. In terms of PDSI (and other indicators of climatological and hydrological drought stress), the drought ended in January 2019 after heavy rain events in Southern California in December 2018 and January 2019. January 2019 represented the first time that PDSI was above zero (indicating wet conditions) in seven years.

The MODIS 8-day composited images were continuous and covered pre-drought, drought, and post-drought conditions. We included 2010 in the MODIS time series to provide enough time to remove seasonal cycles using an annual moving window average. MASTER image dates began in 2013, a year after the start of the drought, and captured a range of drought severities and the brief drought recovery in 2017.

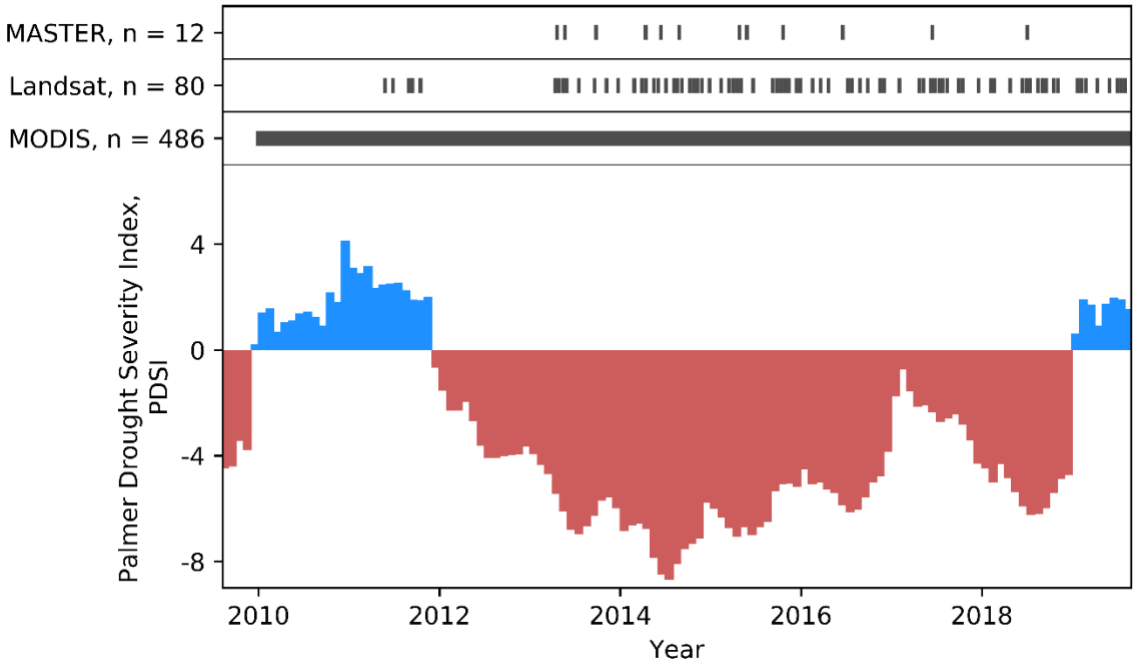

Figure 3: Monthly Palmer Drought Severity Index (PDSI) for the South Coast drainage basin from 2009 through mid-2019. Blue shading indicates relatively wet conditions and red shading indicates relatively dry conditions. MASTER, Landsat 5 and 8, and 8-day MODIS acquisition dates are shown as ticks in the upper third of the figure. The ticks represent the cloud-free, quality-checked data used in this analysis.

3. Results

3.1. Reduced green vegetation fraction during drought

Low precipitation and elevated temperatures during the drought period from 2012–2016 caused a reduction in sub-pixel GV fractional cover (Figure 4A). In addition, mean GV fractions across Los Angeles varied over a larger range during the drought years, likely due to a combination of direct drought impacts in unirrigated green spaces, reduced summertime irrigation from outdoor water use restrictions, and land cover change from lawn replacement

programs. Mean annual GV fraction for the study area decreased from 29.3% in 2011 to a minimum of 24.6% in 2016. This corresponded to a change of GV covered area from 549.71 km^2 in 2011 to 461.54 km^2 in 2016, a net loss of 88.17 km^2. Mean GV fraction increased by 2.0% between 2016–17 in response to stronger winter precipitation. Drought conditions persisted through 2018, resulting in a 2.3% reduction in mean GV fraction. By 2019, mean GV fraction had nearly returned to levels observed before the start of the drought (28.6%).

We observed a positive log relationship between GV fraction and accumulated precipitation over the preceding 3 months (Figure 4B, $y = 0.008\log(x)+0.27$, $r2 = 0.43$). After periods of rainfall, GV fraction reached an asymptote representing full coverage of GV in the areas available for plant growth in the urban region. Maximum mean GV cover over the time series was 31.9%, observed in February 2015 following a total of 12.6 cm of rainfall that occurred in December 2014 and January 2015. Our estimate of maximum GV cover is consistent with results in McPherson et al., (2017) who estimated that Coastal Southern California cities had 13.8% tree cover and that 42% of residential sites in California had trees, which would imply a total vegetation cover fraction of 32.9%. The maximum GV cover fraction approached the total plantable area in the Los Angeles study area (34.0% green land cover estimated from the LAR-IAC classification).

Drought-induced losses and post-drought recovery in GV fraction varied markedly across Los Angeles (Figure 5). The inland San Fernando Valley lost 5.3% GV cover between 2011–2016 and gained 2.4% between 2016–2019. In contrast, regions <10 km from the coast lost 3.1% GV cover between 2011–2016 and gained 3.6% between 2016–2019. This indicates that the San Fernando Valley had a net loss of –2.9% GV cover from 2011–2019 while coastal regions had a net gain of +0.5% GV cover. These net changes are relative to

average GV cover in 2011 of 34.6% for the San Fernando Valley and 25.4% for coastal regions. A number of factors potentially contributed to the disparity in GV loss/gain including (1) lower humidity and higher ambient temperatures in inland areas, (2) spatially heterogeneous water conservation, and (3) incentivized lawn removal programs (Pincetl *et al.*, 2019).

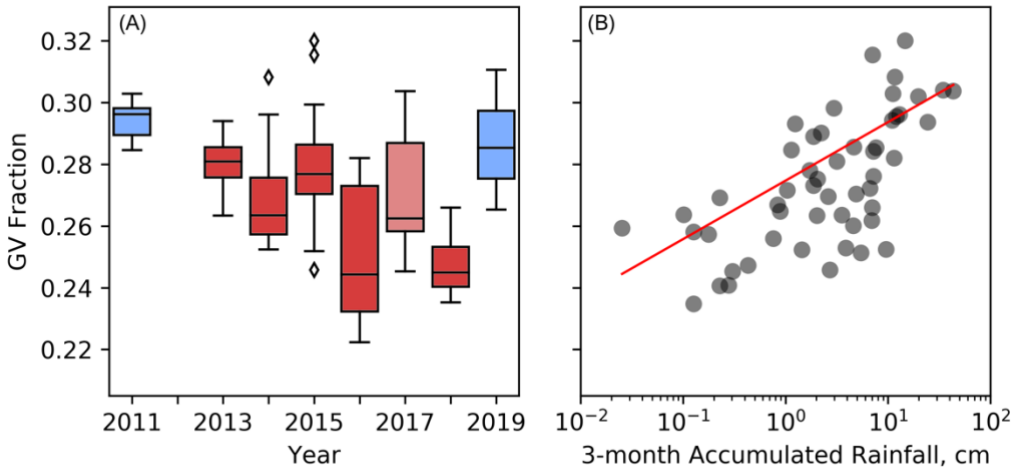

Figure 4: Trends in GV fractional cover over the drought period. (A) Sub-pixel fractional cover of GV from Landsat in urban Los Angeles County for all image dates in 2011 and January 2013 to August 2019. Box colors represent annual average PDSI, with blue PDSI>0 indicating no drought, and light red 0>PDSI>–5, and red PDSI<–5 indicating drought conditions. Whiskers represent 1.5 times the interquartile range and diamonds are outliers. (B) Mean GV fraction for each Landsat image date (n = 80) plotted against the sum of precipitation over the preceding three months.

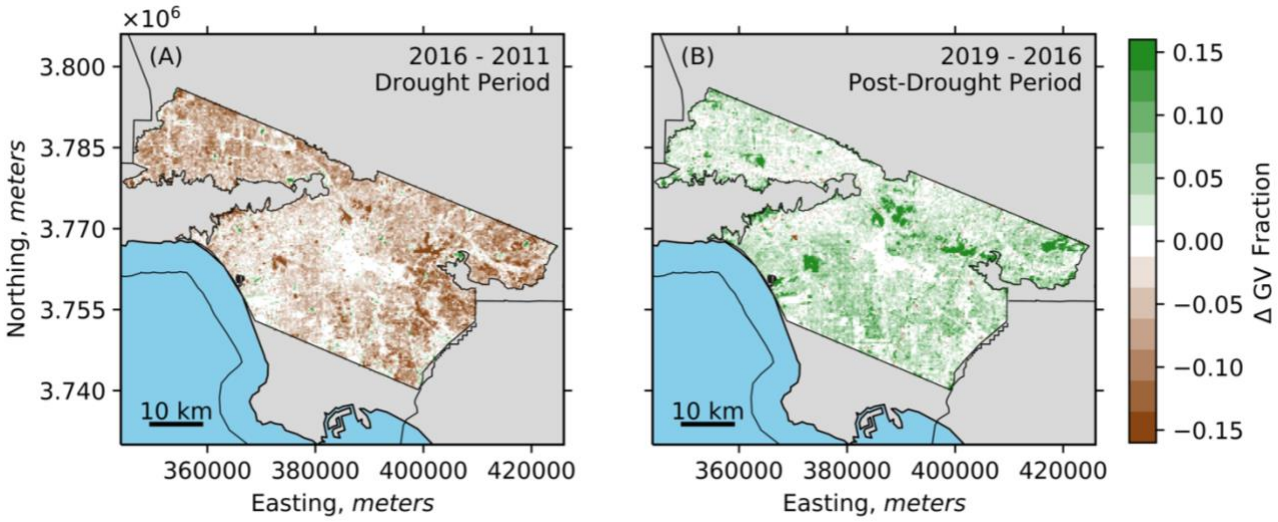

Figure 5: Change in mean annual GV fractional cover from 2011 to 2016 (A) and from 2016 to 2019 (B). GV cover was derived from Landsat 5 and 8 imagery and averaged for each year. Results are aggregated to 300m for map display.

3.2. Reductions in the cooling effect of urban green space at the scale of the urban region

Averaged across the urban region, the drought had a warming effect on urban LST and decreased the range of observed LSTs. Figure 6 shows drought impacts on the mean and standard deviation of LST and on the cooling effect of urban green cover. Results in Figure 6B–F were smoothed using an annual moving window average to remove seasonal cycles. Mean daytime annual LST in urban Los Angeles County increased by 2.7°C, from 34.4°C in 2010 to 37.1°C in 2014. The standard deviation of LST decreased by 0.3°C, from 2.6°C in 2010 to 2.3°C in 2014. In 2018, after the drought had ended, mean LST decreased by 1.0°C to 36.1°C.

We estimated the cooling effect of urban green cover as the average difference in LST between pixels with 0% and 100% tree, grass, and vegetation (tree plus grass) land cover from the 1km aggregated LAR-IAC fractional cover maps. This is expressed as the

slope of a linear regression between land cover fraction of a given class and LST for each MODIS image (Figure 6D–F). Larger negative slopes indicate that there was a stronger cooling effect associated with increasing per-pixel vegetation, tree, or grass cover. Land cover fractions estimated from LAR-IAC are fixed through time and represent cover during moist conditions. By using fixed land cover fractions, these results captured changes in cooling from both reduced plant evapotranspiration and land cover change (e.g. tree and grass mortality).

To compare the distributions of cooling from all vegetation, tree, and grass cover in pre-drought (2010) and drought maximum (2016) years, we extracted slopes of LST vs. vegetation cover fraction (and grass and tree only) for both years (Figure 7). Each year is represented by 46 slope values, which represent the average difference in LST per unit increase in fractional land cover of vegetation, tree, or grass (i.e. the average difference in LST between a pixel with 0% vegetation cover and a pixel with 100% vegetation cover) for each 8-day composited MODIS LST image. In both 2010 and 2016 for all vegetation cover and for trees, the range of observed cooling effects were approximately normally distributed. However, for grass, both 2010 and 2016 had right-skewed distributions suggesting that cooling from grass had a large amount of seasonal variability, with strong cooling observed during the wet winter months and a gradual weakening in cooling during the summer and fall dry down. This skewed pattern was less apparent in 2016 indicating more consistently weak cooling from grass during the drought and weaker peak cooling during the winter months.

We calculated the mean annual cooling effect for each year (and each green cover type) as the average of the 46 slope values in each year. The mean annual daytime cooling effect of all green cover combined decreased from –0.37°C per 10% increase in green cover

prior to the drought in 2010, to –0.30°C per 10% increase in green cover at the peak of the drought in 2016. The difference in mean annual cooling between 2010 and 2016 was significant (Wilcoxon signed-rank test, $z = –4.91$, $p < 0.01$, $n = 46$). This represented a 18.9% relative decrease in the cooling effect of all green cover at the peak of the drought.

Tree covered areas had twice as large of a cooling effect on LST compared to grass cover throughout the drought. Between 2010 and 2016 the annual mean cooling effect of tree cover fell from –0.52°C per 10% increase in tree cover to –0.44°C per 10% increase in tree cover ($z = –3.38$, $p < 0.01$, $n = 46$). Cooling from grass cover changed from –0.25°C per 10% increase in grass cover in 2010 to –0.19°C per 10% increase in grass cover in 2016 ($z = –5.03$, $p < 0.01$, $n = 46$). Thus, annualized daytime cooling from tree cover declined by 15.3% compared to 25.0% for grass cover. Grass cover responded more quickly to short term additions of precipitation during the drought period, with large increases in grass cooling effect after rain events in late 2014 to early 2015, and early 2017.

While mean LST across the study area approached pre-drought levels in 2019, the cooling effect of vegetation remained low, with only a 3.6% increase in the cooling capacity of green cover between January 2018 and January 2019. The lag in post-drought recovery of vegetation cooling was much larger for tree cover, which increased by only 0.6% over the same time period, compared to a 7.9% increase for grass cover.

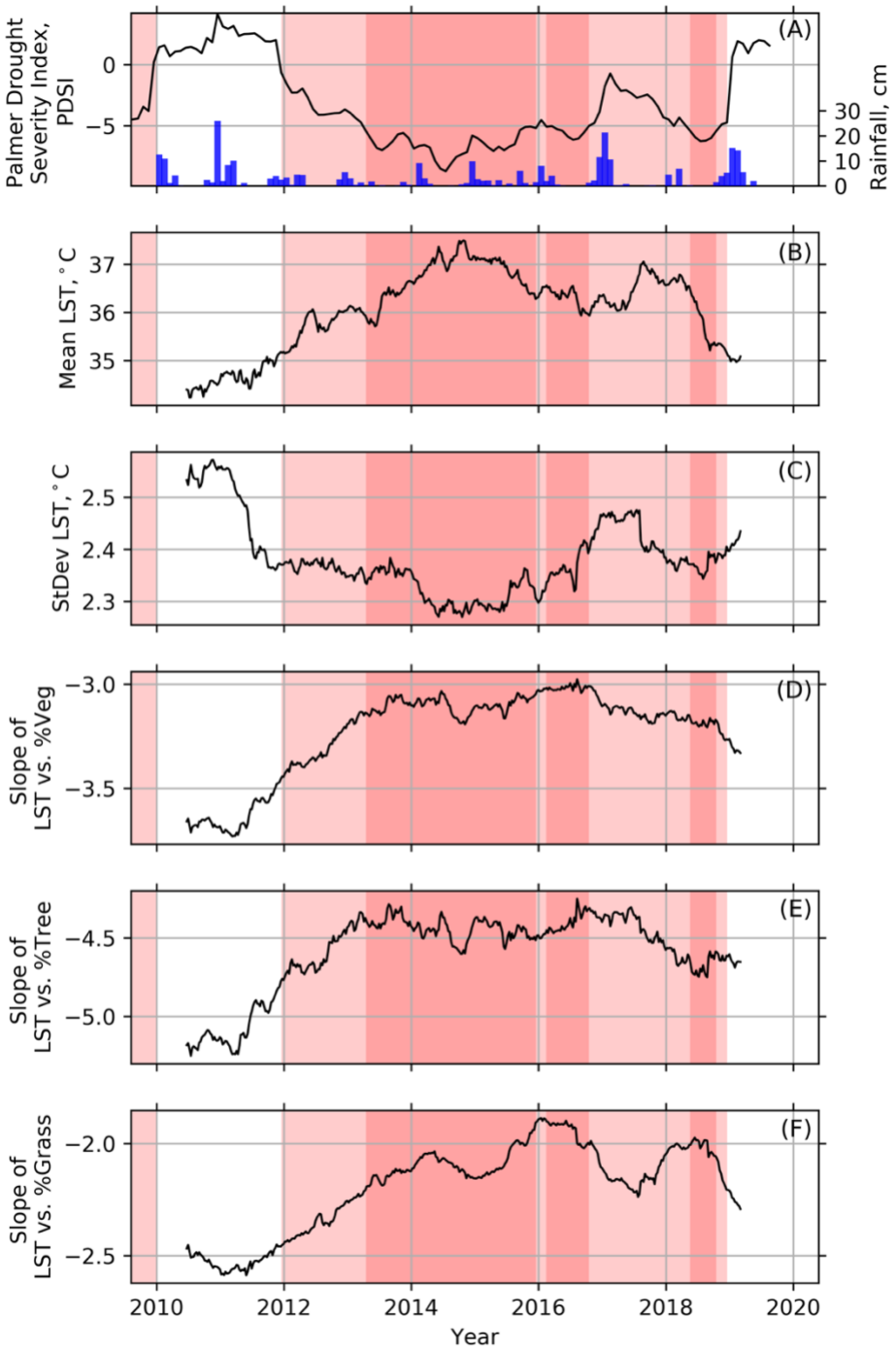

Figure 6: Urban-region-scale drought impacts on urban LST and cooling from urban green space. (A) Drought severity expressed in terms of PDSI for the South Coast drainage basin and monthly precipitation measured at the Los Angeles Civic Center retrieved from the

California Department of Water Resources. (B–C) Mean and standard deviation of MODIS LST over the time series. (D–F) Average slopes of a linear regression of per-pixel vegetation, tree, and grass cover from the LAR-IAC land cover classification against per-pixel LST. Results in (B–F) are smoothed using an annual moving window average to remove seasonal variability. Light shading indicates periods in which –5 < PDSI < 0, indicating mild to moderate drought. Dark shading indicates periods in which PDSI < –5, indicating severe drought.

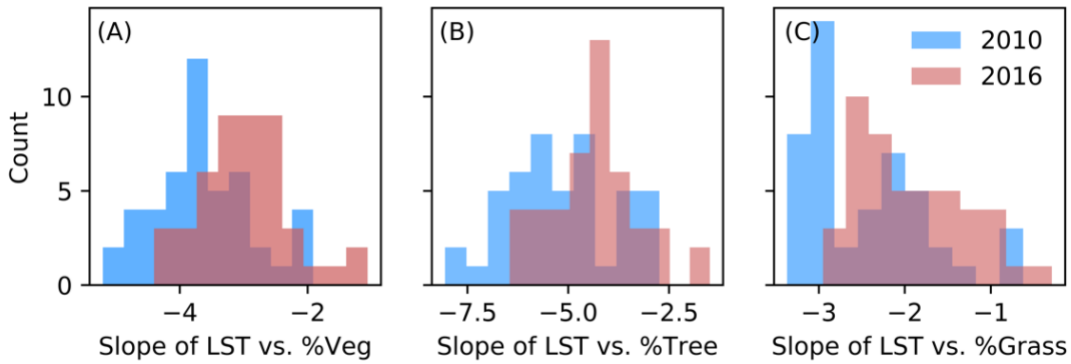

Figure 7: The distribution of slopes of LST vs. green cover for pre-drought (2010) and drought (2016) years for (A) all vegetation, (B) tree, and (C) grass. All differences were statistically significant at $p < 0.05$.

3.3. Differential drought impacts on tree- and grass-dominated areas

Using high resolution MASTER thermal imagery it was possible to further examine differences in drought impacts on LSTs between nearly pure (>80%) tree- versus grass-covered pixels. Results of a Kolmogorov-Smirnov (K-S) test comparing distributions of tree and grass LSTs are shown in Figure 8A. For all images, the distributions of tree and grass LSTs differed significantly ($p < 0.01$), but the magnitude of the LST difference between the

two vegetation types varied over the course of the drought. As drought severity and duration increased, LSTs of grass and tree diverged, resulting in higher spatial heterogeneity of LST within vegetated areas of the urban region. This occurred despite a decrease in the standard deviation of LST at the scale of the urban region as a whole across all vegetated and non-vegetated land cover types.

The difference between tree and grass LSTs increased following differential losses and gains of fractional GV for the two vegetation types. This is shown in Figure 8B using a comparison GV cover for nearly pure tree and grass pixels at each measured time point during the drought against the mean GV cover for the same pixels in 2011 (representing baseline annualized pre-drought conditions). Winter (wet season in our Mediterranean climate zone) GV cover during drought years was comparable to non-drought years, however the decline in GV cover in subsequent months going into the summer dry season was larger during drought years. Variability in GV cover was greater for grass- than tree-covered areas, particularly following winter precipitation events, which caused large spikes in GV cover of grass. Tree cover in the study area was dominated by evergreen trees (McPherson *et al.*, 2017) which do not have a winter leaf-off period and experience relatively small increases in GV cover following winter rainfall.

The difference between distributions of tree and grass LST reached a peak in late summer 2015. During this time, PDSI was between –6.5 and –7, indicating some of the driest conditions over the drought, that were slightly moderated by late season rainfall which likely buffered summer losses of tree GV cover. As a result, late-summer tree GV cover was 5–7% higher than the mean observed in 2011, while grass was 6–12% lower than the mean

observed in 2011. Divergence in GV cover for tree and grass relative to the 2011 baseline likely caused strong deviation between LSTs for the two vegetation types.

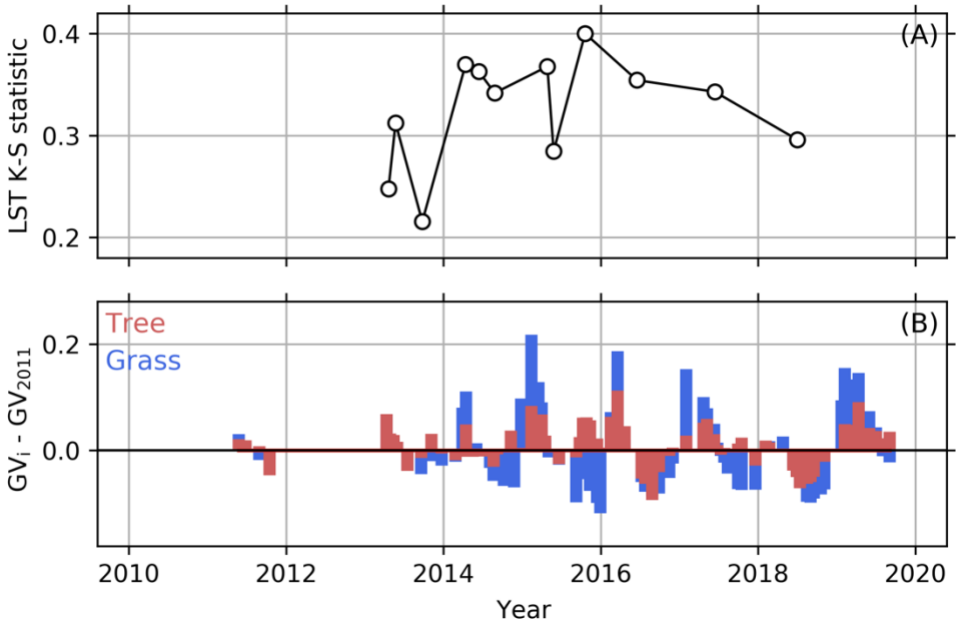

Figure 8: Differences between distributions of tree and grass LSTs and tree and grass GV fractional cover relative to pre-drought levels. (A) Kolmogorov-Smirnov (K-S) statistic calculated from nearly pure (>80%) tree and grass LSTs. Increasing K-S statistic indicates a larger difference between the two distributions of LST adjusting for differences in the mean and range of LSTs observed in each image. Each dot represents a single image and tests were calculated independently for each image. The lines connecting the image K-S values are for visualization only. (B) Difference between mean pre-drought GV cover in 2011 and mean GV cover for each individual Landsat image for >80% pure tree and grass pixels. Note: Bars are not stacked.

4. Discussion

The 2012–2016 mega-drought in California caused a decline in GV cover and a decrease in the cooling effect of urban green space across the Los Angeles region. Our results are consistent with the expectation that declines in GV cover caused a shift in partitioning of net radiation in favor of sensible heat, which resulted in increased daytime LST and near-surface air temperatures (Best and Grimmond, 2016). This shift in the surface energy balance from land cover change was likely exacerbated by decreased irrigation during the drought, which was found to strongly influence evapotranspiration and air temperatures at the city scale in Los Angeles (Vahmani and Hogue, 2015).

GV cover did not decline linearly with drought duration or drought severity (i.e., PDSI). We observed that all drought years had periods with winter GV fractional cover that was in the range of pre-drought levels, while summertime GV cover was often much lower compared to non-drought years, thus increasing the annual range of mean GV cover. GV cover was particularly variable for grass-dominated areas, which experienced large spikes in GV cover following winter rain events during the drought. Despite these occasional winter rain events, water storage remained at historic lows through early 2016 and irrigation restrictions were not relaxed until June 2016 (Mitchell *et al.*, 2017); therefore, we assume that sub-annual increases in GV fractional cover between 2012 and 2016 were driven largely by greening after precipitation, rather than by increases in irrigation or new planting.

Drought induced losses and post-drought gains of fractional GV cover showed markedly different spatial patterns. This was particularly apparent in the contrast between inland and coastal regions of the study area. We observed strong GV cover losses and weak

post-drought gains in inland areas. In contrast, coastal regions showed a net gain in GV cover between 2011–2019. This disparity most likely had a number of causes: (1) inland areas had higher air temperature and lower humidity, increasing the soil moisture deficit and causing stronger GV losses. (2) Mini et al., (2014) found income driven differences in irrigation in the city of Los Angeles, with higher irrigation rates in the more wealthy, coastal regions of Los Angeles. (3) The Metropolitan Water District of Southern California incentivized turf replacement programs during the drought. These programs were more successful in inland areas, particularly in the San Fernando Valley (Pincetl *et al.*, 2019). These results suggest that drought may have lasting impacts on the urban environment not only from direct drought induced losses of GV cover, but also from public policies and individual decisions in response to drought.

To understand how increases in mean annual LST across the Los Angeles region were influenced by losses of GV cover and reduced plant evapotranspiration we calculated the mean annual cooling effect of green space aggregated across the urban region for 2011 and 2016. To calculate the aggregated annual cooling effect of vegetation in 2011 we multiplied the mean cooling capacity of green cover (–0.37°C per 10% increase in green cover) by the mean annual GV cover (29.3%) in urban Los Angeles County, yielding an annualized cooling effect of 1.1°C under pre-drought conditions. In other words, GV cover in 2011 was responsible for 1.1°C of LST cooling averaged over urban Los Angeles County over all seasons. In 2016, this aggregated cooling effect had decreased to 0.7°C. This represents a 0.4°C reduction in daytime cooling from green space averaged over the year and aggregated over the study area. This is consistent with results in (Vahmani and Ban-Weiss, 2016), who used a regional climate model to estimate climate impacts of widespread

adoption of xeriscaping in Los Angeles, resulting in 1.9°C warming of summertime near-surface air temperatures during the day. This is proportionally consistent with our annualized reduction in daytime cooling (0.4°C) from more modest changes in green vegetation cover and plant function (in spite of differences in domain and temperature type).

Over the same time period, mean LST increased by 2.7°C, from 34.4°C in 2010 to 37.1°C in 2014. Thus, of the 2.7°C increase in mean LST between 2011–2016, we infer that 0.4°C was a direct result of decreased GV cover. The remaining 2.3°C likely occurred as a result of increased synoptic scale temperatures (Di Lorenzo and Mantua, 2016) and reduced plant evapotranspiration in vegetation patches that remained green.

While LSTs across the Los Angeles urban region became more spatially homogenous over the course of the drought, the LSTs of nearly pure tree- and grass-covered pixels diverged, thus making the LST within vegetated areas more spatially heterogeneous. Two factors contributed to the differences in drought impacts we observed for tree compared to grass cover. (1) Trees cool by both evapotranspiration and by shading the surface, whereas grasses only cool via evapotranspiration (Shashua-Bar *et al.*, 2011). This difference in cooling pathways accounts for both the larger cooling effect and greater resilience in cooling observed for trees. (2) By virtue of deeper rooting depth and larger biomass than grass, trees are more likely to withstand severe drought conditions and still maintain evapotranspiration, even if at reduced rates, whereas lawns senesce or die (Bijoor *et al.*, 2012; Miller *et al.*, 2020). Drought would have reduced tree evapotranspiration rates, but likely had less of an effect on canopy structure and tree shading. In contrast, grasses cool the surface via evapotranspiration exclusively, without shading effects on other cover types. The evapotranspiration rates of many turfgrasses decline to near zero in as little as four weeks

without irrigation (Qian and Fry, 1997). These factors would have contributed to strong drought induced variability in GV cover and LST for grass contrasted with relatively resilient tree GV cover and LST.

The timing of GV cover losses and reductions in the cooling effect of grass cover indicate that water conservation actions may have exacerbated drought impacts on urban vegetation and surface climate. California declared a state of emergency due to drought in January 2014. In April 2015, the State Water Board issued a mandatory 25% reduction in urban water use (Gonzales and Ajami, 2017; Mitchell *et al.*, 2017). Following the urban water use restriction, mean GV cover fell by 3.0% from 27.9% in 2015 to 24.9% in 2016, the largest year-to-year decrease in the time series. This also coincided with a period of strong differences in drought responses of tree and grass GV cover. Tree cover in mid 2015 to late 2015 was 5–7% higher compared to its mean cover in 2011, while grass cover was 6–12% lower compared to 2011 (Figure 8). Those diverging responses caused a peak in the difference between the distributions of tree and grass LST in late 2015. In addition, the cooling effect of grass cover fell by 11.0% from March 2015 to January 2016, constituting about 40% of the overall drought induced loss in grass cooling. Reduced GV cover at scale of the urban region, differential losses of GV cover for grass dominated areas, and reductions the cooling effect of grass that we observed during that period, were consistent with the results of a widespread reduction of outdoor water use.

Droughts in the southwest United States are often accompanied by elevated temperatures (AghaKouchak *et al.*, 2014). Our analyses showed that a loss of cooling from urban green spaces may have contributed to elevated ambient temperatures during drought. This additionally suggests that drought stricken cities may become more susceptible to

heatwaves. Importantly, drought impacts on the spatial pattern of susceptibility to extreme heat across a city may differ according to the spatial pattern of GV reduction. Our results suggest that the largest increases of LST with drought may occur in areas that are highly vegetated and normally relatively cool because these areas showed larger absolute reductions in GV cover. These areas, which experience relatively cooler climates under non-drought conditions, are less likely to have residential air conditioning, and may be less equipped to withstand extended hot conditions (Fraser *et al.*, 2017).

5. Conclusions

This study analyzed the impacts of the 2012–16 California drought on GV cover and the cooling effect of urban green space in urbanized Los Angeles County using multiple time series of satellite and airborne VSWIR and thermal imagery. Results indicate large, spatially variable changes in GV cover over the course of the drought concentrated particularly in inland areas. These coincided with elevated LST and decreased cooling from urban green space, with proportionally larger changes observed for grass- compared to tree-dominated green areas.

As cities grow and prepare for a more variable and warmer climate, many plan to expand urban green space and urban forests for heat mitigation as well as other ecosystem services such as carbon sequestration (Hutyra *et al.*, 2014) or stormwater runoff mitigation (Berland *et al.*, 2017). While our research focuses on the importance of urban green space for mitigating urban heat, it also seeks to caution that the ecosystem services provided by urban vegetation are not static and but rather are susceptible to climate change and climate extremes. Moreover, many tree species planted in cities may not be viable in a drier and

warmer climate (McPherson *et al.*, 2018). Our results suggest that there may be tradeoffs between urban heat mitigation programs and water conservation goals, particularly during drought. Thus, it is important to weigh the energy and water use goals of water conservation and lawn removal programs with potential urban climate impacts. For example, alternative water sources, such as recycled water and captured stormwater, can provide a pathway to satisfy both goals, particularly for large green spaces (Quesnel and Ajami, 2019). This is particularly important given climate projections, which indicate more frequent and more severe drought events in the region (Diffenbaugh *et al.*, 2015).

Acknowledgements

Thanks are due to D. L. Miller for discussions related to MESMA and to G. Hulley for discussions related to MODIS collection version. Partial funding for acquiring and processing the LAR-IAC data was provided by a NASA JPL Subcontract titled “Plant species mapping, water, and LMA using HyTES”.

Chapter 2: Diurnal sub-neighborhood variability in land surface temperature in Los Angeles using a multi-year time series of composited ECOSTRESS imagery

With Dar Roberts and Joseph McFadden

Abstract

The ECOsystem Spaceborne Thermal Radiometer Experiment on Space Station (ECOSTRESS) mission has a precessing orbital geometry that allows for frequent temporal sampling (every ~3 days) over the full diurnal cycle at a spatial resolution of 70 m. To date, no other orbital sensor combines full diurnal sampling with fine spatial resolution. Thus, ECOSTRESS is unique and highly desirable in study of urban climates, as patterns of temperature, humidity, and turbulence in urban areas are highly heterogeneous across both space and time. In this paper we used two years of ECOSTRESS imagery (initial n = 354 images, final n = 65 images after filtering and pre-processing) of urbanized Los Angeles County, USA from 2018-2020 to construct a composite a diurnal time series of urban land surface temperature (LST). We then used a high spatial resolution land cover classification (~0.2 m) and digital surface model (~0.8m) to investigate sub-pixel relationships between environmental drivers of spatiotemporal contrasts in temperature over the course of a full diurnal cycle. We found that two years of continuous ECOSTRESS thermal imagery was adequate to resolve urban LST at a diurnal time interval of approximately 2 hours with accurate representations of the timing of isothermal and heating/cooling periods and the timing minimum/maximum temperatures. We used the composited time series of LST to compute regressions between environmental drivers and LST over the study area and compared the relative strength of land cover, topographic, and morphological drivers over the course of a day. Results showed variability in the strength of different environmental drivers. For example, stronger reductions in LST were observed for sub-pixel Tree cover (max ΔLST = -8.3 °C px^{-1}) compared to Grass (max ΔLST = -6.0 °C px^{-1}). Contrasts were also observed in the timing of maximum effects from environmental drivers, with land cover drivers

showing peak effects from 12:00 to 14:00 PST and topographic/morphological drivers showing peak effects from 14:00 to 16:00 PST. The results in this study show promise for utility and accuracy of ECOSTRESS for resolving small spatiotemporal differences in LST in a highly heterogeneous urban environment. In addition, these results suggest that the current record of urban temperature from polar orbiting sensors underestimates the range of LSTs observed in urban areas by not sampling key points in the diurnal cycle.

1. Introduction

Land surface temperature (LST) is a key determinant of flows of energy, mass, and momentum at Earth's surface. In cities, LST is of particular importance as it is one of the most widely available climate measurements and it has strong links to urban energy and water use, human health and thermal comfort, and urban ecosystem function (Voogt and Oke, 2003). For example, remotely sensed LST data has been used to measure the surface urban heat island effect (Clinton and Gong, 2013; Bechtel *et al.,* 2019), the cooling effects of urban vegetation (Weng *et al.,* 2004; Wetherley *et al.*, 2018), and the biases and errors associated with remote measurement of LST over complex terrain (Roth *et al.*, 1989; Hu *et al.,* 2016). These data are particularly topical as problems associated with urban development and urban heat are projected to increase both with climate change and with the majority of global population growth concentrated in cities (United Nations, 2014; Broadbent *et al.*, 2020). For example, Hulley et al., (2020) and Zhao et al., (2018) show the potential for amplified urban heat islands with large-scale warming trends. Thus, there has been significant effort in recent years to use thermal imagery from satellite sensors to understand and attribute environmental drivers to spatiotemporal patterns of urban LST and surface urban heat islands.

Most studies of urban LST have relied on data from polar-orbiting satellite sensors such as the Moderate Resolution Imaging Spectroradiometer (MODIS), Advanced Very High Resolution Radiometer (AVHRR), Landsat Enhanced Thematic Mapper (ETM/ETM+), and Thermal InfraRed Sensor (TIRS) (Bechtel *et al.*, 2019). These sensors provide instantaneous "snapshot" measurements of LST over a wide range of spatial resolutions (60 m to 1 km), although, in the case of Landsat, are resampled to 30 m to match reflectance products.

However, due to their polar-orbiting geometry, they sample the surface at only one to two times of day (e.g., 10:30 and 22:30 local time for Landsat and MODIS Terra, 1:30 and 13:30 local time for MODIS Aqua) and do not provide information about the diurnal cycle of LST. Importantly, only one sensor (MODIS Aqua) measures LST during the hottest part of the day, which is most relevant to study of urban heat (Sobrino *et al.*, 2012). This significantly limits our understanding of urban LST at neighborhood and sub-neighborhood scales as data that cover the full diurnal cycle are limited to LSTs from geostationary satellites which are too coarse to resolve intra-urban contrasts in temperature.

In contrast to polar or geostationary orbiting satellites, the ECOsystem Spaceborne Thermal Radiometer Experiment on Space Station (ECOSTRESS) mission has a precessing orbit (Fisher *et al.*, 2020). This orbiting geometry allows for fine spatial resolution (70 m) and moderate temporal resolution (~3 days) and, most notably, allows for sampling of the full diurnal cycle using a single spaceborne sensor without gap filling or downscaling. A visual comparison of ECOSTRESS imagery to Landsat 7 ETM+, Landsat 8 TIRS, and MODIS Aqua thermal imagery is shown in Figure 1.

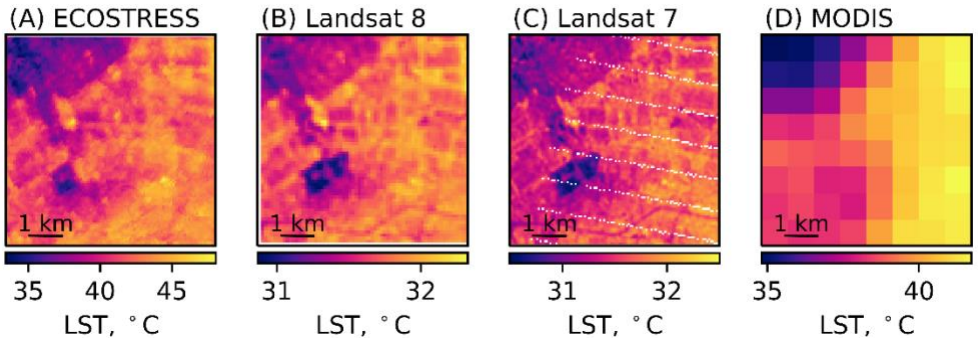

Figure 1: A visual comparison of (A) ECOSTRESS, (B) Landsat 7 and (C) 8, and (D) MODIS Aqua imagery for a 6 km by 6 km subset of the study area (see Figure 2 for location

within the study area). Images were acquired +/- 2 hour from noon PST during August and September of 2019.

In this paper, we explore the utility of the unique characteristics of the ECOSTRESS sensor by using two years of ECOSTRESS imagery to composite the first fully observational satellite-based estimation of the diurnal cycle of urban LST over a 2687 km^2 region of Los Angeles, California, USA. We used this composited time series with a high spatial resolution (~0.2 m) land cover classification and (~0.8 m) digital surface model to map the diurnal development of spatial contrasts in LST and to plot diurnal LST curves for common urban land cover types. We then quantified diurnal contrasts in relationships between land cover, topographic, and morphological drivers and LST.

2. Methods

2.1. Study Area

Our study area covers urbanized Los Angeles County, California, USA (Figure 2). Los Angeles County has a dry subtropical Mediterranean climate (Köppen class Csb in regions near the coast, Csa in inland regions), with a strong coastal gradient in precipitation and temperature and a documented urban heat island effect (Hulley et al., 2020). The study area was manually digitized using a basemap of composited National Agriculture Imagery Program (NAIP) aerial imagery from 2016 and the boundaries of Los Angeles County. We selected this region for three reasons: (1) Los Angeles includes a wide range of urban land cover/land use types and sociodemographic and economic profiles; (2) Los Angeles has a high proportion of clear-sky days, allowing for more frequent and more consistent sampling

throughout the year; (3) Los Angeles is ideal for compositing LST images from different dates as it has a relatively small annual range in temperature but strong spatial and diurnal contrasts in temperature at any given time owing to effects from proximity to coast and topography. This means that differences in LST are relatively small between images, but relatively large across space within images, which improves the effectiveness of compositing.

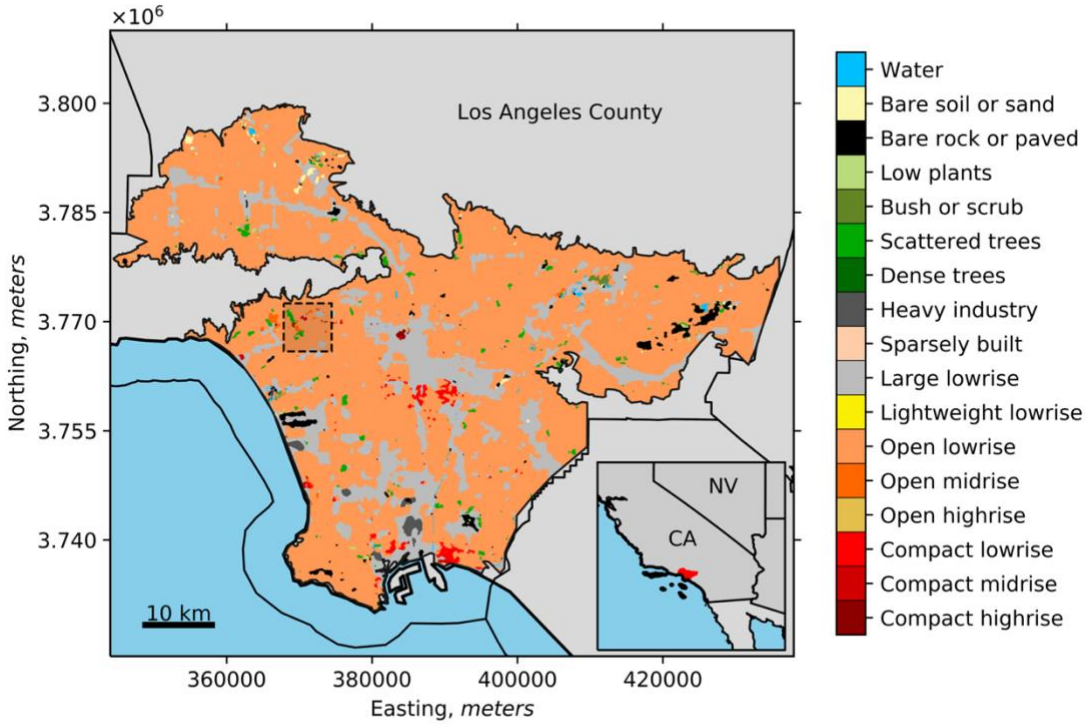

Figure 2: The urbanized Los Angeles County study area. Mapped reference classes are from Demuzere et al., (2020) which used Landsat 8 imagery to map Local Climate Zones (LCZ) – which delineate climatically distinct urban land cover/use types – for the continental United States. The extent of Figure 1 is outlined by the dashed line.

2.2. ECOSTRESS Imagery

ECOSTRESS is a thermal imager aboard the International Space Station (ISS) with five spectral bands covering 8.29 to 12.09 µm. Due to storage and bandwidth constraints, only the three bands centered at 8.78, 10.49, and 12.09 µm have been downlinked since May 15th, 2019 (Silvestri *et al.*, 2020). ECOSTRESS was launched in late-June 2018 and became operational in July of 2018. It has a native spatial resolution of 69 x 38 m at nadir, but its products are resampled to 70 x 70 m during processing. Level 2 LST and emissivity products are generated using temperature-emissivity separation (Gillespie *et al.*, 1998) with a radiometric precision and accuracy of 0.15 K and 0.5 K at 300 K respectively, and a band averaged Noise Equivalent Differential Temperature (NEDT) of ~0.1 K at 300 K (Hook et al., 2020; Hulley et al., 2019).

For our analyses, we acquired 354 images in total from July 2018 to August 2020. Images with <98% coverage of the study area were omitted from further analysis, leaving 148 images. After pre-processing, the remaining images were then clipped to the study area (Figure 2). After clipping, we gridded the imagery to a common 70 m pixel grid (UTM Zone 11N, WGS-84), then filtered for cloud cover and image artifacts. Because ECOSTRESS downlinks only thermal bands, its cloud mask relies solely on emissivity and temperature differences for determining cloud coverage and cloud shadow. In continental areas, this likely is a minor issue as cloud-to-ground temperature differences scale with cloud height. However, our coastal Los Angeles study area was frequently covered by low, thin clouds, and we found that the ECOSTRESS cloud mask underestimated coastal cloud cover, particularly morning fog and stratus clouds. To compensate for this, we manually filtered each image for cloud cover, omitting images having >5% cloud cover based on visual

assessment and an iterative LST thresholding approach. During this process we added additional flags for striping and georegistration artifacts, which were identified in approximately 15% of the images. Images with severe georegistration errors were omitted from the analysis. Images with significant striping were omitted from mapping results, but not from regression analyses. After all filtering steps, there were 65 complete, quality and cloud filtered images available for further analyses.

2.3. Ancillary data

We acquired a high spatial resolution land cover classification (~0.2 m) digital surface model (DSM, ~0.8 m) from the Los Angeles Region Imagery Acquisition Consortium (LARIAC, Los Angeles Region Imagery Acquisition Consortium, 2015). The land cover classification includes three vegetation classes (Tree, Grass (which includes short/small shrubs), and Tall Shrub) and three impervious classes (Building, Road/Rail, and Other Paved) as well as Soil, and Water classes. Both datasets were generated from tiled aerial orthophotography and LiDAR in 2014. The DSM was aggregated to 70 m to match ECOSTRESS taking mean and standard deviation of the height of all objects above the surface level (e.g., buildings, trees, etc.).

The land cover classification was used to derive sub-pixel fractional cover of each class. Sub-pixel fractional cover is highly desirable in this analysis for two reasons: (1) Urban cover is highly mixed at 70m (Wetherley *et al.*, 2017). This means that a simple majority resample likely represents a plurality, not a majority, as pixels are often covered by multiple classes in similar proportions (e.g., road, roof, and vegetation in low-rise residential areas). (2) Relationships between sub-pixel land cover fraction and urban LST can be

nonlinear (Wetherley *et al.*, 2018), particularly when pixels are mixed with two or more classes with diverging thermal properties. Thus, the underlying mixture of surfaces in a pixel can potentially be more important than the majority (or plurality) class. To derive fractional cover we overlaid the 70 m ECOSTRESS LST grid onto the land cover classification and calculated fractions of each cover class in each 70 m grid cell. We generated an Impervious fractional map by summing Building, Road/Rail, and Other Paved (which is largely parking lots), a Paved fractional map by summing the two paved classes, a Pervious fractional map by summing all pervious cover classes, and a Vegetation fractional map by summing Tree and Grass.

To quantify the effects of distance to coast, we computed distances to the nearest point on the coast to each cell in the 70 m ECOSTRESS grid using a coastline shapefile from the National Atlas of the United States representing the shoreline in 2014. To quantify the effects of topography, we used the 30 m National Elevation Dataset from the United States Geological Survey (USGS) resampled to the 70 m grid to generate the ground elevation maps. Maps of ancillary datasets are shown in Figure S1 of the supplemental materials.

2.4. Data analysis

For map visualization, we omitted 27 images with mean per-pixel view zenith angle > 15 degrees as off-nadir views tend to exacerbate minor georegistration errors and issues with image sharpness. The remaining 38 images were binned into eight 3-hour bins to visualize the spatiotemporal development of LST and into two 4-hour bins to represent day (11:00-15:00 PST) and night (2:00-6:00 PST) LSTs and to examine spatial patterns in the range of LST in urbanized Los Angeles County. We note that this approach is relatively conservative,

in non-urban applications and for regions with relatively homogenous land cover, these filters could likely be relaxed.

For analyses of LST in relation to environmental drivers, we used the full set of 65 images. To quantify diurnal and seasonal variability in cooling from urban vegetation cover, we binned the vegetation fractional map into 10% cover bins. We then calculated the difference between mean LST for >90% impervious pixels (representing nearly-pure impervious LST) and mean LST in each vegetation cover fraction bin. This was repeated for each image to plot the diurnal cycle of cooling from urban green cover for spring-summer and fall-winter seasons.

To quantify relationships between LST and distance to coast, topography, and land cover drivers we used two approaches: In the first approach, we binned the LST images into the same day/night bins as the map-based analysis and computed a per-pixel day/night range of LST. We then plotted distance to coast, height above ground level, and green cover fraction against the diurnal range of LST to visualize the shape of the relationship between microclimatic drivers of LST and the range of LST. In the second approach, we quantified the strength and direction of relationships between LST and micro-climatic drivers over the course of a diurnal cycle by binning LST images into 2-hour bins and computed linear regressions between LST and each driving variable extracting slope and Pearson's R.

To develop a generalizable time course of urban LST for the range of common urban land cover types, we binned the composited time series of images into 2-hour bins and calculated mean and standard deviation for nearly pure pixels (>90% cover) of each land cover class. We also computed change in LST between time bins to compare heating and cooling rates for each land cover class over the course of a day.

2.5. Corroboration using concurrent MODIS LST Imagery

As this dataset is unique in its diurnal coverage and spatial resolution, it is difficult to directly validate. Ground based thermal measurements have been used to radiometrically calibrate the ECOSTRESS thermal sensor and LST retrieval (Hook *et al.*, 2020), but are less useful for validating spatial patterns and relationships between LST and surface structure and land cover drivers. Direct comparison against other satellite thermal sensors is similarly difficult, as it is exceedingly unlikely for an ECOSTRESS image to co-occur with imagery from a comparable satellite sensor. Thus, instead of validating using a comparison of concurrent images, we compare composited ECOSTRESS LSTs to composited MODIS LST images from concurrent time periods (i.e., taken at a similar time of day and similar day of year).

To corroborate the ECOSTRESS composited time series, we downloaded MODIS Aqua/Terra LST images (MOD11A1-006 and MYD11A1-006) for July 2018 to August 2020 and clipped them to the study area. These images represented four times of day including 1:30, 10:30, 13:30, and 22:30 PST. We then bilinearly resampled the ECOSTRESS images to match the MODIS 1 km grid. To match time of day and time of year, we filtered the ECOSTRESS images based on time of acquisition to only include images within 1.5 hours of the MODIS overpass times and binned them to match the Aqua day/night and Terra day/night acquisitions. Next, for each MODIS overpass bin, we used the ECOSTRESS date of acquisition to filter the MODIS time series to only include images within 3 days of an ECOSTRESS overpass. After binning and filtering, we calculated a per-pixel mean ECOSTRESS and MODIS LSTs for each time of day bin. To assess error and correlation, we

calculated slope, intercept, root mean square error (RMSE), and coefficient of determination (R^2) between the four pairs of composited datasets.

3. Results

3.1. Annual and diurnal timing of the ECOSTRESS catalogue for the Los Angeles, CA, USA region

Figure 3 shows the annual and diurnal timing of each complete image (i.e. >98% coverage) that entered the second level of filtering. It is important to note that ECOSTRESS is operated as a pseudo-sampler, with target regions and time periods. Thus, unlike MODIS or Landsat, images are not necessarily equally distributed through space and time. We found that images collected over the study period were biased towards the summer and fall seasons, and images were more likely to have been acquired during the nighttime and late evening hours than in the morning hours. In addition, due to cloud cover, images were less likely to pass the cloud filtering procedure during the winter and spring months.

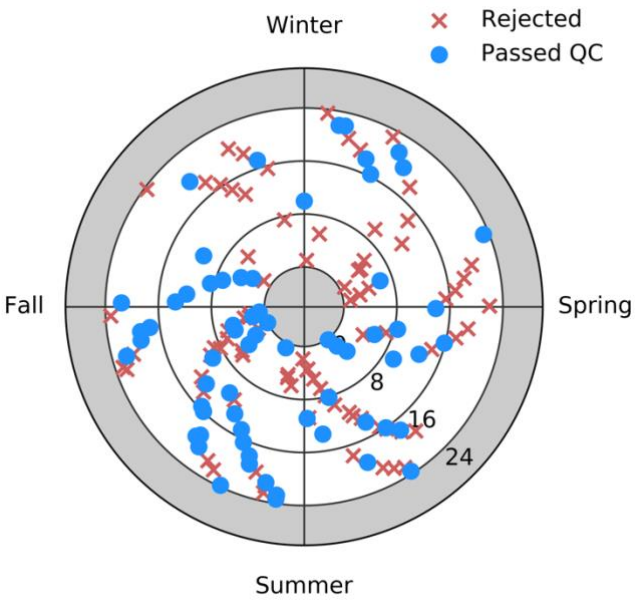

Figure 3: Diurnal and seasonal coverage of the time series of ECOSTRESS imagery in the second level (cloud and artifact) of quality control filtering. The inner axis represents hour of day in Pacific Standard Time (PST).

3.2. Spatial patterns of diurnal LST development

Figure 4 shows binned LST measurements over a full diurnal cycle. In Figure 5 we show the mean per-pixel diurnal range of LST (ΔLSTd) calculated from the difference in mean LST from 11:00 to 15:00 PST (n = 5 images) and mean LST from 2:00 to 6:00 PST (n = 6 images). The composited time series of LST showed strong thermal contrasts across the study area based on surface composition, distance to coast, and street-grid orientation. Highways and dense road grids (particularly those that line up with the image grid) were visible as cool spots during the day and hotspots during the night (ΔLSTd = ~23–30 °C). Highly impervious areas showed high LST during the day and low LST at night, resulting in a large diurnal range in LST (ΔLSTd = ~30-35 °C). This is particularly apparent as distance

to coast increases. A daytime cool island and nighttime heat island was observed for the downtown core of Los Angeles (indicated by the region of Compact Highrise land cover near the center of the study area).

Coastal regions were the coolest part of the city during both day and night. This resulted in ΔLSTd <20 ℃ for areas near the coast. Areas with surface water had a particularly distinctive pattern, with high LST at night and low LST during the day and a ΔLSTd similar to coastal regions. A small proximity effect was observed for inland lakes, with smaller ranges in LST observed around the perimeter of lakes. Covered reservoirs (which are common in the study area) had high LST during the day from strong heating of the low-albedo covering materials and anomalously high LST at night as water below transferred heat to the covering material. Large areas of green space had relatively low LST during both the day and night (ΔLSTd = ~18-23 ℃). This effect was stronger for irrigated parks and golf courses compared to unmaintained or senesced vegetation.

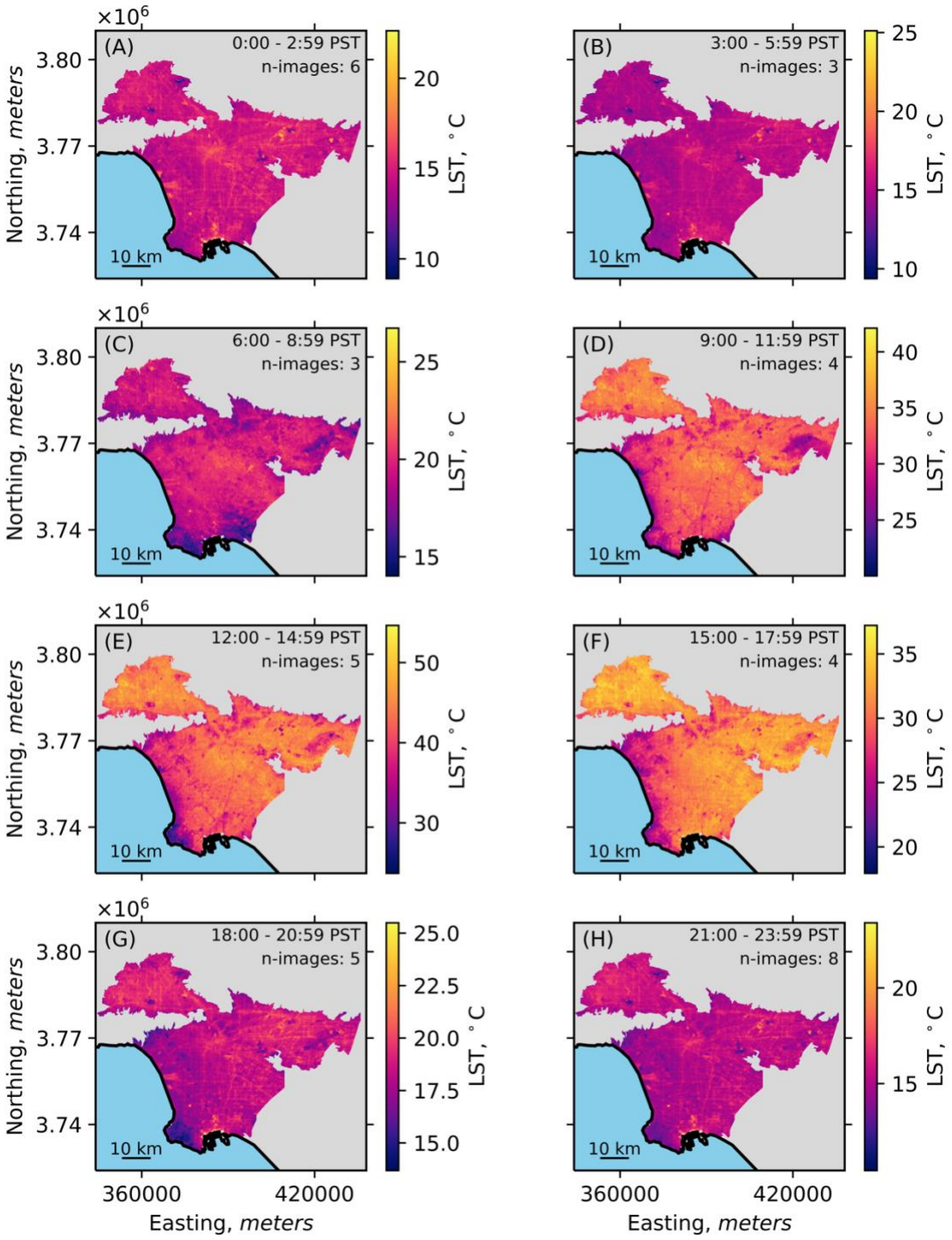

Figure 4: Mapping the diurnal pattern of urban LST for the study area for 3-hour bins. Color bars for each binned image show the range between the 5th and 95th percentile. Each image

has a unique colorbar to visualize spatial differences in each binned image, which are not visible when using a shared colorbar.

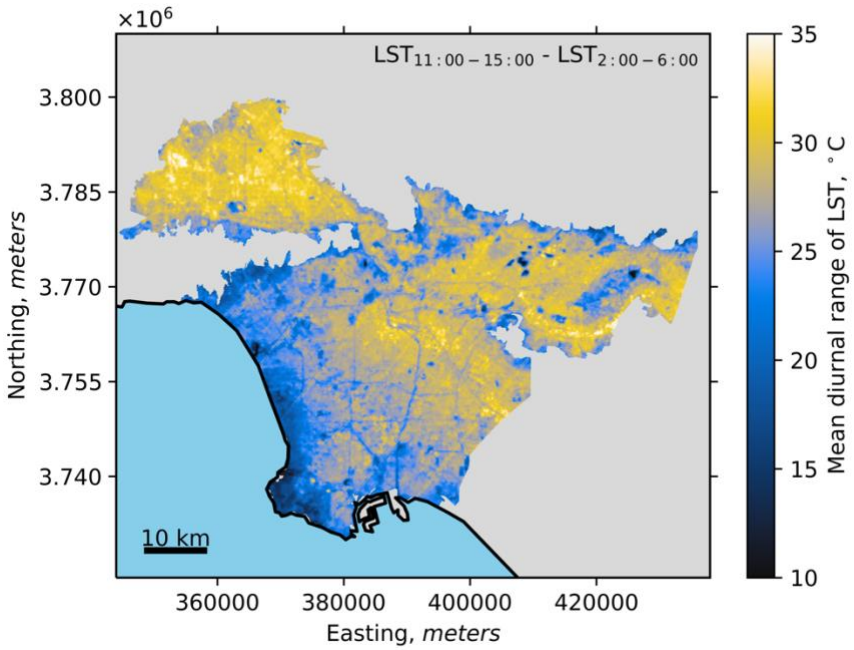

Figure 5: The diurnal range of LST (ΔLSTd) over the study area calculated from the difference in mean LST from 11:00-15:00 PST (n = 5 images) and mean LST from 2:00-6:00 PST (n = 6 images). Composited images include samples from all seasons.

To investigate relative LSTs of different classes, we filtered the 2hr binned images for nearly pure pixels of each land cover class (>90% cover) and calculated mean LST for each class and each binned time step. The diurnal course of LST for each class as well as heating/cooling rates (as dLST/dt in °C hr^{-1}) are shown in Figure 6. The number of discrete observations in each diurnal bin ranged from 4 to 9 images, with generally lower frequency sampling in the morning hours due to frequent fog and stratus clouds in the summer months. The time bin covering 6:00 to 8:00 represented an outlier with only two cloud-free samples,

one in the winter and another in early-Fall. In addition, we used the same day and night bins as in Figure 5 (Day = 11:00 to 15:00 PST, Night = 2:00 to 6:00 PST) to visualize distributions of LST for >90% pure pixels of each class in Figure 7.

As expected, maximum LST was observed near solar noon (between 12:00 and 14:00) and minimum LST was observed just before sunrise (between 6:00 and 8:00). The timing of maximum LST was slightly earlier for pervious materials compared to impervious, with dLST/dt > 0 ℃ hr^{-1} through 12:00 PST for impervious materials. The shapes of morning heating rates and afternoon/evening cooling rates were dissimilar, with stronger dLST/dt observed in the morning (maximum dLST/dt = 6.9 ℃ hr^{-1} for Impervious, dLST/dt = 4.9 ℃ hr^{-1} for Water at 8:00 PST) compared to a longer and more shallow cooling curve observed after solar noon for all materials (dLST/dt = -6.1 ℃ hr^{-1} for Impervious, dLST/dt = -4.5 ℃ hr^{-1} for Water at 16:00 PST). At night, dLST/dt converged for all classes and was less consistent between time intervals but appeared slightly negative trending towards 0 ℃ hr^{-1}.

Daytime LST had a much larger range than observations at night, owing to synoptic and seasonal contrasts which more strongly affect variability in daytime temperatures. Among pervious materials, Tree was coolest (mean LST = 35.4 ℃) compared to 38.9 ℃ and 40.4 ℃ for Grass and Soil. Among impervious surfaces, the Building class was warmest (mean = 43.5 ℃) followed by Other Paved (41.2 ℃) and Road/Rail (40.8 ℃). LST at night showed a much smaller range for all classes. The largest ranges in nighttime LST were observed for Grass, Water, and Other Paved. Water was the warmest class (mean LST = 16.9 ℃), again owing to a relatively high thermal mass, but also had an anomalously high range of LST compared to its spatial coverage. This was likely due to differences in thermal mass with water depth. Road/Rail was the warmest non-water class at night (14.8 ℃) compared to

means of 13.9 ℃ and 14.7 ℃ for Building and Other Paved impervious classes. For pervious classes, nighttime temperatures were slightly cooler than impervious, with means of 12.2 ℃, 12.9 ℃, and 13.6 ℃ for Tree, Grass, and Soil respectively.

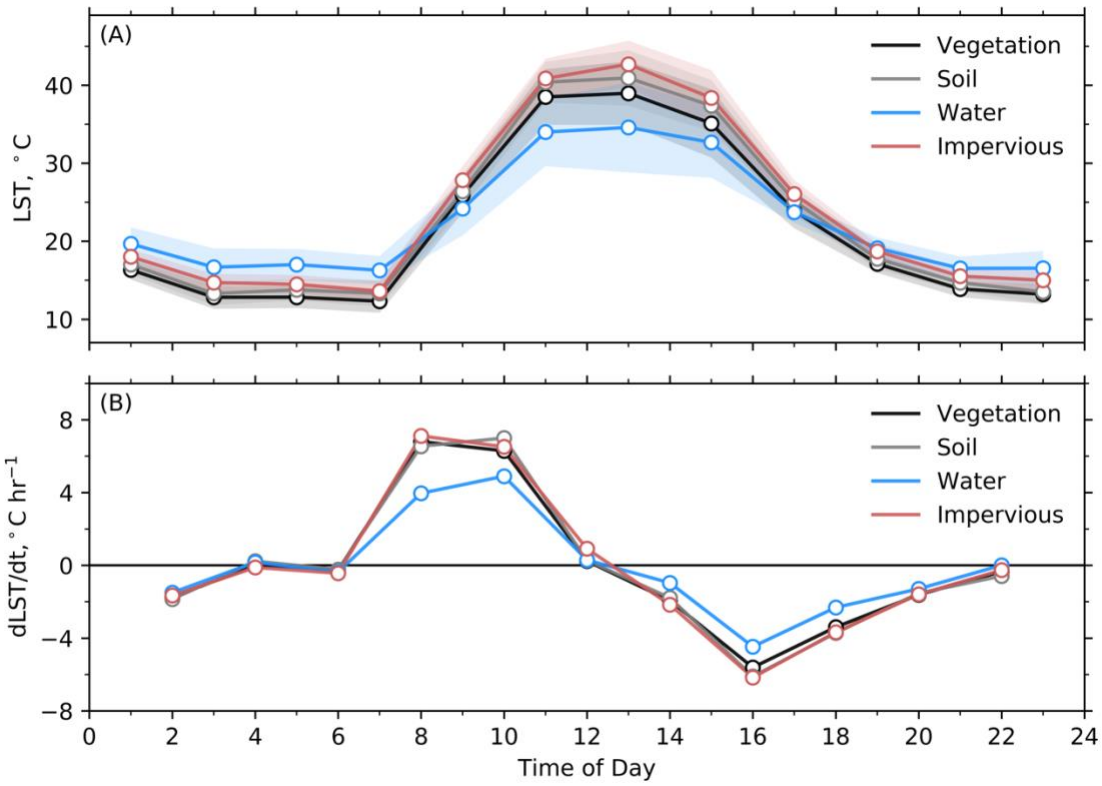

Figure 6: (A) Mean LSTs for nearly-pure (>90% cover) aggregated land cover classes calculated from binned LST images (2 hour bins). (B) Heating and cooling rates (dLST/dt, ℃ hr^{-1}) calculated between time bins as the difference in LST between bins divided by dt = 2.

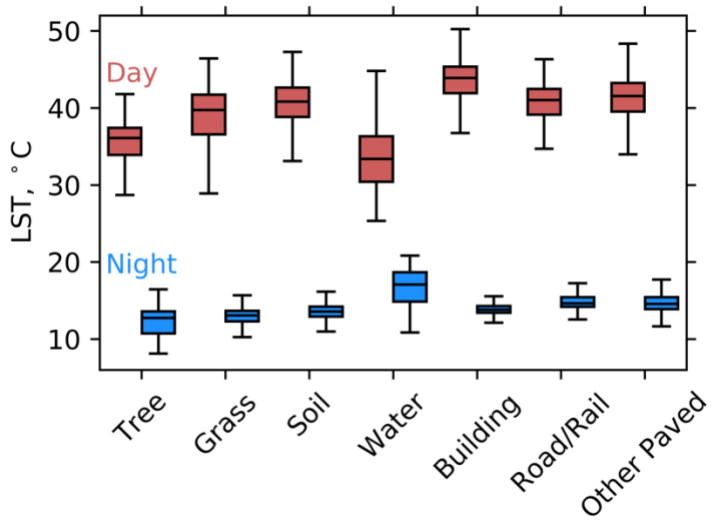

Figure 7: Distributions of LST by class for day (11:00 to 15:00 PST) and night (2:00 to 6:00 PST) for >90% pure pixels. Boxes indicate 25%, 50%, and 75% quartiles. Whiskers indicate 1.5 times the interquartile range.

3.3. Environmental drivers of LST

Relationships between ΔLSTd and distance to coast, elevation, height above ground of buildings and trees, and percent green cover are shown in Figure 8. ΔLSTd increased with distance to coast increased. We also observed that proximity to coast only moderated LST within ~20 km of the coast, with little to no change in LST observed at distances >20 km. In addition, the ΔLSTd also decreased with increasing green cover fraction, Vegetation cover provided stronger cooling in inland regions compared to coastal areas, as cooling scaled with increasing LST, both within and among images. The magnitude of LST modifications from distance to coast and green cover were approximately similar (mean ΔLSTd = 5.5 °C over 0 km to 20 km and 4.9 °C for 0% to 100% green cover differences respectively). Height above ground and elevation had non-significant negative relationships with ΔLSTd.

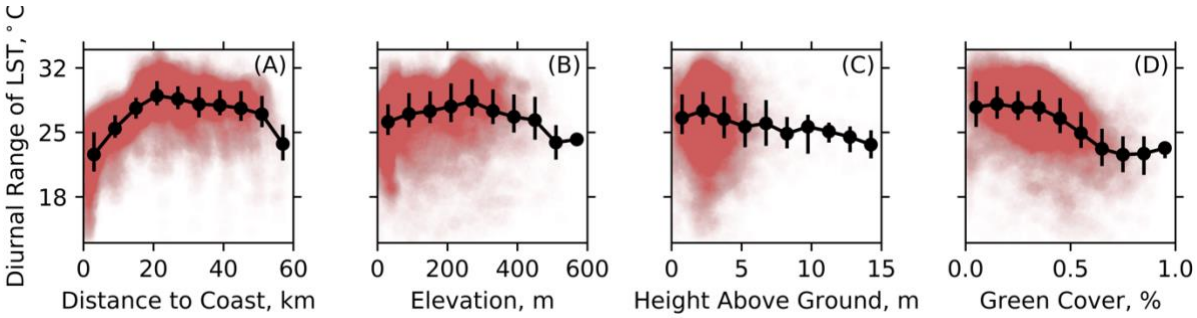

Figure 8: Per-pixel relationships between the ΔLSTd (using the same bins shown in Figure 5) and environmental drivers. Dots and error bars are calculated over 10% bins of the range of each independent variable. Error bars show the 25th and 75th percentile of LST for each bin.

Figure 9 shows the diurnal course of the difference in mean temperature between nearly pure (>90%) impervious pixels and pixels from a gradient of vegetation cover fraction (10% bins from 0% cover to 90% cover). During the day, the strength of cooling from urban vegetation cover (ΔLSTveg) was most variable for pixels with vegetation cover between 30% and 70%. In contrast, increasing vegetation cover at low (<30%) and high (>70%) vegetation fractions had a relatively weak effect on LST,

Tracking how cooling from urban vegetation changes through a diurnal cycle reveals that ΔLSTveg increased starting from sunrise to a maximum just after solar noon (~13:00 PST) in both spring-summer and fall-winter. Peak cooling was stronger in spring-summer (ΔLSTveg = 7.2 ℃) compared to fall-winter (ΔLSTveg = 3.9 ℃). We found mean ΔLSTveg for a given image was positively correlated with mean LST ($r = 0.94$, $p < 0.01$, $n = 65$), with stronger cooling observed on warmer days. In spring-summer, ΔLSTveg persisted for a longer period than fall-winter, with strong cooling (ΔLSTveg = ~4K) observed through the

late-afternoon. In both seasons, ΔLSTveg was near 0 just before sunrise indicating a period of relatively equal LST for vegetation and impervious cover.

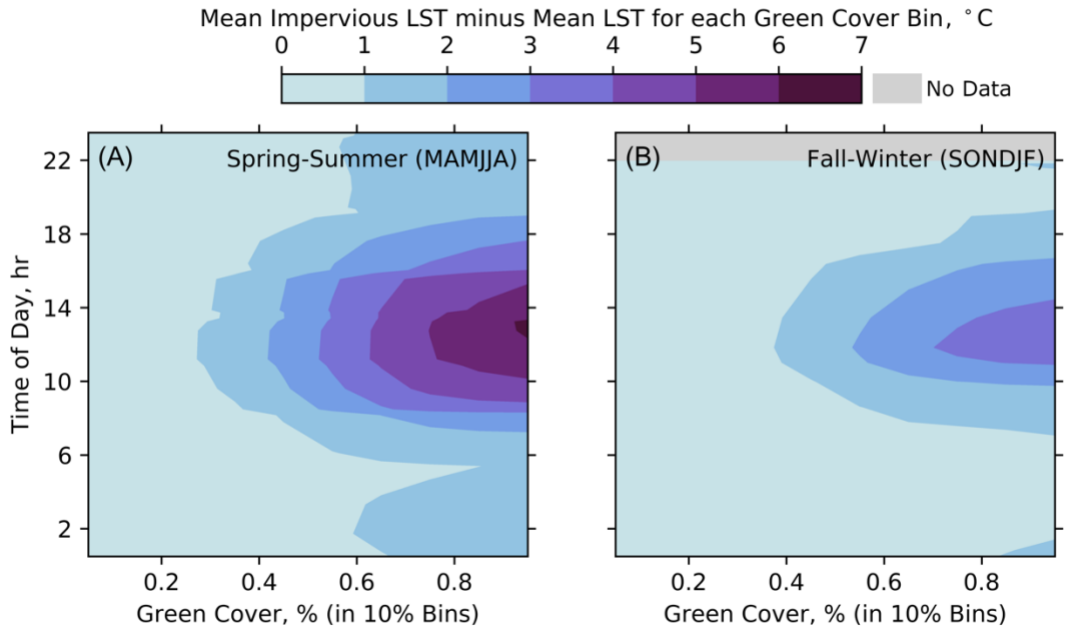

Figure 9: The diurnal evolution of the cooling effect of urban green cover. For each image, we binned the data into 10% green cover bins covering a range of vegetation cover fractions from 0% to 90% cover. The mean LST for each green cover bin was then subtracted from the mean LST of all >90% impervious covered pixels. The data were plotted separately for the spring-summer and fall-winter seasons. Data were smoothed using a gaussian filter with sigma = 1.

Figures 10 and 11 show slope and Pearson's R from linear regressions between subpixel fractional cover of land cover classes and topographic environmental drivers and LST over the course of a diurnal cycle. Slopes are expressed as the average change in LST per unit change in the independent variable. Increasing impervious cover was correlated with

warmer LST throughout the day, with a maximum ΔLST of 6.1 ℃ px^{-1}, r = 0.52 from 12:00 to 14:00 PST. Of impervious subclasses, Other Paved had the strongest daytime maximum ΔLST (5.0 ℃ px^{-1}, r = 0.30) followed by Building (ΔLST = 4.1 ℃ px^{-1}, r = 0.19), and Road/Rail (ΔLST = 2.18 ℃ px^{-1}, r = 0.11). This likely owes to the fact that the Other Paved class was dominated by expansive areas of asphalt cover such as airport tarmac and parking lots, which were not shaded during the day and often had very little vegetation cover. In contrast, buildings and road/rail were more strongly affected shading and radiation trapping by building geometry, and thus more heterogeneity of pixel-to-pixel LST, which resulted in weaker positive correlations and lower slopes between increased building and road cover and LST. Throughout the night, ΔLST was low for all impervious materials with weak correlation, reaching a minimum just before sunrise (4:00 to 6:00 PST).

Increasing fractional cover of water bodies such as lakes and reservoirs was negatively correlated with daytime LST (max ΔLST = -6.0 ℃ px^{-1}, r = -0.44) and positively correlated with nighttime LST (max ΔLST = 2.9 ℃ px^{-1}, r = 0.53) owing primarily to the very high specific heat of water, which suppressed heating and cooling rates, and daytime heat mitigation from latent heat exchange. Increasing pervious cover was negatively correlated with LST throughout the day, particularly during the midday hours from 10:00 to 14:00 PST (max ΔLST = -6.0 ℃ px^{-1}, r = -0.53). We observed negative ΔLST and strong negative correlations for Tree (max ΔLST = -8.3 ℃ px^{-1}, r = -0.37) , which were higher than those observed for Grass cover (max ΔLST = -6.0 ℃ px^{-1}, r = -0.28), likely because of the wide range of grass conditions found in the study area. Turf grass is more susceptible to seasonal variability in precipitation but is also frequently irrigated (e.g. in golf courses). Thus, grass has a wide range of thermal mass that is low when grass is senesced and high

when grass is irrigated, resulting in strong spatial contrasts in heating/cooling rates for grass areas and lower correlation between grass cover and LST. As with impervious cover, weaker correlations and slopes near $\Delta LST = 0$ °C px^{-1} were observed for pervious materials, with minimums observed just before sunrise.

Increasing distance to coast had a strong positive correlation with daytime LST (max $\Delta LST = 0.13$ °C km^{-1}, $r = 0.50$) with maximum slope/correlation observed two hours later than maximum slope/correlation for land cover classes (between 14:00 and 16:00). At night, correlations between LST and distance to coast were less consistent owing partially to cloud cover prior to the image acquisition, which can reduce cooling/heating rates depending on cloud timing. Increasing surface height above ground had a weak negative ΔLST and correlation in the afternoon hours (max $\Delta LST = -0.16$ °C m^{-1}, $r = -0.10$) and ΔLST near zero with little to no correlation at night. Elevation had negative ΔLST and correlation at night (max $\Delta LST = -0.04$ °C dam^{-1}, $r = -0.46$) and positive ΔLST and correlation observed during the day (max $\Delta LST = 0.07$ °C m^{-1}, $r = 0.23$). However, this relationship is influenced by the fact that higher elevations are generally observed in inland areas, which have strong diurnal contrasts in LST.

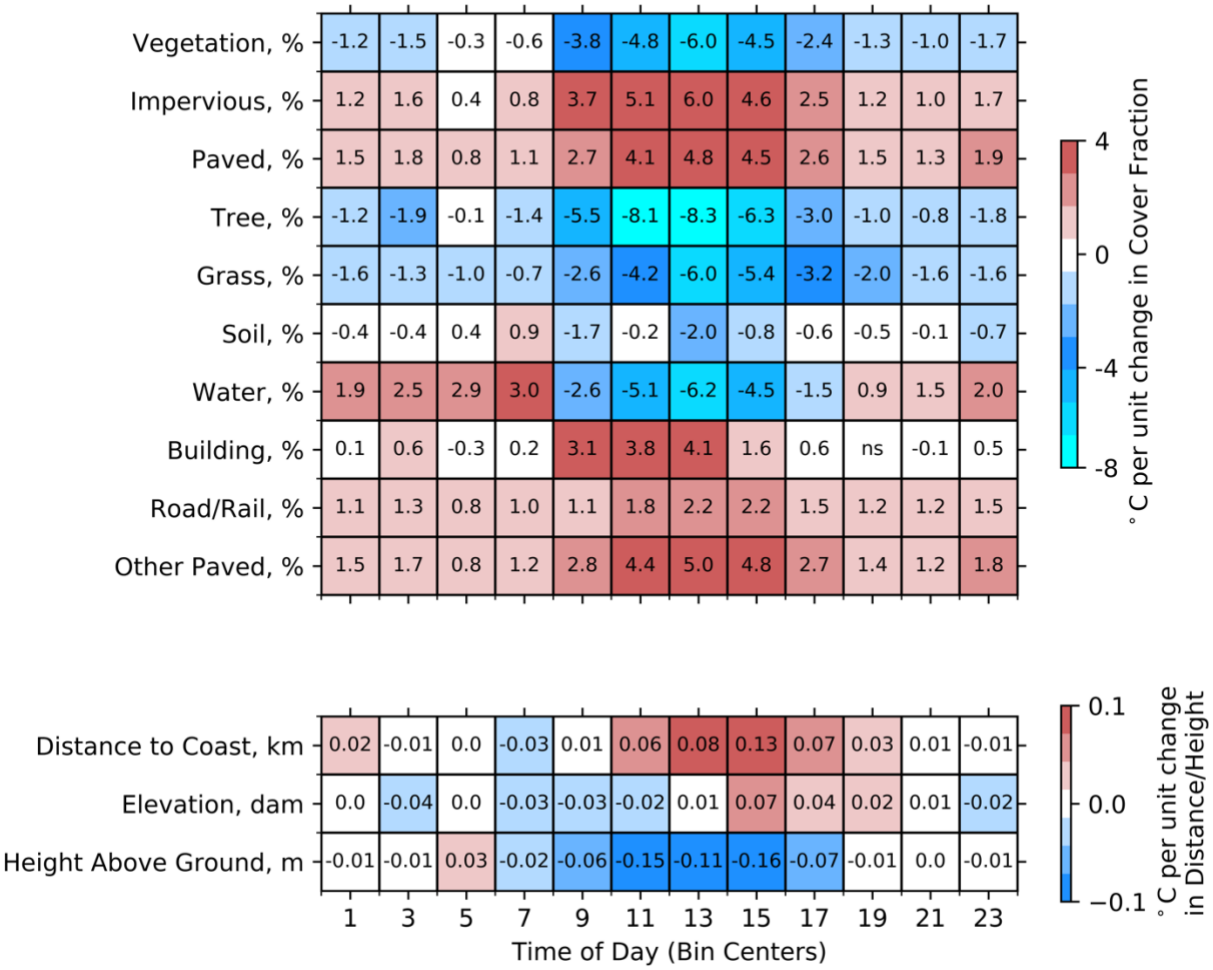

Figure 10: The diurnal evolution of slopes of a linear regression between each independent variable and binned mean per-pixel LST. Slopes are reported with units of in per unit change in the independent variable (e.g., per 0% to 100% change in cover, or per 1 km change in distance to coast). X-axis tick labels indicate time bin centers. “ns” denotes not significant based on a threshold of $p < 0.01$.

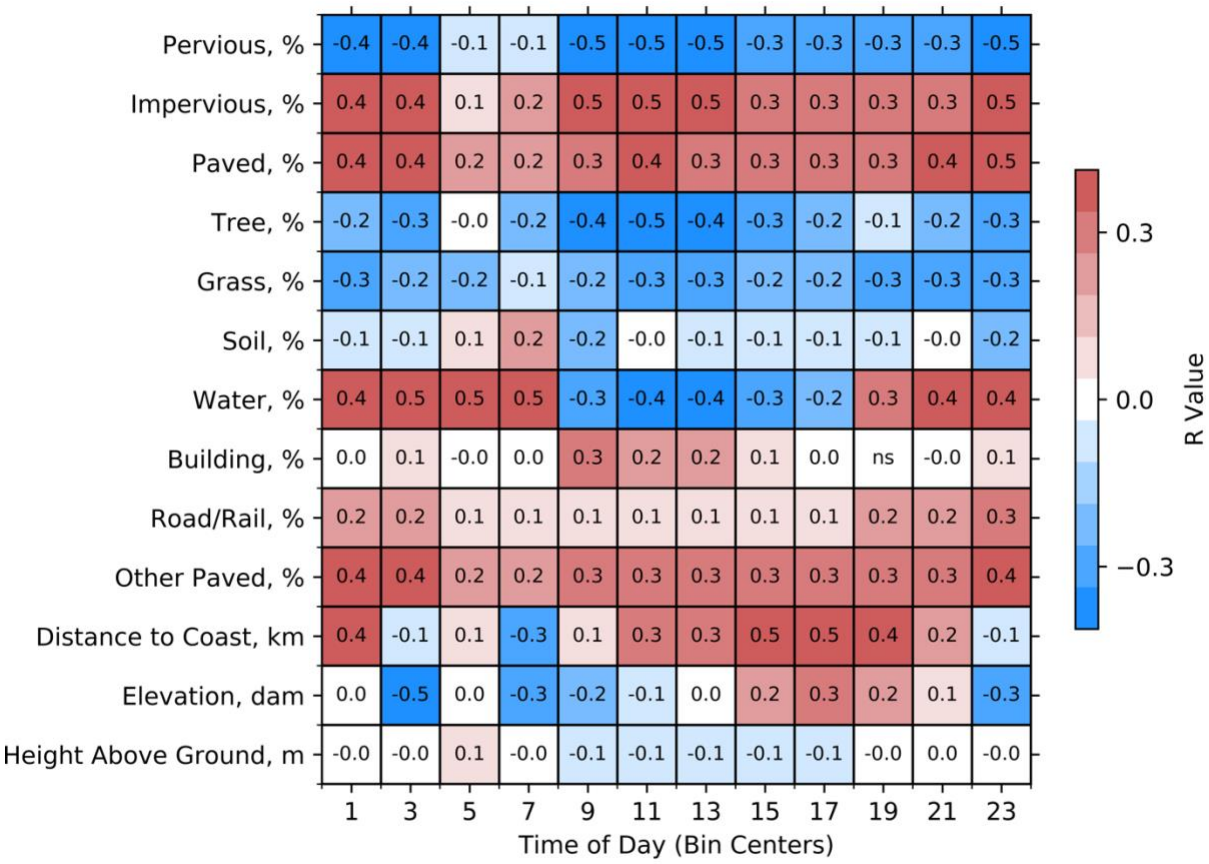

Figure 11: As in Figure 8, but with correlation coefficients (Pearson's R) of the same linear regression. "ns" denotes not significant based on a threshold of $p < 0.01$.

To examine differences in diurnal patterns of LST for different building heights, we segmented the building class based on mean height above ground using the DSM and took the difference between Building LST and Paved LST at each time step (ΔLSTbp, Figure 12). Buildings were warmer than paved surfaces during the day, with maximum ΔLSTbp > 2.3 ℃ near solar noon (10:00 to 14:00 PST) and cooler during the night, with ΔLSTbp < -1.1 ℃ near sunrise (6:00 to 8:00 PST). During the day, increasing building height decreased

ΔLSTbp indicating that pixels with taller buildings were relatively cool for most of the day. This was particularly apparent for mean building heights > 16m, which showed relatively weak late-morning (10:00 to 12:00 PST) heating rates. The relationship between building height and LST is less clear in the evening and night, with the tallest class of buildings showing persistent heating through the early afternoon (12:00 to 16:00 PST) and warmer LST in the evening hours (16:00 to 22:00 PST). At night, mean above ground height had little effect on LST.

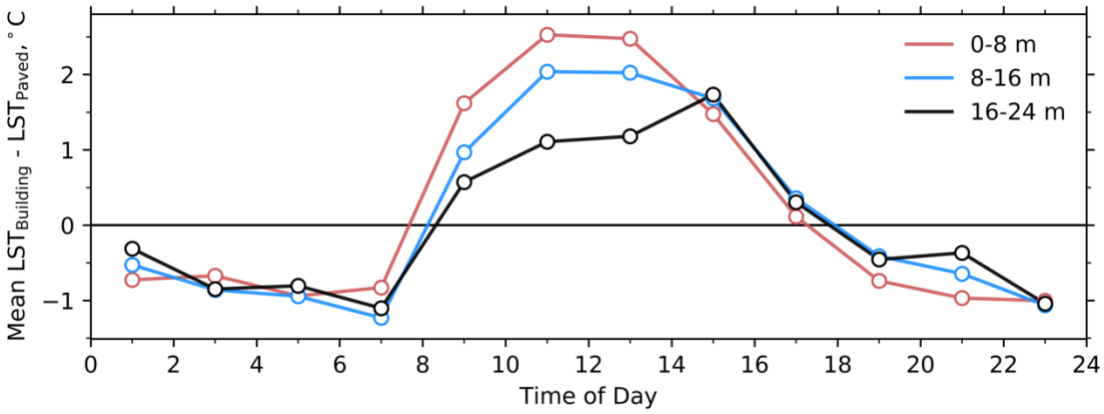

Figure 12: A comparison of the mean difference in LST between >90% pure Building and Paved pixels segmented based on mean building height.

3.4. Comparison to MODIS Aqua/Terra Climatology

Figure 13 shows the results of the comparison between diurnally and annually coincident MODIS and ECOSTRESS images. For both daytime sampling periods we observed relatively high correlation between the MODIS and ECOSTRESS composites, with slopes near 1 and $r^2 > 0.75$ ($p < 0.01$), with consistent residuals over the range of observed LSTs. A slight warm bias in the ECOSTRESS dataset was observed for relatively cool pixels in the Terra daytime comparison (10:30 PST). Daytime RMSEs were on the order of or less

than potential uncertainties from emissivity correction, anisotropy, and atmospheric correction over similar daytime periods (Hulley et al., 2012; Voogt & Oke, 1998). A smaller range of LST and weaker correlations were observed at night over a smaller range of temperatures ($r^2 < 0.5$, $p < 0.01$). A slight cool bias is observed in the Terra nighttime comparison (22:30 PST), particularly for relatively cooler pixels. ECOSTRESS sampling near 1:30 PST preferentially occurred during the warmer summer and fall months with no winter sampling, resulting in higher composited LSTs at 1:30 PST compared to 22:30 PST. Residuals in both nighttime cases were non-uniform across the range of LST, however, because of the small range in observed LST, RMSE was lower at night.

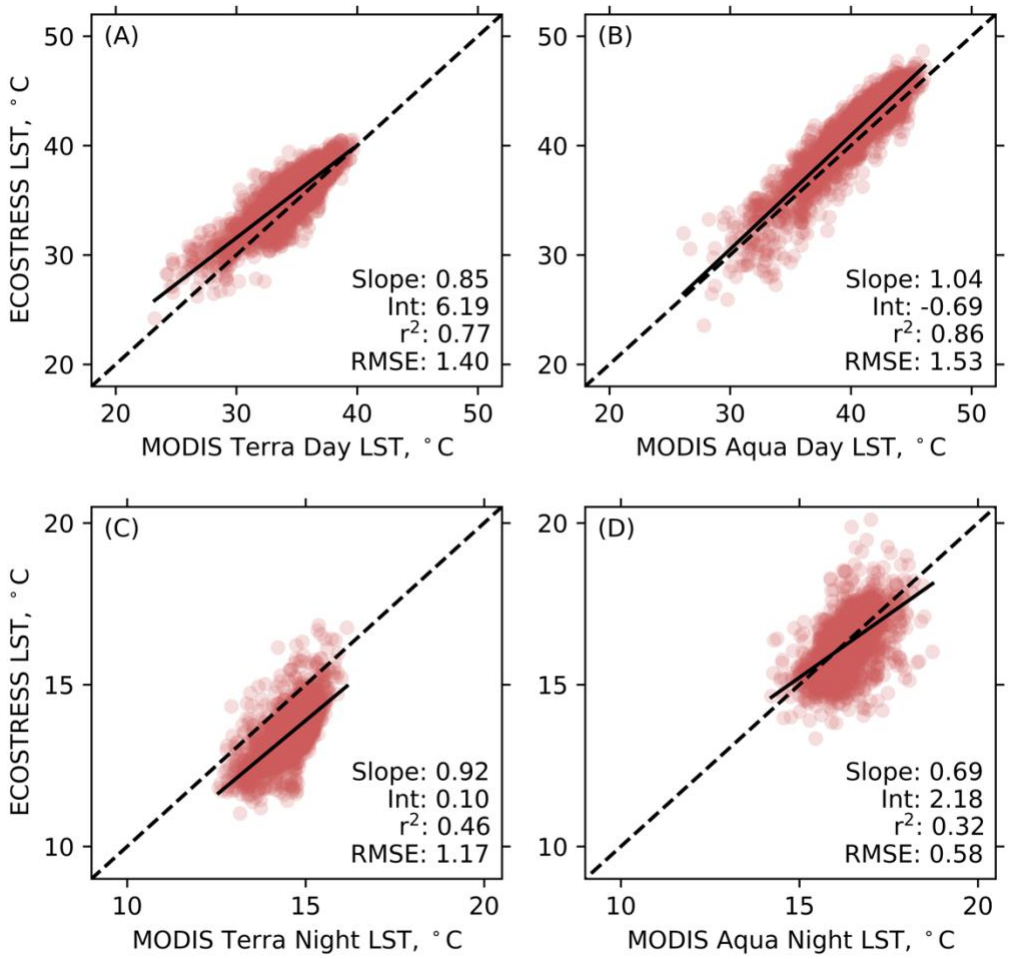

Figure 13: Comparisons of per-pixel composited mean LST from concurrent (within 3 days and within 1.5 hours) ECOSTRESS and MODIS Terra/Aqua LST images.

4. Discussion

In this paper, we used a multi-year time series of filtered ECOSTRESS LST images to composite and map a full diurnal cycle of LST in the urbanized Los Angeles, CA, USA region. This work presents the first fully observational satellite-based time series of diurnal urban LST at fine spatial resolution. First, we used this time series to develop and map a generalizable diurnal cycle of LST for common urban land cover types. We found that

composited ECOSTRESS images can accurately represent an annually averaged full diurnal cycle of LST and can be used to quantify how relationships between LST and environmental drivers change over an averaged diurnal cycle. As expected, we found strong and variable relationships between LST and proximity to coast, surface thermal and radiative properties (which are governed broadly by land cover class), and surface geometry. The relative importance of these drivers varied through the course of the day.

4.1. The utility and validity of a composited diurnal cycle of urban LST

Temporally continuous, fine resolution, spatially extensive measurements of LST have long been a goal in urban remote sensing (Voogt & Oke, 2003; Zhou et al., 2013). However, because of the tradeoff between spatial coverage, spatial scale, and temporal scale, it is difficult, if not impossible, to achieve all of these characteristics with a single sensor. Fine-scale thermal remote sensors (e.g. airborne and ground-based thermography) are generally accompanied by domain and time restrictions. On the other hand, while coarse-scale sensors (e.g. MODIS) generally have and more frequent overpass times and wider spatial coverage, they cannot represent complex and heterogeneous urban forms well (e.g. non orthogonal street grids and highly mixed terrain). These are significant challenges for the utility of remotely sensed urban LST, as much of the remotely sensed record of urban LSTs is either relatively anecdotal (in space or time) or lacks fine scale representivity (Zhou et al., 2019). This, we posit, has slowed progress in integrating satellite-based remotely sensed LST into urban climate models and into a process-based understanding of urban climate phenomena and processes. Thus, we consider the unique properties of ECOSTRSS to be a particularly useful source of information to close the gaps in diurnal coverage left by polar

orbiting remote sensors and as a tool for forcing and validating downscaling of geostationary imagery and Diurnal Temperature Cycle (DTC) models.

Composited diurnal curves from ECOSTRESS are consistent with curves from thermal imagers in Adderley et al., (2015) and Meier et al., (2011), with annual time series fixed radiometry in Allen, (2017), and with diurnal curves from DTC models in Sismanidis et al., (2016) and Weng & Fu, (2014). ECOSTRESS imagery was able to capture diurnal features such as the period of isothermality before sunrise, differences in intensity between morning heating rates and afternoon cooling rates, and the development of thermal contrasts between different land cover types (e.g. impervious versus vegetation cover) and surface morphologies (e.g. shading from building geometry). The composites were also able to accurately depict the timing of annually averaged diurnal minimum and maximum LST, with minimum LST observed just before sunrise (between 6:00 and 8:00 PST) and maximum LST just after solar noon (between 12:00 and 14:00 PST). Our results also support the notion that the timing of overpass cycles for Landsat and MODIS Terra, which are commonly used for urban thermal remote sensing do not coincide with diurnal extremes of LST (Sobrino *et al.*, 2012). Indeed, no polar orbiting thermal sensor is able to capture the coolest part of the day just before sunrise, which is highly useful for constraining models. Thus, the satellite record of urban temperatures likely underestimates the full range of urban LST.

4.2. Limitations

This analysis has multiple limitations, some shared between all thermal remote sensors, and some unique to ECOSTRESS and to the compositing method. All satellite remote sensors undersample urban surface geometry, as narrow field-of-view sensors only

view a fraction of the urban surface (Voogt and Oke, 2003). This results in a bias towards horizontal facets (e.g. roofs and roads) and an effective anisotropy of urban LST, with a general overestimation of daytime LST and an underestimation of nighttime LST for nadir and near-nadir remote sensors (Voogt and Oke, 1998a). The magnitude of effective anisotropy varies with surface morphology and time of day, but is generally largest for neighborhoods with height to width ratio between 1.5 and 3 (Krayenhoff and Voogt, 2016) – which is common throughout our study area. While ECOSTRESS samples from a wider range of sensor zenith/azimuth angles than other fine spatial resolution thermal sensors (e.g., Landsat), it does not sample representative proportions of horizontal, vertical, and sloped facets, particularly in densely built areas.

Another prominent limitation results from incomplete diurnal and seasonal sampling. While ECOSTRESS samples the surface at a much wider range of times of day compared to polar-orbiting satellites, its overpass cycles are not randomly distributed across seasons and times of day and are still subject to influence from synoptic conditions. In addition, cloud cover was spatially variable and more likely in the coastal regions during May/June and over the study area during the winter months. This added additional noise to early morning composites as cloud cover is often difficult to detect during isothermal periods of the day and because coastal cloud often dissipates just after sunrise, resulting in lower LST for previously shaded areas. We anticipate similar impacts from partially cloudy days which would likely result in reduced overall LST and reduced spatial contrasts in LSTs across our environmental variables. A more robust cloud filtering regime incorporating cloud climatologies from ground station data or reanalysis data may provide more explicit cloud impact assessment.

However, as LST data scarcity was the main limitation in this study, we chose to filter only for cloud intrusion detected in the LST imagery.

We encountered an additional limitation relating to image quality which varied significantly between acquisitions. As is common with other wide-FOV thermal images (e.g. MODIS), image sharpness degrades with increasing off nadir view angle as instantaneous field of view increased and georegistration error increased. These errors were visible in our ECOSTRESS time series as small coregistration errors and image artifacts. Striping and co-registration errors were also more common in off nadir images. This reduced the number of images available for analysis.

A final limitation to note is that we assumed land cover changes in the study area (both from urban development and changes in vegetation cover such as drought-induced reductions in green vegetation) were minimal over the time series. In addition, we assumed that large scale forcings on LST patterns were similar between years (i.e., "warm" versus "cold" years). These assumptions may hold for a relatively short time series of 2.5 years of a relatively static study area, but longer analyses and/or analysis rapidly developing areas may need adjustment for land cover change/variability and for interannual differences in mean temperatures.

4.3. The relative importance of environmental drivers of LST

Urban vegetation promotes cooler surface temperatures as vegetation shades the surface and modifies the surface energy balance by increasing evapotranspiration (Oke et al., 1989). These two mechanisms reduce the daytime heating rate of urban green spaces, resulting in cooler temperatures in vegetated parts of a city. We observed that vegetation

cover reduced the average diurnal range of LST by 4.9 ℃, with a maximum ΔLSTveg of 7.3 ℃ near spring-summer solar noon. Our estimate of ΔLSTveg was lower than estimates from fine scale airborne sensors measured during the height of the summer (10 to 12 ℃, (Wetherley *et al.*, 2018)), but higher than estimates from coarser satellite sensors such as MODIS (4 to 5 ℃, (Duncan *et al.*, 2019)). This range of estimates supports results in Hu & Brunsell, (2013), which showed effects from spatial scale in measuring contrasts in urban LST. Trees maintained strong positive cooling (ΔLST < -4.0 ℃ px^{-1}) for a longer period of the day between 8:00 to 16:00 PST compared to 10:00 to 16:00 PST for Grass. Change in ΔLSTveg was nonlinear with vegetation cover, with the strongest change in LST observed between green cover fractions of 0.3 and 0.7 and weaker change in ΔLSTveg observed at more extreme green cover fractions. This suggests that a minimum amount of green space per unit urban area is needed to achieve cooling from vegetation (approximately 30%). This supports results in (Yan *et al.*, 2019) which showed that cooling from vegetation is highly variable based on vegetation patch size and complexity.

During spring-summer, the diurnal course of ΔLSTveg was also nonlinear. The strongest change in ΔLSTveg was observed between 8:00 and 11:00 PST to a peak near solar noon, with weaker change in ΔLSTveg in the afternoon. This is consistent with the contrasts in dLST/dt intensity observed between morning and afternoon. Thus, we posit that the cooling effect of vegetation occurs primarily as a result of suppressed morning heating rates for vegetated surfaces but declines more slowly in the afternoon as heat is distributed from warmer surfaces and as the surface dries and evapotranspiration rates fall. In fall-winter, the time course of ΔLSTveg is more linear with more consistent morning increases in ΔLSTveg and symmetrical decreases in ΔLSTveg after solar noon.

Surface geometry results in shading, which suppresses daytime heating rates resulting in cooler LST for shaded patches. Surface geometry also promotes multiple scattering of emitted longwave radiation, which suppresses nighttime cooling by trapping heat near the surface. This is a primary driver of both surface and air nighttime urban heat island effects, particularly for densely built areas with tall buildings narrow streets (Oke, 1988). At the city scale, we observed cooler daytime LST and warmer nighttime LST for frequently shaded classes (e.g. Road/Rail, Other Paved), consistent with results in Christen et al., (2012).

Relatively high daytime LST was observed for buildings as this class was dominated by rooftops which are less likely to be shaded and often highly insulated, resulting in high LST for the "skin" of the rooftop. However, LST decreased with mean building height, indicating that taller buildings (which are, in theory, subject to less shading) have lower morning heating rates. This likely occurs because as mean building height increases, so does the standard deviation of building height (slope = 0.67 m m^{-1}, $r = 0.77$, $p < 0.01$). Increased sub-pixel roughness promotes shade and cooler LST.

In contrast to Crum & Jenerette, (2017) and Wetherley et al., (2018), we found that trees were on average 3.5 ℃ cooler than grass by day. This may have been influenced the slightly coarser pixel size of our imagery, in which nearly pure tree pixels are dominated by large stands of trees and closed canopies, which maintain cooling throughout the day. Street trees laid out one-by-one lining a street, for example, may be subject to more intense insolation and less shade than closed canopy forest patches, however this may be offset by increased turbulent heat transfer and higher sky view factor. We also observed cooler tree LST at night compared to grass. This was unexpected as multiple emission by trees causes radiation trapping and suppressing nighttime cooling rates in tree canopies. However, most

trees in the study area are taller than their surrounding buildings (Wetherley, 2018), leading to a larger sky view factor and stronger nighttime cooling. This offsets radiation trapping within the canopy as the portion of the tree "seen" by the sensor is open to the sky and cools quickly at night.

Of similar importance to land cover drivers was proximity to water, which strongly controlled the range of LST. Proximity to coast reduced the diurnal range of LST on average by 5.5 K, primarily from a reduction in daytime LST, with daytime coastal LST on average 4-7 ℃ cooler than inland areas. LST and the diurnal range of LST increased linearly with distance to coast from 0 km to approximately 20 km from the coast, indicating the extent of the effect of the sea breeze on the land surface. The effect of distance to coast was strongest for North-South oriented coastline.

5. Conclusions

In this study, we set out to fulfill three goals. First, we sought to map the diurnal development of urban LST to identify the development of spatial contrasts in urban LST over the course of a day. We found that two years of ECOSTRESS data was sufficient to accurately resolve patterns of urban LST at a 2-hour diurnal resolution. Increased uniformity in seasonal and diurnal sampling would greatly aid this process, as the minimum time interval is determined by the period with least sampling (i.e. the lowest common denominator). Second, we used the composited diurnal time series of LST to develop diurnal curves of LST for common urban land cover types. This allowed for investigation of relative LST and cooling/heating rates over a full diurnal cycle. We found good agreement in the timing of minimum/maximum LST and magnitudes of class differences in LST between

curves derived from ECOSTRESS data and in-situ and model-assisted diurnal curves. Finally, we used a regression analysis to investigate the relative effects of environmental drivers on urban LST over the course of a day. We tracked the difference in LST between impervious and vegetation cover as a function of season, time of day, and sub-pixel vegetation cover to provide a comprehensive analysis of the cooling effect of vegetation over space and multiple time scales. We also developed diurnal curves of the forcings exerted by different land cover and topographic/morphological drivers on urban LST.

Urban areas present a particularly difficult set of challenges for thermal remote sensing. Significant progress has been made to understand the relationship between satellite sampled LST and ground-level air/surface temperature measurements (Stoll and Brazel, 1992; Schwarz *et al.*, 2012), to estimate errors from atmospheric/emissivity correction and from surface geometry (Voogt and Oke, 2003), and to investigate spatial and climatological patterns of urban land cover and climate (Zhao *et al.*, 2014). However, there remain large gaps in sampling, particularly of urban geometry and of the diurnal cycle of LST. ECOSTRESS is well equipped to help to fill those gaps by sampling over a wide range of times of day and a wide range of sun-surface-sensor geometries. In addition, ECOSTRESS is near-global mission, making it useful for developing comparative climatologies of urban temperatures and to predict urban heat vulnerability and energy demand. ECOSTRESS also has utility in defining the seasonal and diurnal shape of urban climate phenomena such as the surface urban heat island effect and the cooling effect of urban vegetation. This is particularly useful as observational and modelling tools for monitoring urban heat, forecasting urban weather, and siting heat and pollution mitigation infrastructure become more complex and require more detailed spatial and temporal information.

In conclusion, the ECOSTRESS mission provides a unique opportunity to investigate diurnal patterns of urban climate as it samples urban LST over a wide range of times of day at fine spatial resolution. Thus, ECOSTRESS allows for a more complete analysis of diurnal and seasonal spatial patterns of urban LST and its relationships with environmental drivers. We argue that the ECOSTRESS mission is of particular interest to the urban climate community for asking difficult and unresolved questions about spatiotemporal patterns of urban climate phenomena and about the driving mechanisms behind urban microclimates.

Chapter 3: Using surface-sensor modeling and time-series ECOSTRESS imagery to measure facet-scale temperatures and angular effects on urban land surface temperature.

With Dar Roberts, Charles Jones, Joseph McFadden

Abstract

Angular effects on urban land surface temperature (LST) are a well-documented source of both error and signal in measurement of urban surface climates. In this paper, we used a combination of time series ECOSTRESS imagery over New York City, New York, USA and Los Angeles County, California, USA with high spatial resolution land cover and surface morphology datasets to calculate sub-pixel fractions of "seen" wall for the unique per-pixel surface-sensor geometry in each image. We then investigated variability in seen wall fractions as a function of image surface-sensor geometry and surface morphology metrics. Next, we extracted sub-pixel facet-scale directional wall LSTs and considered the diurnal evaluation of wall temperatures compared to other common urban facet types. In addition, we binned the time series of ECOSTRESS imagery by surface-sensor geometry and overpass time to quantify magnitudes of effective anisotropy as a function of sensor zenith/azimuth angles and surface morphology. Finally, we used estimates of effective anisotropy to map the spatial distribution of angular effects on measured ECOSTRESS LST at neighborhood scale for morning, afternoon, and night overpasses. Results indicate that angular effects are minimal for sensor zenith angles < 12 degrees and increase linearly with surface roughness (i.e., complete surface area, building height) and sub-pixel wall fraction. Clear separation was observed between distributions of roof and road LSTs and directional east- and west-facing wall fractional LSTs, particularly in afternoon imagery in NYC. Directional contrasts in LST contributed to large anisotropies (>1 standard deviation of LST) in measured urban LST for images with mean sensor zenith > 12 degrees, with increasingly large angular effects with surface complexity and building height. The influence of tree canopy cover, surface

structure, and street grid orthogonality were readily observed as differences in directional LSTs in the afternoon between the two study areas.

1. Introduction

The unique materials and complex geometry of cities result in distinct and highly variable urban climates. This leads to a modified surface energy balance and generally higher surface and air temperatures in cities (Oke, 1982). Spatial and temporal patterns of urban heat are often using thermal imagery from satellite platforms. These measurements are particularly useful as land surface temperature (LST) is a key driver of the surface energy balance and has an important role in determining energy and water use, human health, and turbulence in the surface layer. Remotely sensed LST is most frequently measured using satellite-based narrow field-of-view (FOV) thermal scanners. These sensors cover a range of spatial and temporal resolutions, from high-frequency coarse-scale imagery (Moderate Resolution Imaging Spectroradiometer (MODIS), Geostationary Operational Environmental Satellite (GOES)) to low-frequency fine-scale imagery (Landsat). Ease of access, data availability, and increased computational power have led to a rapid increase in the use of satellite retrieved thermal imagery for measuring phenomena in urban climate, particularly over the last decade (Weng, 2009; Zhou *et al.*, 2019). Satellite thermal imagery have been used extensively in urban applications such as mapping and tracking the urban heat island effect (UHI) (Bechtel *et al.*, 2019), estimating outdoor water use (Reyes *et al.*, 2018; Wetherley *et al.*, 2018), land cover change, and vegetation stress (Weng *et al.*, 2004; Allen *et al.*, 2021). However, our knowledge of urban LST is biased towards the dimensions and times for which data are available (Sobrino *et al.*, 2012). For example, there is far more data available to describe inter-/intra-city spatial variability than there is to investigate diurnal differences in LST. Thus, there remain significant gaps in our understanding of patterns of

urban LST across spatial (e.g. facet-scale variability in LST), temporal, and geometric dimensions – particularly with respect to the latter two dimensions (Voogt and Oke, 2003).

Gaps in spatial and temporal sampling have received significant attention in the literature. This has led to the development of empirical time/space downscaling methods (e.g., Diurnal Temperature Cycle (DTC) models (Huang *et al.*, 2016), spatial disaggregation algorithms (Weng and Fu, 2014; Sismanidis *et al.*, 2017)), the development of harmonized and smoothed analysis-ready LST products (e.g., MODIS 8-day LST products, disaggregated 30 meter Landsat 5/7/8 LST), and more complex retrieval algorithms that account for the wide range of urban material properties to constrain and minimize biases from LST retrieval (e.g., the MODIS MOD21 LST products, which allow emissivity to vary dynamically reducing retrieval error in highly complex urban environments). While these advancements have been useful for gap filling in time and space and for constraining retrieval errors, they do not address the physical limitations in sensor design that often preclude measurement of vertical and sloped facets of the urban surface. This is in spite of the fact that these constitute a large proportion of the total urban surface area and, therefore, have a strong effect on surface-atmosphere energy exchanges (Voogt, 2000).

Geometric biases in urban thermal remote sensing arise from limitations inherent in the design of satellite remote sensors, which use a narrow-FOV detectors and often concentrate sampling to near-nadir views to reduce variance in view angle and ground instantaneous FOV (GIFOV) over a scene. In cities, where the surface is dominated by complex 3-dimensional geometry, this results in a geometric undersampling of vertical facets such as walls, tree canopies, and sloped roofs. This undersampling results in a sampling bias towards surfaces that are pointed towards the sensor, and, thus, a directional dependence of

measured LST depending on a wide range of factors including surface morphology, time of day/season, background climate, and sun-surface-sensor geometries (Lagouarde et al., 2004). This effect is conceptually similar to the bidirectional reflectance function in remote sensing of reflected solar radiation.

The directional dependence of remotely measured urban LST is termed effective anisotropy as it represents a directionality not of the surface itself, but as a result of a combination of surface morphology and narrow-FOV sampling. Effective anisotropy has been observed primarily at small scales using ground-based and airborne based measurements (e.g., helicopter) or at whole-city-scales. Anisotropy is generally quantified as the maximum difference in measured LST of an urban patch depending on view zenith/azimuth for a given observation time. Observational studies indicate that the magnitude of urban effective anisotropy can be as large as 9-14 K depending on surface morphology, land cover/materials, time of day/year, and background climate (Cao *et al.*, 2019; Hu and Wendel, 2019). Modeled and measured neighborhood-scale assessments of urban effective anisotropy show that effects are largest in low-rise, densely built areas (height/width ~ 3) during clear, calm summertime conditions approximately 2-3 hours after solar noon (Krayenhoff and Voogt, 2016). Anisotropy generally increases over the course of a day, particularly in cloud-free weather as clear calm days promote the development of large contrasts in facet-scale surface temperature driven by differential illumination (Adderley *et al.*, 2015; Morrison *et al.*, 2021). Assessments at similar scale have also observed nighttime anisotropy, which generally decreases over the course of the night and has little azimuthal variability (Lagouarde *et al.*, 2012). Long-term assessment of city-scale anisotropy using

MODIS imagery have shown that anisotropic effects on satellite imagery can be as large as 9 K and can account for up to 2.3 K of variance in the UHI (Hu *et al.*, 2016).

Not only does geometric undersampling result in a measurable and potentially significant bias in remotely sensed urban LST from anisotropic effects, it also means that the temperature measured by a narrow-FOV remote sensor is often incomplete. Moreover, per-pixel LSTs may represent a different type of temperature based on the collection of facets (e.g., walls, roofs, tree canopies, roads, etc.) seen by a sensor for a particular view geometry. For example, a narrow-FOV sensor viewing a flat parking lot or grass field samples the full surface area of the patch. In this case, the complete LST (i.e., a temperature that represents the area-averaged LST of all facets in a pixel) and plan area LST (i.e., a birds-eye-view) converge and angular effects are minimal assuming all surfaces are inherently isotropic. In contrast, a sensor at nadir viewing a residential neighborhood or downtown core only measures plan-area LST, neglecting vertical facets and undersampling sloped facets. This leads to a divergence between the complete and plan-area LST based on a pixel's sun-surface-sensor geometry.

This problem grows more complex when we consider the fact that per-pixel zenith angle varies both within a scene and, for sensors with wide-swaths and large scene overlap such as MODIS, between different scenes. As a result, geometric undersampling affects internal (i.e., within scene) and external (i.e., between scenes) comparison of LST. This produces a bias as the proportion of seen vertical and sloped facets increases with view zenith angle. Moreover, contrasts in facet scale temperatures vary based on time of day/year, synoptic effects and view azimuth. Ground-based measurements of facet-scale temperatures show strong contrasts in LST based on facet type and orientation and strong variability over

the course of a day (Lindberg *et al.*, 2008; Hilland and Voogt, 2020). Thus, it is exceedingly difficult to constrain and quantify angular effects on remotely sensed LST. A large amount of data is needed to account for and nullify variance from unwanted parameters. For example, disentangling spatiotemporal differences in LST at seasonal, synoptic, and diurnal scales requires multi-scale thermal imagery, a full cloud climatology, and fine-scale maps of surface structure, land cover, and tree canopy.

Thus, effects from geometric undersampling and effective anisotropy remain understudied, particularly at neighborhood-scale, largely due to gaps in data acquisition and the large number of free parameters at play in determining the LST of a single pixel. While sensors such as MODIS Aqua/Terra view the surface from a wide range of angles (view zenith of up to 65 degrees), they lack the spatial resolution to investigate neighborhood-scale contrasts and to stratify across driving variables such as surface morphology and land cover. In contrast, fine-scale ground-based analyses are often site/neighborhood-specific and restricted to specific periods in time making it difficult to generalize and scale to satellite-scale analysis. This gap in spatial/temporal scale remains a significant challenge at precisely the scale where that information is most actionable, as angular effects vary based on neighborhood- and facet-scale parameters (Voogt and Oke, 1998a, 2003). While modeled assessment has helped to fill these gaps by allowing for downscaling and model-assisted neighborhood-scale analysis (Yang *et al.*, 2021), we often lack the observational data necessary to estimate errors from parameterization and model-simplification, such as effects from translucent materials (such as tree canopies) and sub-facet-scale self-shading and atmospheric and emissivity effects (Dyce and Voogt, 2018; Morrison *et al.*, 2020).

The ECOsystem Spaceborne Thermal Radiometer Experiment on Space Station (ECOSTRESS) presents a unique opportunity to bridge gaps in observational assessment of angular effects on remotely sensed urban LST. ECOSTRESS is a five-band thermal sensor operating from the International Space Station (ISS). The precessing orbital geometry and height of the ISS results in diurnally variable overpass times and a 2-5 day overpass cycle with a relatively fine spatial resolution (sampling resolution of 69 x 38 m at nadir with products resampled to 70 x 70m). In addition, the combination of a relatively wide swath (384 km) and low orbital height (400 km) result in per-pixel view zenith angles of up to ~32 degrees. This produces a potentially large range of angular effects across a single scene and between scenes, with the spatial scale necessary to stratify at neighborhood-scale across a suite of land cover and surface morphology variables. In this paper, we used a 2.5 year time series of ECOSTRESS with high spatial resolution land cover and LiDAR-derived datasets to: (1) estimate per-pixel fractions of seen wall using a sun-surface-sensor model and the fine-scale LiDAR and land cover information; (2) extract and compare diurnal distributions of fractional wall temperatures to other impervious cover types as a function of sun-surface-sensor geometry; and (3) quantify and map neighborhood-scale anisotropic effects and their distributions across metrics of surface morphology.

2. Study Area and Methods

2.1 Study area

We defined two study areas shown in Figure 1: New York City, New York, USA; and Los Angeles County, California, USA. We chose these two study sites as they are highly urbanized and represent a wide range of urban land cover proportions and surface

morphologies. New York City (NYC) has a humid subtropical climate (Köppen class: Cfa) and is punctuated by very densely built high rise neighborhoods, particularly in the downtown core (Manhattan). Los Angeles County (LA County) has a Mediterranean climate (Köppen class: Csb) with strong contrasts in temperature and moisture along a coastal gradient. LA County is dominated by a mixture of low-rise hardscape dominated neighborhoods and highly vegetated neighborhoods near the coast.

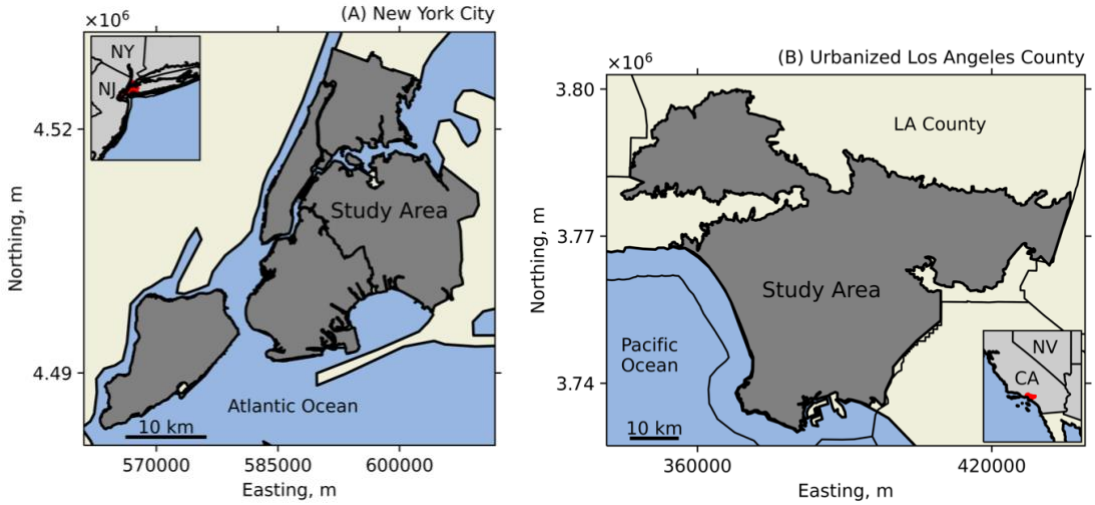

Figure 1: (A) New York City study area, (B) Urbanized Los Angeles County study area.

2.2. LST Imagery

ECOSTRESS has been operational since July 2018. LST products are generated using temperature emissivity separation (TES) with precision and accuracy at 300 K of approximately 0.15 K and 0.5 K and a band averaged noise equivalent differential temperature (NEDT) of ~0.1 K (Hulley *et al.*, 2019; Hook *et al.*, 2020). We used the Application for Extracting and Exploring Analysis Ready Samples (AρρEEARS) maintained by the Land Processes Distributed Active Archive Center (LP DAAC) to download all ECOSTRESS geolocation (ECO1BGEO) and level 2 LST, quality control (ECO2LSTE), and

cloud (ECO1BCLD) products from July 2018 through mid-January 2021 for both study sites. We then used the processing chain described in the following sections to pre-process and coregister the time series LST imagery.

2.2.1. Quality Control

ECOSTRESS products come with radiometric and cloud quality rasters. We used these to filter the stack of images based on pixel counts before entering the processing chain. To ensure consistent coverage and mask fully clouded imagery, we used counts of quality and cloud-free pixels to filter out images with <95% LST coverage and >5% cloud coverage within the study area. ECOSTRESS relies solely on emissivity and LST information to calculate a cloud mask and is susceptible to false negatives with thin cloud cover and when the surface is isothermal. To ensure cloud-free coverage in the remaining images, we manually inspected each image and removed images with >5% cloud coverage. During this process, we also tagged images for artifacts such as striping (which occurs in 5-10% of images) and major coregistration errors (which occur in 15-20% of images). Counts of images at each stage of quality control and their seasonal distributions are found in Table 1.

Table 1. Counts of images in the three major steps of the pre-processing chain.

Stage	New York City	Los Angeles County
Raw	395	532
>95% Complete	149	206
<5% Cloud	42	88
Winter	14	10
Spring	3	16
Summer	17	31
Fall	8	31

2.2.2. Spatial Nudging

Coregistration errors in ECOSTRESS imagery appeared as row/column shifts over the scene. These occur because of inconsistencies in the ISS position, which makes stable georegistration difficult. While image blur increased with view zenith angle (as is true with other wide-swath sensors, such as MODIS), coregistration errors appeared to be randomly distributed across sensor-surface geometries but were more common in partially cloud-contaminated scenes. Row/column shifts were as large as a kilometer but were generally <5 pixels in either direction. To correct coregistration errors, we implemented a cost-function approach, which used a subset of the scene with consistent linear contrast in LST to nudge the target poorly coregistered image across rows and columns while seeking to minimize the difference in contrast between the target poorly registered image and a reference well-registered image.

We first manually identified an approximately 100x100 pixel subset of the image with high contrast in LST. We found that the process was most effective when centered over complex, high thermal contrast linear features that move diagonally across the scene, as this

allowed for simultaneous correction of both row and column shifts. In both NYC and LA County, we chose a subset that straddled the coastline. After identifying an image subset, we selected a reference scene with good georeferencing by comparing a series of near-nadir scenes to a 10m USGS shoreline shapefile.

Using our image subset and reference image, we then produced a binary reclassification of the reference image using the median subset LST as a threshold. As the subsets for LA County and NYC were both centered over the coastline with approximately equal areas of water and land, their LST distributions are highly bimodal, which allowed for easy binary reclassification. After processing the reference subset, we entered the main nudging subroutine, which applied the same reclassification steps iteratively to each image identified as poorly registered. To account for diurnal and multi-seasonal sampling (in which the water and land experience an inversion in LST), we calculated mean LSTs for the left and right extremes of the imagery, which in represent average land and water temperatures. If the rank order of those LSTs did not match the reference image a flag was raised to invert the binary classification. To find the optimal row/column shift, we then nudged the target image over the reference image by moving across rows and columns and taking the sum of the squared difference between the two binary images. A total of 400 pixel shifts were tested for each target image (from a shift of -10 pixels to +10 pixels in both row/column directions) and the optimal shift was selected based on minimum sum of squared differences. An example subset showing pre-shift and post-shift imagery is included in Figure 2.

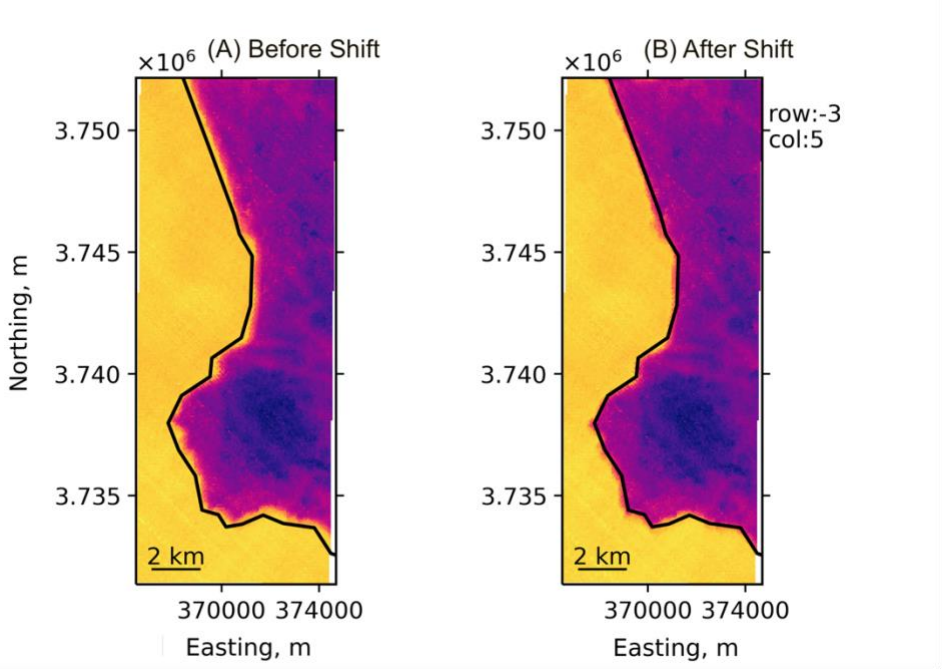

Figure 2: Pre-shift (A) and post-shift (B) subsets for a representative LA County image. Colors are unscaled LST values (purple = cool, yellow = warm). This image had a -3 row, +5 column shift.

This method for calculating optimal image row/column shifts fails when spatial contrasts in LST are too small. Under clear sky conditions this means that the method will likely to fail at overpass times close to sunrise and sunset, when the differential heating/cooling rates of surfaces of high and low thermal mass force most of the scene close to isothermality. The spatial nudging routine also fails on imagery with striping or other image artifacts, which causes the algorithm to fail to converge on a reasonable solution. After applying the algorithm, the NYC time series had 22 images with pixel shift corrections, with an average row shift of 2.9 pixels and an average column shift of 2.9 pixels. The LA County time series had 25 images with pixel shift corrections, and an average row shift of 3.3 pixels and an average column shift of 4.2 pixels.

After spatial nudging, we applied final preprocessing steps to the images by clipping and masking for the study area and stacking the imagery with its corresponding metadata.

2.3. Land Cover and LiDAR Data

In LA County, land cover information and a digital surface model (DSM) were acquired from the Los Angeles Region Imagery Acquisition Consortium (LARIAC) version 4 datasets, which used a combination of aerial imagery and LiDAR collected in 2014 to produce a ~0.2 m land cover classification and a ~0.7 m DSM. Classes include tree canopy, grass and short shrub, bare soil, water, building (i.e., rooftops), road/rail, other paved (e.g., parking lots, airport runways), and tall shrubs. To pre-process these datasets, we clipped the classification and DSM to the study area and reprojected both to EPSG 32611 (WGS-84, UTM z11N). We then resampled to 1m using bilinear resampling to allow for fast aggregation between the different scales used in the surface-sensor modeling and analysis.

In NYC, land cover information and a DSM were acquired/produced from datasets maintained by the NYC Department of Information Technology and Telecommunications (DoITT). DoITT produced an 8-class land cover classification, bare earth digital elevation model (DEM), and highest hit DSM from LiDAR flights in 2017-18 at ~0.15 m spatial resolution. Classes in the DoITT land cover classification are the same as LARIAC with two exceptions: (1) there is no tall shrub class and (2) DoITT produces a separate rail class. Tree and grass/shrub in the DoITT classification are distinguished using a 2.4 m height threshold. The DoITT DEM and DSM are delivered as irregular tiles and were mosaicked together and clipped to the study area, we then took the difference of the two to derive the height above

ground DSM used in this study. We reprojected the classification and DSM to EPSG 32618 (WGS-84, UTM z18N) and resampled to 1 m using bilinear resampling.

2.3.1. Surface Structure/Cover Metrics

When aggregated to the scale of a thermal image, LiDAR derived DSMs provide per-pixel statistical assessments of height above ground (i.e., central tendency, sub-pixel variance). Likewise, the aggregated land cover classification may provide a majority class, or sub-pixel fractions of land cover. It is often more useful to calculate specific metrics that summarize key features of sub-pixel surface structure, such as plan area fraction of impervious cover (λ_i) and complete aspect ratio (λ_c). When combined, these metrics can be used to delineate micro-climatically distinct neighborhoods and are descriptive enough to aid in model parameterization of surface cover and structure. To derive λ_c and λ_i for the 70 m ECOSTRESS grid, we use the two 1 m DSMs and land cover classifications. We calculated λ_c as the ratio of the total 3-dimensional external surface area (i.e., the total surface area of all elements including 3-d and 2-d elements) and the planar area of each pixel (70 x 70 m) (Oke et al., 2017). For example, $\lambda_c = 1$ for a flat surface and as the quantity and size of elements within a pixel increase (e.g., the count and height of buildings), so does λ_c. We calculated λ_i as the subpixel fractional cover of all impervious surfaces (building, road, other paved, and in NYC rail). Figures 3 and 4 show maps of λ_c and λ_i for the two study areas.

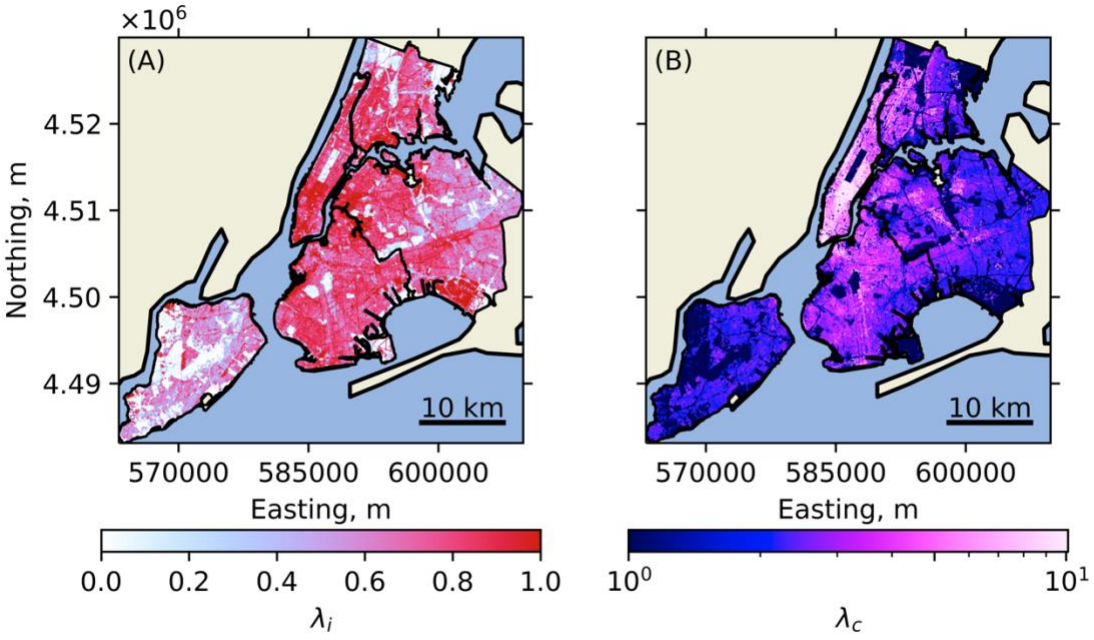

Figure 3: Maps of λ_i (A) and λ_c (B) calculated from 1 m DSMs for the 70 m ECOSTRESS grid for the NYC study area.

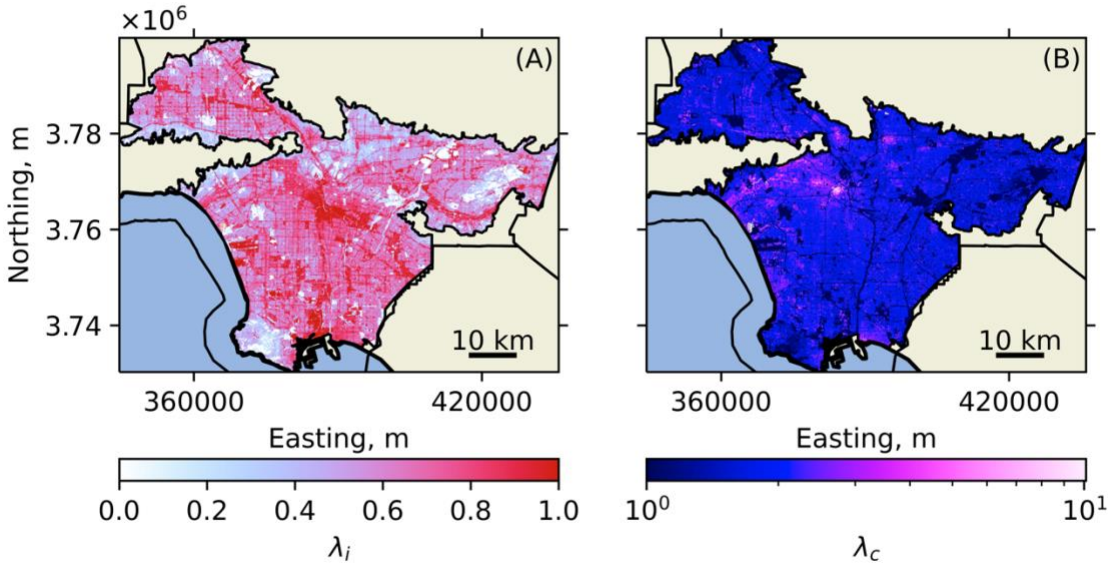

Figure 4: Maps of λ_i (A) and λ_c (B) calculated from 1 m DSMs for the 70 m ECOSTRESS grid for the LA County study area.

2.4. Surface-Sensor Geometry Modeling

To calculate and extract sub-pixel fractional wall temperatures, we used a surface-sensor model that used the fine-scale DSM to tag pixels of the 3-dimensional surface as seen or occluded based on each pixel's height above ground and the sensor view zenith and azimuth. To do this, we projected the FOV of the sensor onto the DSM twice, once with the direction of the sensor and once with the sensor on the opposite end of the sky (a difference in view azimuth of 180 degrees). The former tags pixels of the DSM as in shadow (occluded), the latter calculates wall displacements from the foot of each building. We then combined these outputs with the land cover classification to compute sub-pixel fractions of

seen wall displacement over the ECOSTRESS grid for the unique per-pixel surface-sensor geometry of each image.

To do this, we aggregated the 1m DSM to 5m to reduce noise from very small-scale structure (which tends to overamplify the amount of seen/obscured wall) while emphasizing the overall structure of the surface. To obtain the sensor view geometry for a given image, we extracted per-pixel view zenith and azimuth angles from the pre-processed ECO1BGEO layers based on the closest 70 m pixel to the location of the source pixel within the DSM. We then projected the sensor line of sight (LOS) from the height of the source pixel onto the DSM and calculated the length of shadow from the source pixel (l) at pixel i, j as,

$$l_{i,j} = \frac{h_{i,j}}{\tan\left(90 - vz_{i,j}\right)}$$

where $h_{i,j}$ is the height of the source pixel, $vz_{i,j}$ is the view zenith angle. l represents the shadow length from a given source pixel if the sensor view azimuth is parallel to the pixel grid. To discretize and distribute the shadow onto the DSM, we overlaid the shadow length from the source pixel as a vector onto the DSM grid with the direction of the view azimuth. We then tagged pixels that intersected the vector with the shadow height at their pixel centers. These tagged heights were then compared to the DSM. If the height of the shadow was greater the height of the corresponding DSM pixel, the pixel was tagged as in the source pixel's shadow. If the shadow height was less than the DSM height, the pixel was left untagged and the vector was truncated. This process was repeated for each building pixel > 2 m in height.

After calculating, discretizing, and tagging per-pixel occlusions for each image over the DSM, we followed similar steps to calculate wall displacements with the sensor on the opposite side of the sky (difference in azimuth of 180 degrees). However, when calculating wall displacements, we filtered the DSM using the land cover classification to only run the calculation on building pixels and added an additional step to store the per-pixel displacement on the source pixel as the sum of the length of the displacement. This represents the height of the wall displacement seen by the sensor for each building pixel.

Figure 5 shows a schematic of the 5m aggregated land cover classification (A) and DSM (B), and the output from the surface-sensor model (C and D) for a ~500 x 500 m subset of the NYC study area with sensor zenith angle ~20 degrees and azimuth angle of ~300 degrees. In (C), shades of blue represent the per-pixel wall displacement length converted to meters. Pixels of the DSM tagged as occluded are shaded in the red. To integrate this with the ensemble of gridded environmental variables, we combine the 5 m surface-sensor model outputs with the 5 m land cover classification by reclassifying pixels that were tagged in the model output. Pixels tagged as occluded (e.g., road pixels behind a tall building) are nullified and omitted from the aggregated totals. Seen displacement lengths are classified as an additional class and are added to the total sub-pixel area. To aggregate to the 70 m ECOSTRESS grid, we produce pixel counts of each class (including the seen wall displacement) and divide by the total number of seen pixels in each 70 m cell. This produces fractional cover of all land cover classes and seen wall displacement for the ECOSTRESS grid, with areas obscured by surface cover omitted. In rare cases, the area obscured by surface structure is larger than the displaced area seen by the sensor (generally by < 1%). In

these instances, we scale land cover fractions of each class linearly so that the sum of fractional cover in each pixel is equal to one.

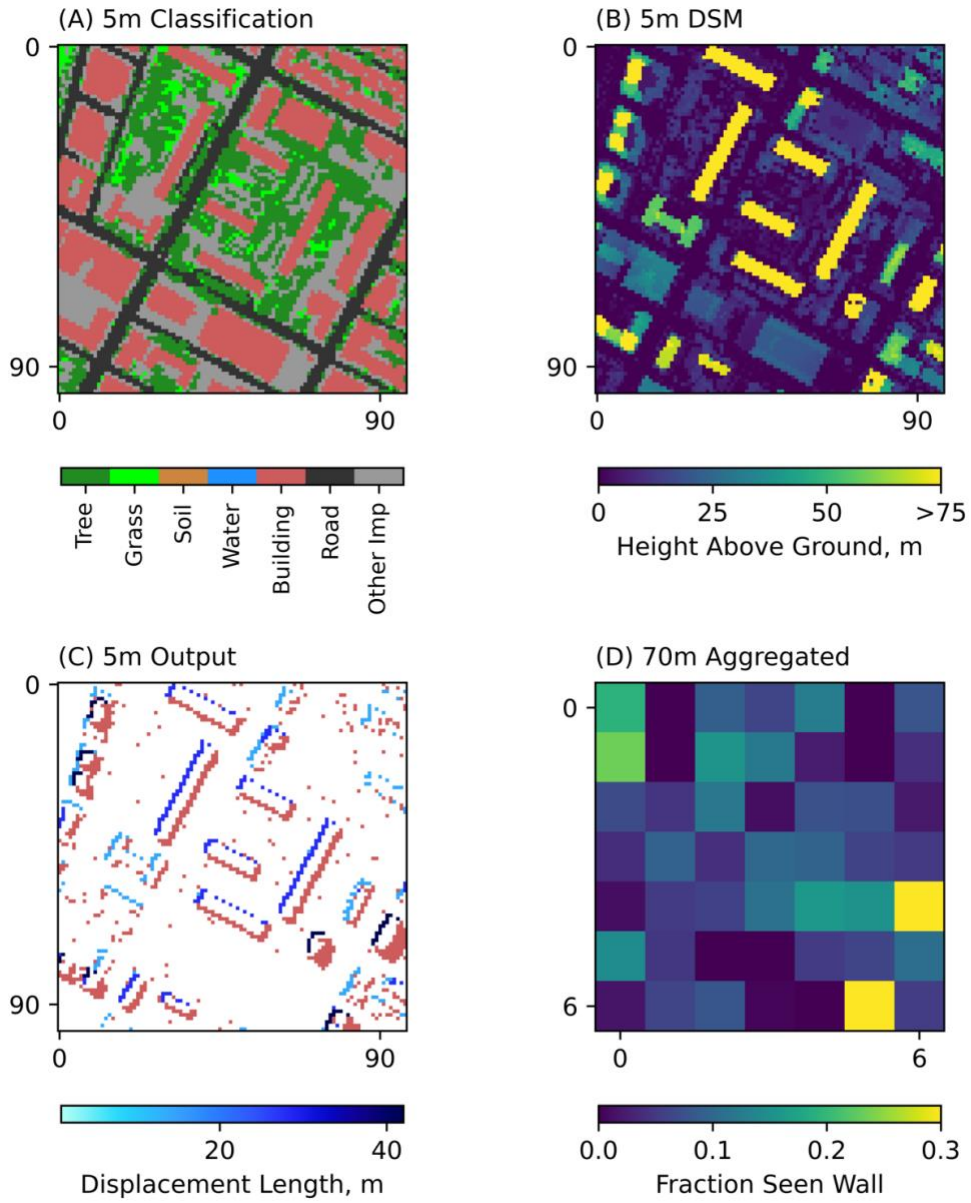

Figure 5: All subplots show the same 490 m area of the NYC study area. X/Y ticks represent counts of pixels from the upper left corner. (A) 5 m aggregated land cover classification. (B) 5 m aggregated height above ground calculated from the DSM. (C) Output from the surface-sensor model at 5 m for a view zenith angle of ~20 degrees and azimuth angle of ~300

degrees. Shades of blue represent seen wall displacement converted to meters. Pixels tagged as red are obscured by surface geometry. (D) Fractional seen wall cover at 70 m calculated from the land cover classification and surface-sensor outputs.

2.5. Data Integration and Analysis

Our analysis has four parts. First, we map and quantify relationships between surface structure metrics (namely λ_c), view zenith angle, and sub-pixel fractional seen wall. To do so, we bin pixels based on surface structure metrics and calculate mean wall fractions as a function of sensor zenith angle. Second, we extract diurnal distributions of wall temperatures for multiple surface-sensor geometries and compare them to distributions of LSTs for other facets. Third, we estimate azimuthal variability in directional LSTs at multiple times of day using differences in standardized LST over a gradient of λ_c. Finally, we use relationships between effective anisotropy and λ_c with maps of land cover and surface structure to map the spatial distribution of effective anisotropy for the two study areas. In parts two, three, and four we standardize LST for each image as,

$$Z_{i,j} = (LST_{i,j} - \overline{LST})/\sigma_{LST}$$

This Z-score standardization aids in comparison between images as the mean and variance of each LST image varies based on time of day/year and synoptic effects, which makes direct comparison of distributions of LST between images difficult. In part four, we aggregate results to neighborhood-scale using neighborhood shapefiles produced by the New

York City Department of City Planning and Los Angeles Times for visualization and to reduce pixel scale noise.

3. Results

3.1. Sub-pixel seen wall fractions

Figures 6 and 7 show the spatial distribution of sub-pixel seen wall fractions. In both figures, (A) shows sub-pixel seen wall with a small scene-average view zenith angle (i.e., near-nadir) and (B) shows a large scene-average view zenith angle (i.e., off-nadir). Seen wall fraction increased with sensor zenith angle in both NYC and LA County as the proportion of vertical facets in the FOV increased. This occurred both as an increase in seen wall fraction for pixels with very high λ_c and as an increase in the total area with observable seen wall fraction. This effect is most obvious in NYC, where the study area contains a large number of medium-rise neighborhoods ($8 > \lambda_c > 4$), which have negligible angular effects at view zenith angles < 12 degree that strongly increase at view zenith angles > 18 degrees. At large sensor zenith angles (> 22 degrees), much of the downtown core of NYC (Manhattan) has seen wall fractions > 40%.

In LA County, tall buildings are found almost exclusively in the downtown core. Thus, increasing sensor view zenith resulted in larger seen wall fractions in the downtown with minimal increases observed elsewhere. Obstruction by tree canopies (which are on average 4.8 m taller than buildings in the urbanized LA region (Wetherley *et al.*, 2021)) likely caused a further reduction in seen wall fraction. However, we note that results in Dyce & Voogt, (2018) indicate that while tree canopies reduce the fraction of seen wall facets, this does not necessarily result in a decrease in overall anisotropy.

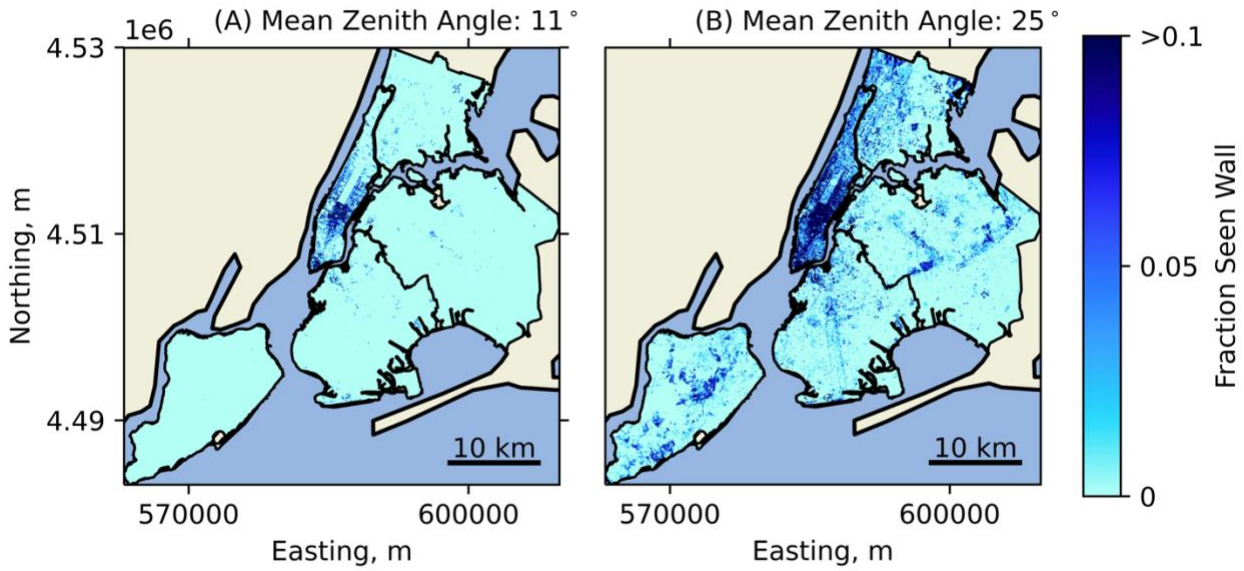

Figure 6: Sub-pixel fractional wall cover for scene average view zenith angle of (A) 11 degrees and (B) 25 degrees in the NYC study area.

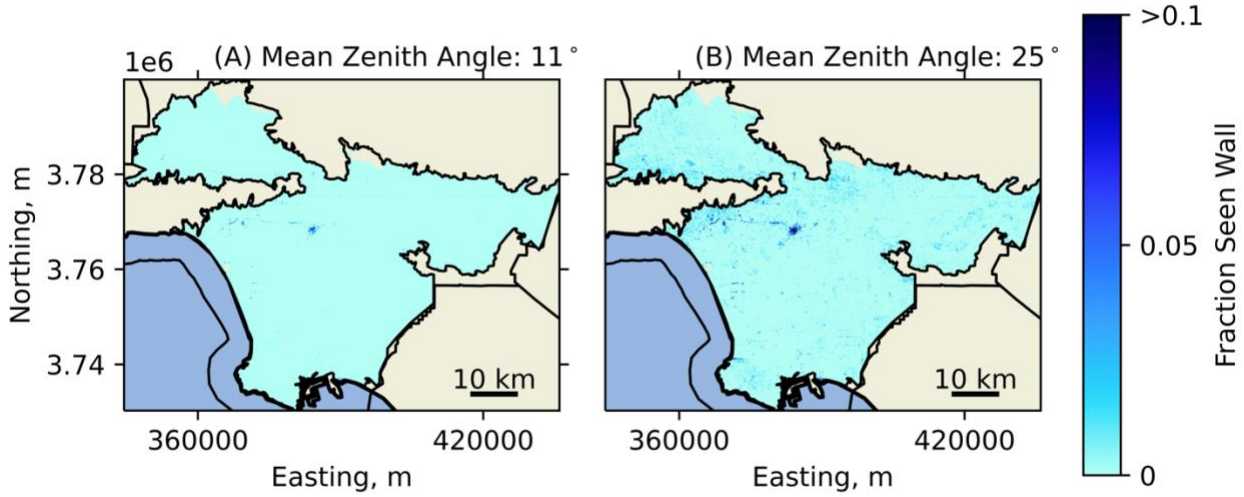

Figure 7: Sub-pixel fractional wall cover for scene average view zenith angle of (A) 11 degrees and (B) 25 degrees in the LA County study area.

As both λ_c and per-pixel view zenith angle increase, both NYC and LA County show similar patterns of increasing seen wall fraction (Figure 8). Results are less consistent in LA County, where n-samples decreases sharply above $\lambda_c = 20$. In both cases, seen wall fraction is negligible for $\lambda_c < 3$ and with view zenith < 12 degrees. Results for mean pixel height above ground (Figure 9) show slightly more linear increases in seen wall fraction with increasing view zenith. No observable relationship was found between λ_i and seen wall fraction (not shown), particularly in LA County, which is dominated by low-rise neighborhoods with high λ_i but relatively low λ_c.

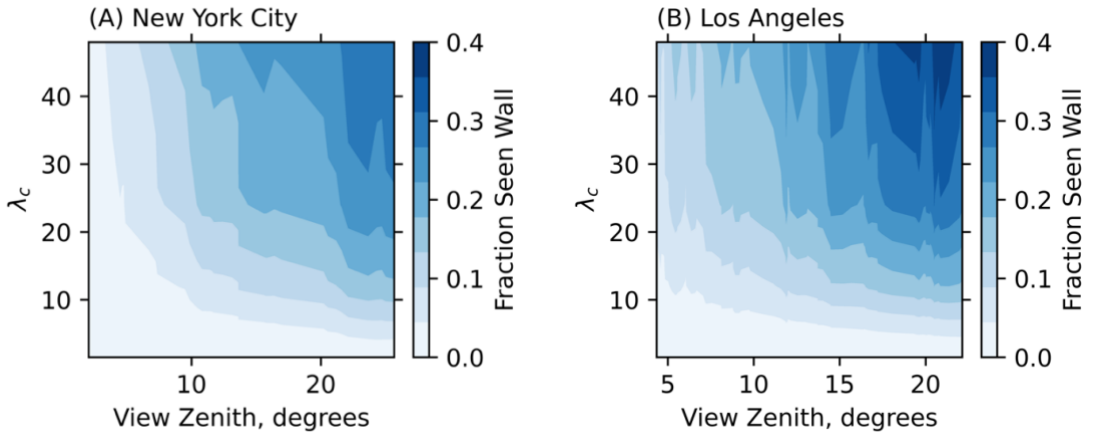

Figure 8: Seen wall fractions as a function of view zenith and binned λ_c for (A) NYC, and (B) LA County. Bins extent from 1 to 64 in increments of 2^i. Y-axis labels represent bin centers. Results are smoothed using a zero order gaussian filter (sigma = 1) for visualization.

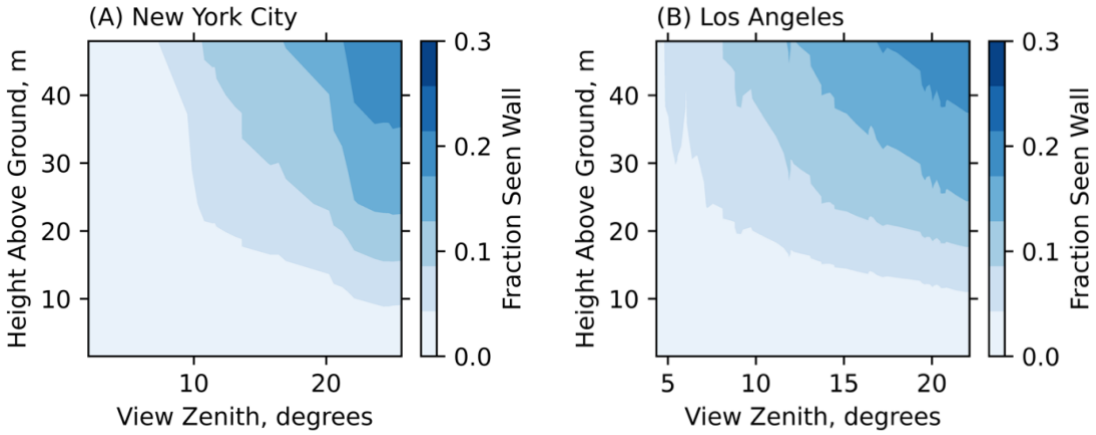

Figure 9: Seen wall fractions as a function of view zenith and binned height above ground for (A) NYC, and (B) LA County. Bins extent from 1 to 64 in increments of 2^i. Y-axis labels represent bin centers. Results are smoothed using a zero order gaussian filter (sigma = 1) for visualization.

3.2. Extracting diurnal patterns of fractional wall LSTs

To investigate wall temperatures, we first calculate Pearson's R correlation coefficients between per-pixel wall fraction and LSTs (Figure 10). We note that both sub-pixel wall fraction and LST are allowed to vary for each image (as sensor-surface geometry is unique for each overpass and each pixel), so the distribution and total amount of wall fractional cover varies significantly for each image. In NYC, we observe positive correlation between seen wall fraction and LST at night (mean R = 0.51) and slightly negative correlation during the day (mean R = -0.23). This pattern is consistent seasonally and for both small and large view zenith angles. In LA County we found no significant relationship between wall fraction and LST. This likely occurred because of a combination of highly skewed sampling (towards low wall fraction) and because variance in LST in LA County was highest at low wall fractions.

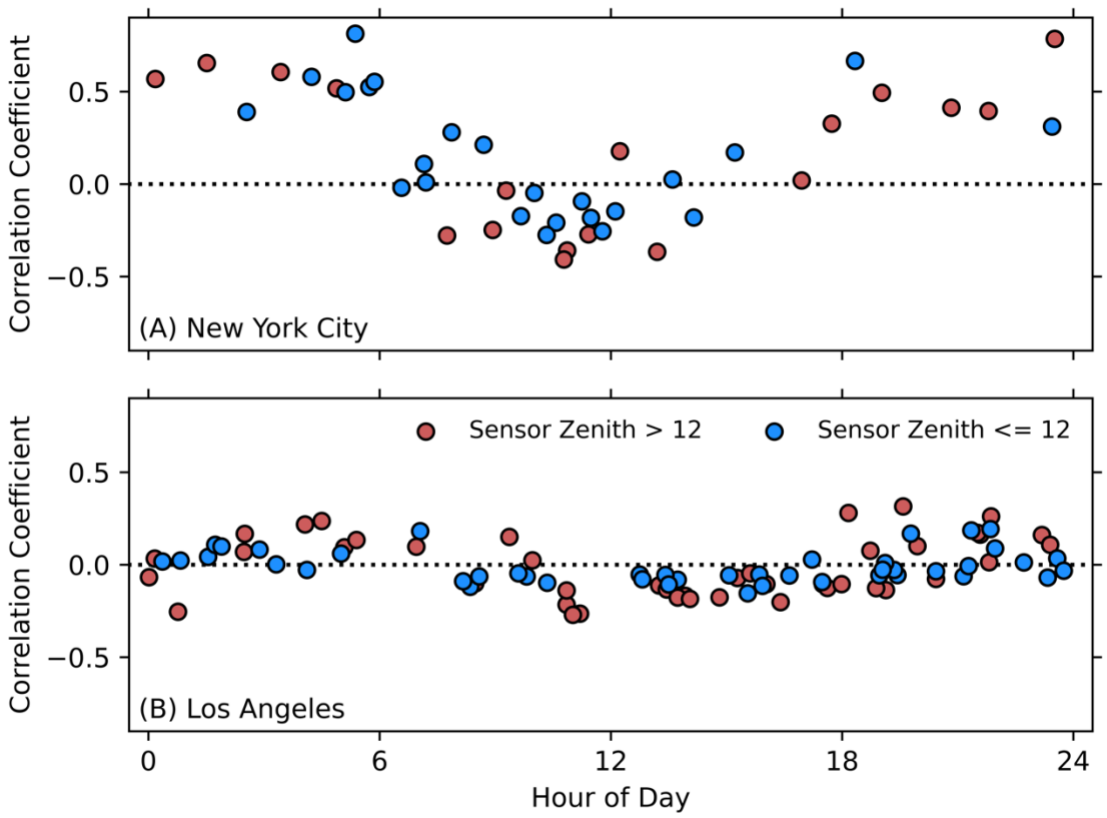

Figure 10: Correlation coefficients calculated between fractional wall cover and LST for each image. Fill colors indicate scene averaged sensor zenith angle.

Figure 11 shows distributions of standardized LSTs stratified based on time of day, sensor zenith/azimuth, and wall/roof/road fraction. All distributions are computed from pixels with $\lambda_i > 0.75$ to minimize influence from other cover types. Images were filtered to separate near-nadir images (scene average sensor zenith < 12 degrees) from off-nadir images with the sensor in the eastern half of the sky (zenith > 12 degrees, sensor azimuth < 180 degrees) and off nadir views the sensor in the western half of the sky (zenith > 12 degrees, sensor azimuth > 180 degrees). We stratified nadir views based on road and roof fractional cover using a 75% cover threshold. West and east distributions included an additional filter

to include LSTs of pixels with > 20% remaining wall fraction. We note that similar results were observed over a range of wall fraction thresholds, with n-samples decreasing sharply above the 20% threshold (particularly in LA County). Details of this sensitivity testing as well as pixel and image counts for the range of sampling bins are included in the supplemental materials. Morning represented overpass times from sunrise to noon local time, afternoon represents overpass times from noon to sunset, and night represents overpass times between 2 hours post-sunset and sunrise.

At night in both study areas, off-nadir LSTs were much warmer than nadir roof and road LSTs, likely as a result of radiation trapping and reradiation by adjacent vertical facets, which also drove slightly warmer road LSTs compared to roof. We observed slightly warmer west LSTs compared to east owing to more recent insolation in the afternoon hours. In the morning all views and cover types were approximately isothermal. Near-nadir views of road and roof were the warmest, followed by off-nadir east walls, and off-nadir west walls. In the afternoon, we observed different relationships in NYC and LA County, with much warmer west wall LSTs and cool east wall LSTs in NYC, and much warmer near-nadir roof/road LSTs and little difference between east and west off-nadir views in LA County. We hypothesize that this difference is due to differences in surface structure, street layout, and tree canopy; with densely packed orthogonal street grids in NYC leading to strong shading of roads and strong insolation of west facing walls. In contrast, lower building heights and a generally more open plan area in LA County allow for more direct insolation of roofs and roads, while a taller tree canopy and a larger fraction of low-rise residential neighborhoods (which are punctuated by strong self shading) reduced LSTs of west facing walls (Hilland and Voogt, 2020).

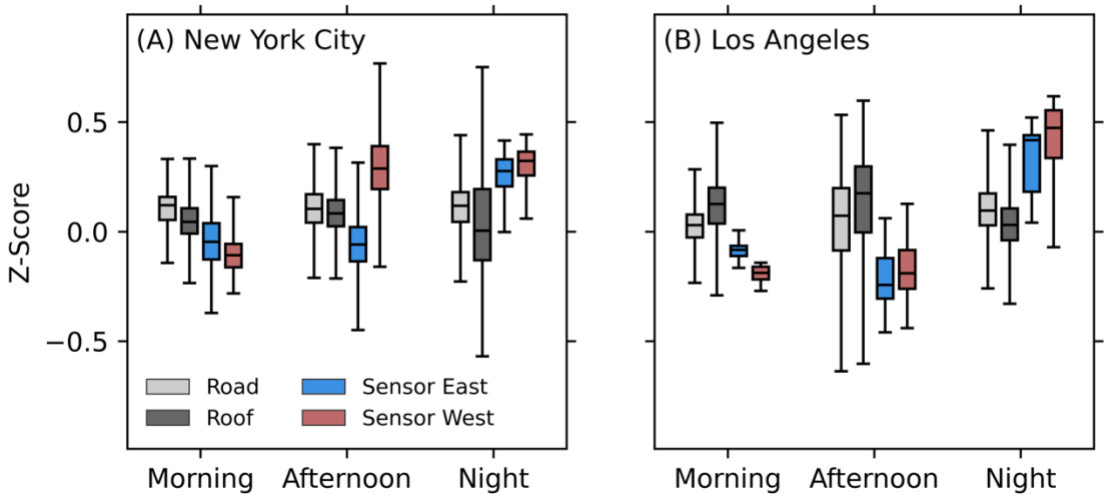

Figure 11: Distributions of standardized LSTs for nadir (view zenith < 12 degrees), and two off-nadir (view zenith > 12 degrees) sensor positions. Sensor west and Sensor east boxes represent distributions of pixels with at least 20% seen fractional wall. Pixels were filtered based on an λ_i threshold of 0.75 to minimize influence from other cover types. Nadir views were filtered for >75% Road and Roof cover.

3.3. Estimating anisotropy as a function of time of day and surface morphology

We estimate anisotropy as the mean difference in standardized LST between high λ_c neighborhoods ($\lambda_c > 6$ for NYC, $\lambda_c > 3$ for LA County) and low λ_c neighborhoods ($\lambda_c < 2$) ($\Delta LST_{\lambda c}$). These thresholds roughly approximate the 75th and 25th percentiles of the distribution of λ_c. We calculated $\Delta LST_{\lambda c}$ for each image and binned results based on time of day and for four view directions. All images in this analysis had scene-average sensor zenith angle greater than 12 degrees. Figures 12 and 13 show $\Delta LST_{\lambda c}$, with positive $\Delta LST_{\lambda c}$ indicating warmer LST for neighborhoods with taller buildings for the specific sun-surface-sensor setup, and negative $\Delta LST_{\lambda c}$ indicating relatively warmer LST for flatter, low λ_c

neighborhoods. Thus, we assume that forcings on measured LST for each view quadrant and time of day are approximately the same, so that differences in standardized LST result from a combination of illumination and view geometry. To aid interpretation, we note that $\Delta LST_{\lambda c} = 0$ indicates minimal differences in LST based on surface morphology, but not necessarily an absence of anisotropy. Rather, anisotropy appears as differences in $\Delta LST_{\lambda c}$ across azimuthal bins.

In NYC, anisotropic effects are well defined (Figure 12). In morning acquisitions, high λ_c neighborhoods are cooler when observed from off-nadir sensor positions for NW, SW, and SE view quadrants. The opposite was true for NE sensor azimuths, which observed warmer LSTs in high λ_c neighborhoods compared to low high λ_c. Negative $\Delta LST_{\lambda c}$ in the SE view quadrant was unexpected, as facets pointed towards that quadrant had on average been illuminated for approximately 2-3 hours. However, the average view azimuth (black "+") was approximately 20 degrees greater than the average sun azimuth (yellow dot). This discrepancy may have caused a differential between illuminated vertical facets and seen vertical facets, meaning that the vertical facets seen by the sensor had not yet been illuminated by the sun. We hypothesize that strong contrasts in angular differences in LST based on minute differences in sun-sensor relationships are likely in cities highly linear street grids (such as Manhattan).

In LA County, anisotropic effects are strong in morning observations but as clearly distinguished in afternoon observations. This pattern is consistent with observations of fractional wall LSTs in LA County, which were anomalously low in the afternoon compared to NYC. In the morning, we observed positive $\Delta LST_{\lambda c}$ for both NE and SE sensor positions, owing to strong illumination of vertical facets pointing towards the sensor in those quadrants.

In the afternoon, $\Delta LST_{\lambda c}$ was consistently negative for all sensor orientations save NW, which does not receive direct illumination until just before sunrise in the summer (and often does not receive any direct illumination in the winter months). This pattern in afternoon observations from the NW quadrant was also observed in wall LSTs in Section 3.2.

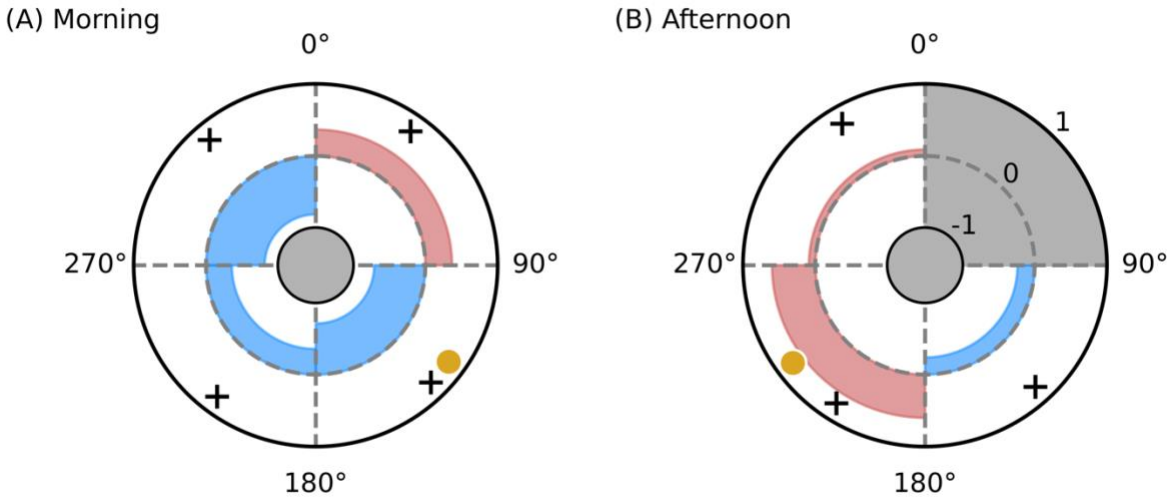

Figure 12: Polar plots of difference in standardized LST (z-score) between high λ_c ($\lambda_c > 6$) and low λ_c ($\lambda_c < 2$) neighborhoods for the NYC study area ($\Delta LST_{\lambda c}$). Results are aggregated into quartiles of sensor azimuth angle. Red shaded values indicate $\Delta LST_{\lambda c}$ above zero and warmer LST in high λ_c neighborhoods. Blue shaded values indicate $\Delta LST_{\lambda c}$ below zero and cooler LST in high λ_c neighborhoods. Black "+" marks show average quartile sensor azimuth relative to the study area. The average solar azimuth is shown as a yellow dot. Grey shaded quartiles have n-image < 2 and are omitted.

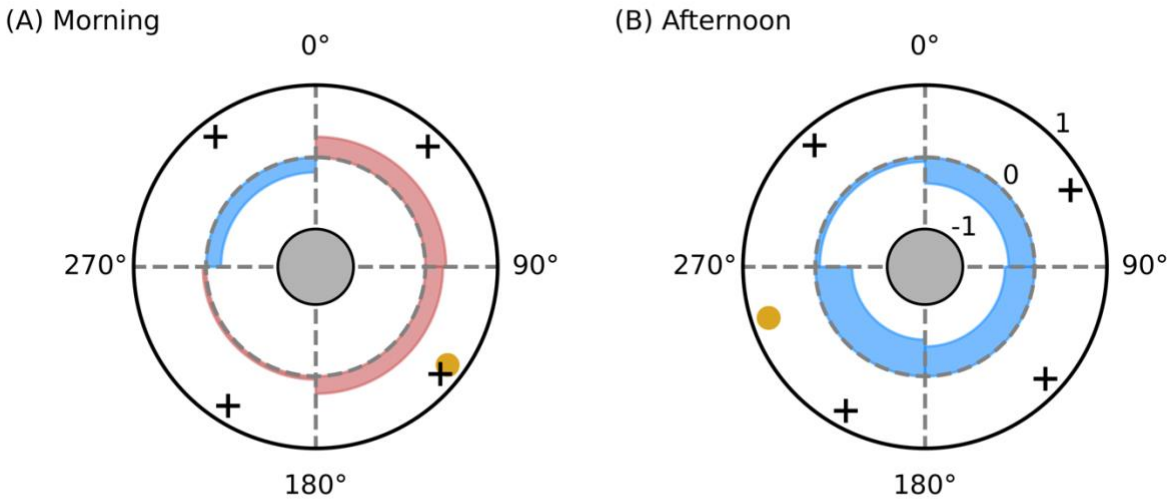

Figure 13: Polar plots of difference in standardized LST (z-score) between high λ_c ($\lambda_c > 3$) and low λ_c ($\lambda_c < 2$) neighborhoods for the LA County study area ($\Delta LST_{\lambda c}$). Results are aggregated into quartiles of sensor azimuth angle. Red shaded values indicate $\Delta LST_{\lambda c}$ above zero and warmer LST in high λ_c neighborhoods. Blue shaded values indicate $\Delta LST_{\lambda c}$ below zero and cooler LST in high λ_c neighborhoods. Black "+" marks show average quartile sensor azimuth relative to the study area. The average solar azimuth is shown as a yellow dot. Grey shaded quartiles have n-image < 2 and are omitted.

To examine the impact of surface morphology, we binned pixels by λ_c after filtering for pixels with $\lambda_i > 0.75$. We then calculated mean Z-score standardized LST for morning, afternoon, and night and the same surface-sensor setups used in Section 3.2 (Near-nadir, off-nadir sensor West, off-nadir sensor East). These are shown in Figure 14 for NYC and Figure 15 for LA County. We note that similar results were observed when plotted against mean height above ground from the DSM, with higher inter-/intra-bin variances in both cities.

In both cities, we observe positive Z-score for open, low λ_c cover in both morning and afternoon owing to increased direct insolation and low shading. In morning observations, LST generally decreased with increasing λ_c. Morning nadir and east views tracked together, with divergence and lower standardized LSTs observed for west views in both cities. This divergence was particularly large in LA, where west facing LSTs for high λ_c pixels ($Z_{max(\lambda c)}$ = -0.8) were nearly a standard deviation lower than corresponding nadir/east LSTs ($Z_{max(\lambda c)}$ = -0.1). At night results were also similar in both cities, with near-global-mean LSTs observed for low λ_c cover ($Z_{\lambda c<6}$ = ~0.0) and increasing LSTs with increasing λ_c. Higher overall variances in LST were observed in LA County compared to NYC.

Results in LA County and NYC were different in the afternoon. In LA County, LSTs from nadir and west sensor orientations tracked downward together with increasing λ_c (nadir: $Z_{max(\lambda c)}$ = -0.4, west: $Z_{max(\lambda c)}$ = -0.4). Slightly lower LSTs were observed for east views (east: $Z_{max(\lambda c)}$ = -0.7), owing to increased shading of east facing facets in the afternoon hours. In NYC, LSTs of west views tracked lower for low λ_c cover, but sharply increased as λ_c increased from λ_c = 5 to a maximum of $Z_{max(\lambda c)}$ = 0.8, indicating much warmer LSTs for west facing facets in the afternoon. While LSTs of nadir and east views did not show large change with increasing λ_c (nadir: $Z_{max(\lambda c)}$ = -0.3, east: $Z_{max(\lambda c)}$ = -0.1). This is consistent with results for fractional wall LSTs in NYC observed in Section 3.2.

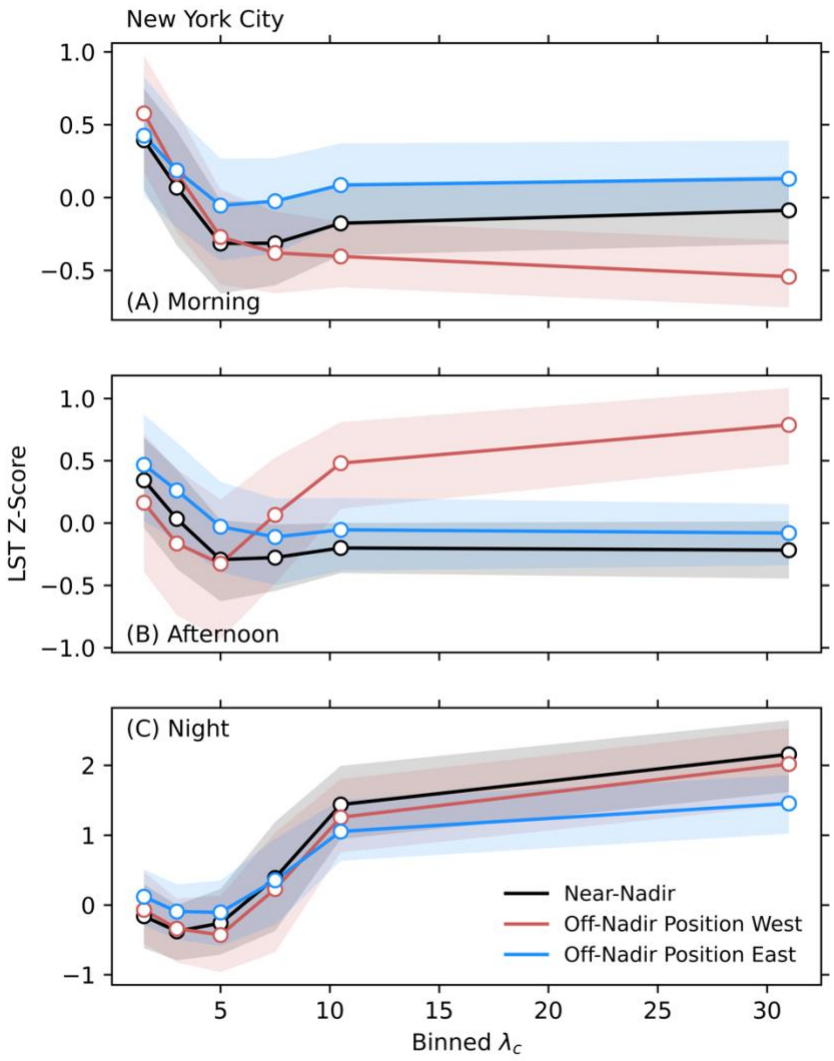

Figure 14: Mean Z-score standardized LST binned based on λ_c (lines) and interquartile range (shading) for NYC. X-axis labels represent bin centers.

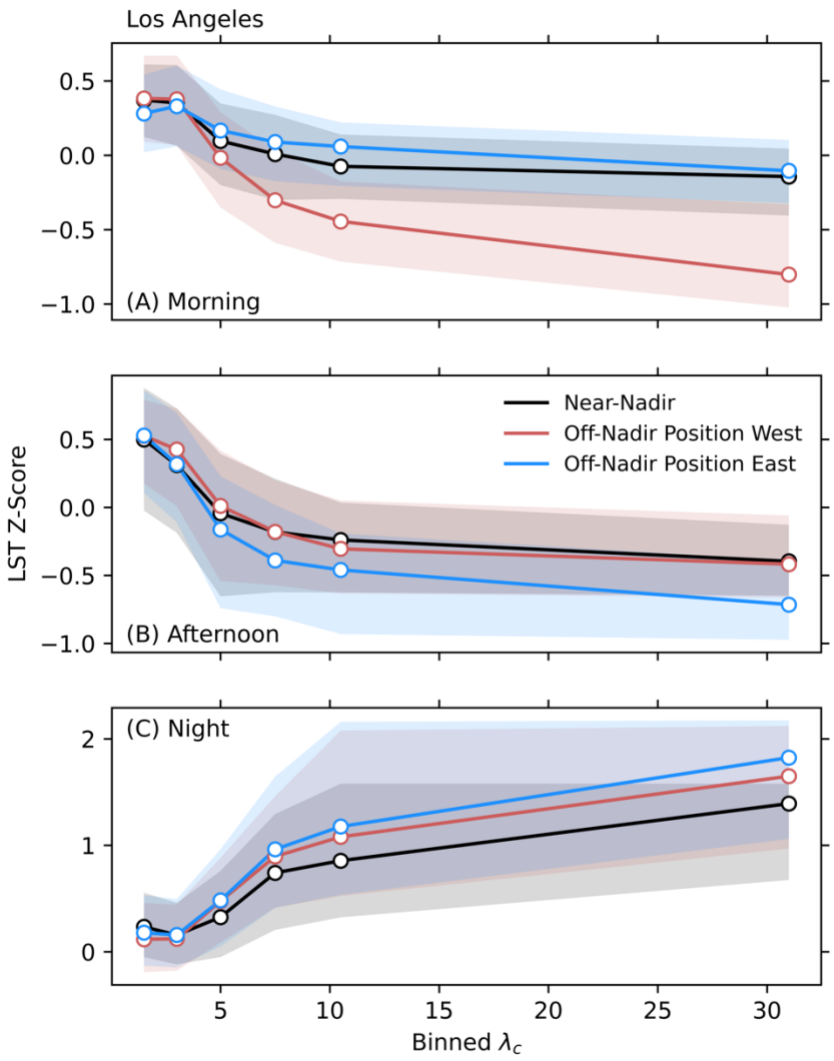

Figure 15: Mean Z-score standardized LST binned based on λ_c (lines) and interquartile range (shading) for LA County. X-axis labels represent bin centers.

3.4. Mapping anisotropy as Z-score divergence based on neighborhood-scale surface morphology

The magnitude of effective anisotropy (Λ) is generally estimated as maximum difference in LST over all view geometries for a single sampling period (Krayenhoff and Voogt, 2016). Based on this, we estimate magnitudes of anisotropy based on the maximum difference in Z-score standardized LST between the three view geometries for each time of day and for each bin of λ_c (i.e., the absolute values of differences between lines in Figure 14 and 15) as $\Lambda = \max(Z_{\lambda c}) - \min(Z_{\lambda c})$. We then calculate neighborhood λ_c and λ_i using zonal means and match each neighborhood with its binned estimate of Λ. These results are shown in Figures 16 and 17. For mapping neighborhood Λ estimates, the λ_i threshold was relaxed to 0.6 (from 0.75) to account for the fact that many neighborhoods include larger patches of vegetation. Grey shaded polygons represent neighborhoods $\lambda_c < 0.6$ which were omitted from the sample.

We observed large neighborhood-scale spatial contrasts in our binned estimates of Λ as a function of λ_c in NYC. These are particularly apparent in Manhattan, where many neighborhoods are dominated by high λ_c. Λ was highest across the study area in the afternoon, with more modest A at night and in the morning. $\Lambda > 0.5$ was observed consistently throughout the day/night in the downtown core of Manhattan (mean polygon λ_c ~20-50). A was very low throughout LA County, likely owing partially to the fact that areas of high λ_c (primarily the downtown core) are split between multiple polygons. In spite of this, differences in λ_c across the study area and time-dependent differences in the relationship

between λ_c and LST do force small neighborhood-scale contrasts in Λ. In particular, between the downtown core and the surrounding lower λ_c neighborhoods.

We note that these estimates do not explicitly include anisotropic effects from tree cover, as λ_c is calculated from building heights alone. Thus, we likely underestimate anisotropy in tree covered neighborhoods, particularly in LA County where residential neighborhoods are often accompanied by tall trees.

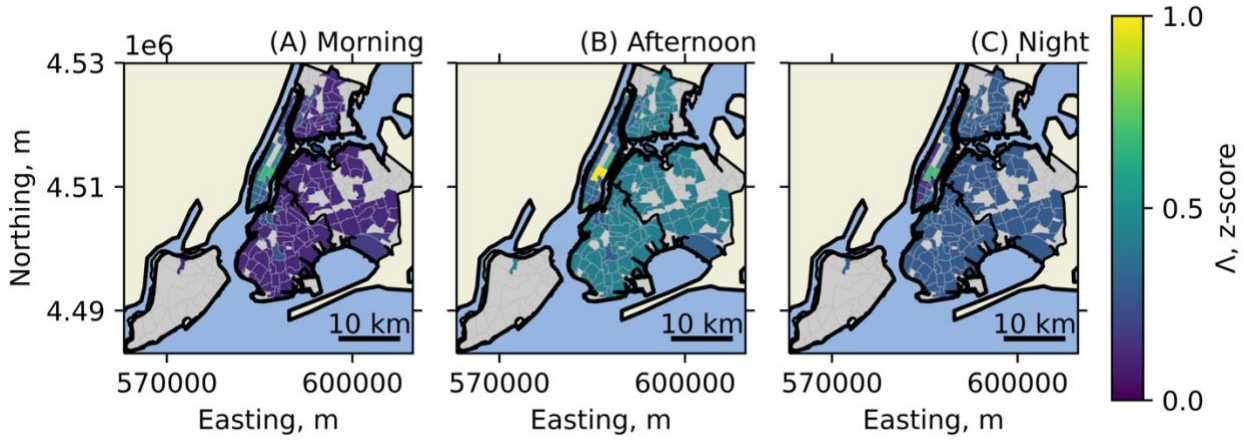

Figure 16: Λ estimated at neighborhood scale in NYC from binned estimates of the difference between maximum and minimum Z-score standardized LST for different surface-sensor setups. Grey polygons were omitted based on $\lambda_i < 0.6$.

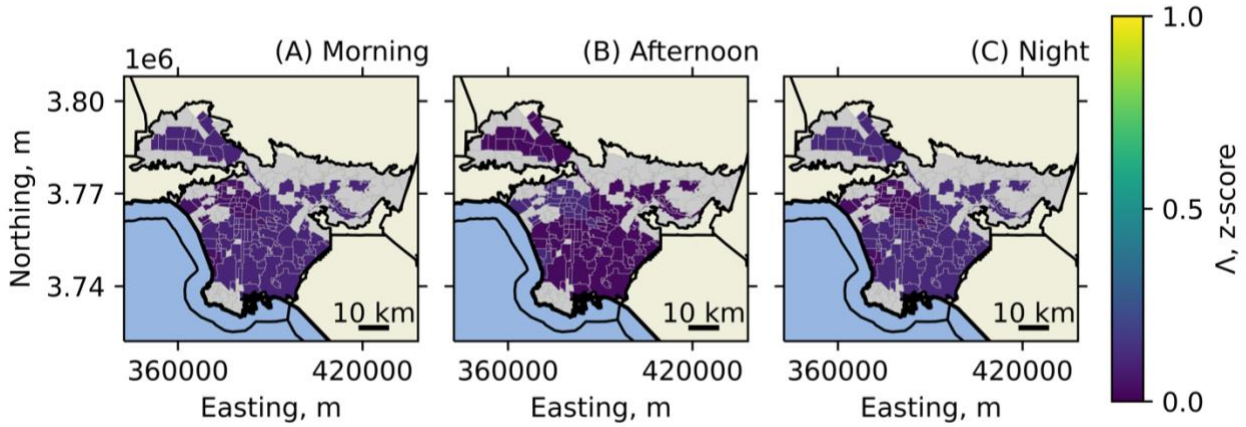

Figure 17: Λ estimated at neighborhood scale in LA County from binned estimates of the difference between maximum and minimum Z-score standardized LST for different surface-sensor setups. Grey polygons were omitted based on $\lambda_i < 0.6$.

4. Discussion

Inter-facet contrasts in LST form the basis of directional differences in remotely sensed LST and are an important driver of exchanges of energy between the surface and the atmosphere and within the lowest layers of the boundary layer. While micro- and facet-scale contrasts in urban LST have received significant attention in the urban climate literature from ground-based and modelled studies (Soux *et al.*, 2004; Christen *et al.*, 2012; Morrison *et al.*, 2021), they have largely been neglected in satellite-based analysis of urban climate. We posit that this, in part, has led to the development of a significant knowledge gap between largely empirical satellite remotely sensed study of urban climate (i.e., the forest) and micro-scale process-based study of urban climates (i.e., the trees). This gulf in understanding will only grow larger as the volume of satellite-based remotely sensed LST data grows and as instrument (e.g., handheld thermal scanners) and computational model improvements allow

for finer and more accurate portrayals of complex urban form and function. Integrating and synthesizing between these perspectives, methods, and independent sets of terminology represents a significant challenge for the urban climate community. Unique datasets such as that produced by the ECOSTRESS sensor present a highly useful tool for bridging and assessing the gaps in observational knowledge and process-based understanding.

4.1. Inferring scene-specific LSTs from Z-score metrics

In our analyses we used Z-score standardized LSTs because both the mean and standard deviation of LST are scene specific and change based on factors outside of the scope of the study (e.g., synoptic and seasonal variability in LST). By converting to Z-score, we preserve contrasts in LST (as intra-scene variance) while allowing for direct comparison between images from different times of year and with different synoptic setups. However, this abstracts the results and requires an additional step to extract actual LSTs or to extrapolate results to other contexts. We also note that this standardization is nevertheless subject to biases from multi-seasonal compositing (which tends to suppress variance) and from land cover change (e.g., drought). These factors are discussed in more depth in Section 4.4.

To aid the conversion of Z-score departures to LST departures, we calculated mean and standard deviation of LST for each image, displaying them in Figures 18 and 19. These can be used for rough conversion of Z-score Λ magnitudes to LST units. For example, an Λ of 0.9 in the afternoon in NYC represents a mean magnitude of anisotropy of approximately 3.0 K calculated between the two most divergent view geometries for high λ_c pixels. This value is averaged over all seasons and measured synoptic conditions (note: we only sample

clear sky conditions). Scene specific magnitudes of Λ (e.g., for a particularly warm scene) can also be inferred by calculating the scene standard deviation and multiplying it by the Z-score standardized Λ.

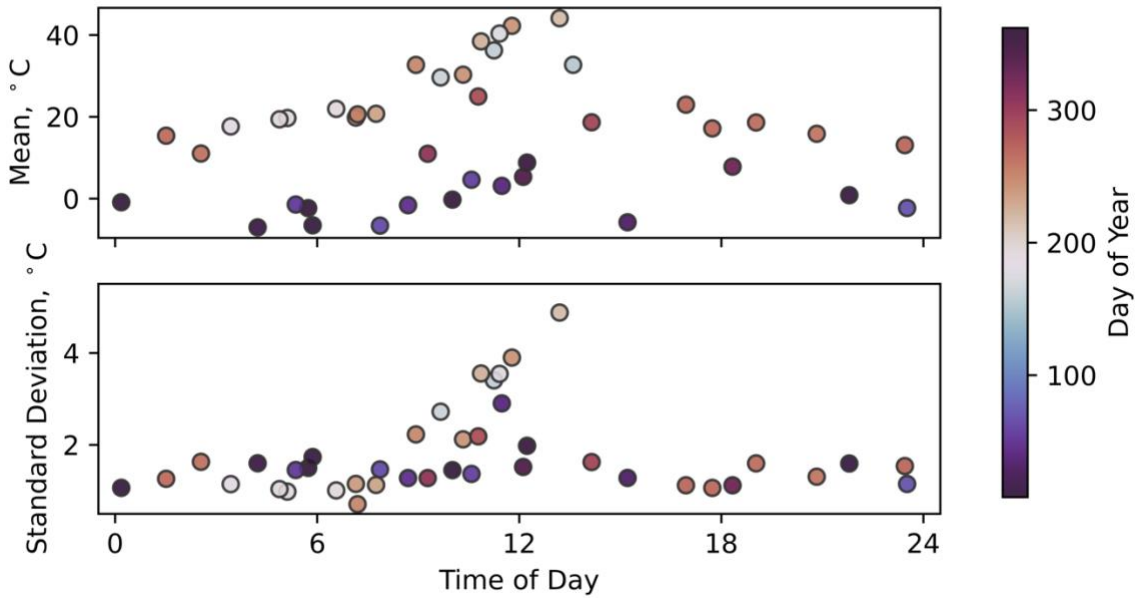

Figure 18. Mean and standard deviation of LST for the NYC study area. Each dot represents one scene.

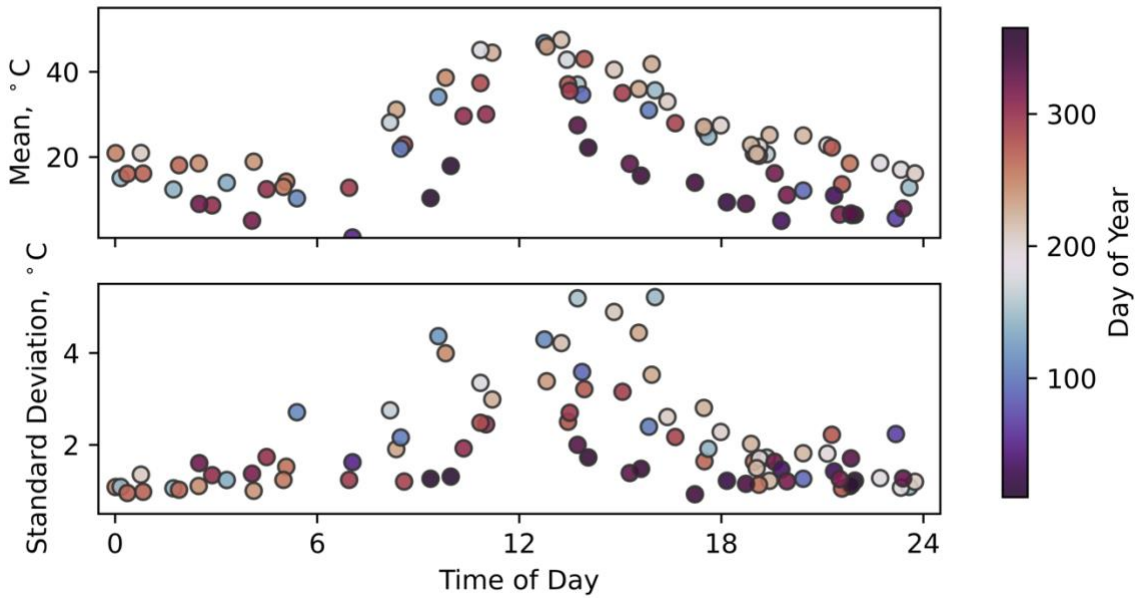

Figure 19. Mean and standard deviation of LST for the LA County study area. Each dot represents one scene.

4.2. Wall temperatures

The complete LST, i.e., a temperature representing an area weighted average of all facet-scale temperatures within a pixel or patch of the urban surface is of particular interest because it represents the temperature of the surface over the full interface between the surface and the atmosphere. While the plan-area LST is a useful substitute and generally has some level of internal validity, it has decreasing representivity with respect to the surface energy/water balance and human thermal comfort as surface structure (e.g., λ_c) increases. Several studies have attempted to infer complete (or more representative) LSTs from 2-dimensional radiometric thermal imagery using downscaling and model-assisted assessments (Voogt, 2008; Jiang *et al.*, 2018; Hu and Wendel, 2019). However, these studies generally rely on micro-scale models that estimate distributions of facet-scale temperatures over

simplified, often orthogonal grids. They are also exceedingly difficult to validate at city-scale as validation would require a full suite of measured directional LSTs over all sampled neighborhood types.

Thus, we posit that direct extraction of facet-scale LSTs from directional satellite imagery is a first step in developing a fully observational assessment of more representative, complete satellite urban LSTs. In this paper, we showed that when influence from confounding variables is mitigated (in this case, via multi-temporal sampling, diurnal binning, and Z-score standardization) we can observe distributions of facet-scale (e.g., wall, road, roof) LSTs from ECOSTRESS imagery by modeling the wall seen by the sensor given each pixel's unique surface-sensor geometry and extracting distributions of wall LSTs. As this method uses spatially extensive satellite imagery, we are able to extract facet-scale LSTs over an extent not possible via ground-based campaigns and with neighborhood-scale complexities not often represented in micro-scale models (e.g., influence from tree canopies, self-shading). However, we note some major challenges inherent with our approach.

At 70 m, most pixels are a mixture of multiple surface types. This is particularly apparent in densely built areas, where most pixels have fractional cover of at least 3 surface types. When combined with inaccuracies in coregistration, this meant that we were not confident in our ability to attribute pixel-scale LSTs to specific land cover types, particularly for our synthesized wall class, which exhibits strong contrasts at relatively fine scales (similar to shadow). Rather, we opted to extract distributions of wall LSTs for pixels with non-trivial fractions of seen wall in off-nadir view geometries. In spite of this, we observed measurable differences in LST between off-nadir views of wall-influenced impervious pixels and nadir views of roof and road pixels, particularly at night and in the afternoon.

Our results suggest that angular effects on the composition of sub-pixel fractional cover are minor at view zenith angles < 12 degrees. For pixels with view zenith angle > 12 degrees seen wall fraction increased linearly with increased surface height and roughness. While per-pixel wall fractions could be as high as ~0.95, we found that aggregating to neighborhood scale saw a reduction in mean wall fraction to a maximum of ~0.3. Seen wall fraction generally decreased with increasing tree cover (not shown) as wall displacement was often obscured by shadow from street trees. This was particularly apparent in low-rise residential neighborhoods with tight street grids (i.e., height to width ratio ~0.5-2) in LA County.

Effects on LST from sub-pixel wall fraction were clearly observed in LSTs, even at relatively small fractions (e.g., 10% wall fraction). Diurnal patterns were generally similar between the two study areas. This was in spite of strong contrasts between the two study areas in terms of dominant land cover and surface morphology, shading regimes, and regional scale climate forcings. Results at the city scale were similar to those observed by ground-based studies, with warmer wall LSTs at night from multiple emission and absorption of thermal radiation by surface structure (i.e., canyon radiation trapping) and cooler wall LSTs in the morning hours from minimal direct insolation and surface radiative cooling. Nighttime roof LSTs in NYC showed anomalously large variance, likely from exhaust from heating/cooling systems. We observed divergence in afternoon observations, with much warmer LSTs for west-facing walls and cooler LSTs for east-facing walls in NYC. In LA County, we observed much cooler LSTs for all wall influenced view directions compared to roof and road LSTs. We posit two factors that caused this discrepancy. First, tree heights in urbanized LA County are on average 4.8 m taller than building heights (Wetherley *et al.*,

2021), which obscures seen wall fractions (via canopy shading) and lowers overall LSTs for off-nadir views as increased LSTs from illuminated wall facets are offset by cooler LSTs from increasing tree canopy view fraction. Tree heights in NYC are generally lower than building heights (tree: 10.1 m +/- 7.8, building: 11.6 m +/- 15.4), particularly in the downtown core (restricted to Manhattan, tree: 11.6 m +/- 9.7, building: 29.3 m +/- 32.8), which reverses this effect. Second, the surface morphology in NYC promotes strong facet-scale contrasts in LST, as the surface is dominated by a regular grid of high-rise densely packed buildings with little vegetation cover. This increases angular contrasts in LST as wall displacement is rarely obscured by tree cover and is rarely subject to self-shading. In addition, we note that this discrepancy is generally consistent with results in (Hilland and Voogt, 2020), which showed strong neighborhood-scale contrasts in diurnal patterns of wall temperatures depending on surface morphology, self-shading, and tree cover. This comparison between two vastly different cities suggests that neighborhood-scale differences in facet-scale LSTs based on tree canopy cover observed by ground-based measurements may scale up to city-scale satellite observations (Dyce and Voogt, 2018).

4.3. Anisotropy

In this paper, we show that a combination of high spatial resolution LiDAR-derived surface morphology metrics with a time series of ECOSTRESS imagery can be used to measure neighborhood-scale patterns of effective anisotropy over the course of a day and stratified across driving variables (e.g., λ_c). The results presented in this study are consistent with model- and ground-based assessment of anisotropy both in terms of variance over the course of a day and with surface structure metrics (Lagouarde *et al.*, 2012; Krayenhoff and

Voogt, 2016), albeit with lower overall magnitudes of Λ. We found that anisotropy was largest in the afternoon in both cities, but was detectable for high λ_c neighborhoods at all times of day, particularly in NYC (Lagouarde *et al.*, 2010). We observed large spatial contrasts in directional LSTs in NYC, which has a surface structure and land cover which maximizes detection of angular contrasts in LST (i.e., highly impervious, densely built, high λ_c terrain).

Anisotropy followed the sun position closely but manifested slightly differently in the two study areas. In NYC, where neighborhoods are dominated by densely built high-rise buildings and little vegetation, off-nadir views of high λ_c neighborhoods showed warmer than average LSTs (i.e., a hot spot compared to nadir views of flat terrain). In contrast, in LA County, which has highly variable cover but is largely dominated by low-rise neighborhoods, we observed cooler than average LST for high λ_c neighborhoods (i.e., a persistent cool spot compared to nadir views of flat terrain). Thus, both cities had detectable anisotropy, the former observed as a warm departure for sensor azimuths in line with the sun position and the latter (in LA County) observed as a cool departure from the nadir view that was less severe for sensor azimuths in line with the sun position. We hypothesize that this discrepancy was driven by differences in directional wall LSTs, which in turn was forced by differential shading by tree canopy cover and by increased tree canopy in the sensor FOV in LA County, which offsets increases in LST for illuminated walls. In addition, the regular, largely orthogonal street grid in NYC (particularly in the downtown core) decreases shading of tall building facets, increasing the purity of illuminated wall facets in off-nadir views.

We also note that differences in latitude between the two study areas also influenced our estimates of anisotropy. NYC has a latitude of approximately 41 degrees. In contrast, LA

County has a latitude of approximately 34 degrees and weaker seasonal variability in solar azimuth angles. This means that summertime azimuth angles in NYC extent further north illuminating northeast-, north-, and northwest-facing walls more strongly for a longer period of the day compared to LA county. The opposite is true in winter, with solar azimuths restricted to the southern half of the sky in NYC. Combined with differences in surface morphology, tree canopy height/cover, and street grid orientation, we posit that the more extreme latitude of NYC produced stronger maximum contrasts in LST which resulted in larger overall magnitudes of anisotropy and more distinct diurnal patterns of directional wall LSTs.

In general, our estimates of anisotropy were lower than those observed from ground-based platforms (Voogt and Oke, 1998a), computational models (Hu and Wendel, 2019), and from time series remotely sensed imagery (Hu *et al.*, 2016). We attribute this underestimation to two factors. First, our analysis relied on binned averages between images taken from different seasons and synoptic setups, which tended to smooth spatial contrasts in LST resulting in lower maximum Λ values. In addition, we stratified over surface structural metrics by binning based on λ_c values. Both of these result in reduced overall variance in LST between different surface-sensor setups as we compared values that have been averaged twice. Second, the range of ECOSTRESS view zenith angles is not large enough to capture absolute maximums of Λ, which generally occur between extreme off nadir views (sensor zenith > 60 degrees) (Hu *et al.*, 2016; Krayenhoff and Voogt, 2016). This is compared to a maximum per-pixel zenith angle for ECOSTRESS of approximately 32 degrees.

4.4. Summarizing major limitations

This work is subject to three major limitations which restricted the scope of our analysis and contributed to uncertainty and error. First, this analysis relied on averaging and Z-score standardization to remove influence from synoptic and seasonal variability in LST. These, along with the diurnal cycle, often constitute the strongest signals in inter-image comparison, but were not variables of interest in this study. While standardization and compositing harmonized the central tendency of each image and reduced influence from synoptic/seasonal variance, it likely decreased ease of interpretation. Hu et al., (2016) used the water-land LST difference to account for non-geometric variance in an analysis of angular impacts on MODIS LST. This was advantageous because it allowed the authors to directly compute angular effects on urban LST in temperature units (rather than statistical differences). However, the land-water differential is likely only appropriate over a long and consistent time series, such as those available from the MODIS sensors. In this study, we found that a similar approach easily removed seasonal effects on LST but was insufficient to remove synoptic impacts because the thermal mass of water makes it slow to respond to synoptic variance.

Moreover, we note that it is likely that the only solution that thoroughly removes variance from unwanted parameters is consistent multi-seasonal sampling and/or exceedingly large amounts of quality-controlled data, which would allow for the option to exclude specific seasons or synoptic setups without sacrificing geometric or diurnal sampling. Based on difference in efficacy between LA County and NYC (which had about half the number of samples, mostly due to greater cloud contamination), we posit that approximately 150 quality controlled ECOSTRESS images is adequate to balance diurnal sampling with removing

synoptic/seasonal effects. This corresponds to ~900-1300 raw ECOSTRESS scenes or 4-7 years of consistent data. Less images are necessary in cloud-free areas or in areas with less seasonal or synoptic variance. Increased image quality (i.e., artifact removal, coregistration fixes) would drastically lower raw scene count requirements.

Second, we assume consistent land cover over the time series of LST and assume leaf-on conditions year-round for all vegetation. Thus, the inter-scene contrasts we observe were likely contaminated by land cover change, either from land conversion, expansion or modification of the built environment, or by phenology or seasonal variability in vegetation cover. Vegetation cover and particularly tree cover was low for most of the NYC study area and was generally restricted to expanses of green space greater that 70 m. As we filtered pixels based on thresholds of impervious cover, land cover change and phenology in these areas likely had little influence on LST contrasts. In LA County vegetation cover is much more dispersed and inter-/intra-seasonal variability in green vegetation cover can be large (Wetherley *et al.*, 2018; Allen *et al.*, 2021). Thus, we posit that even with our impervious cover threshold, our results were subject to some influence from seasonal vegetation cover change. However, approximately 78% of tree cover in the LA County study area is evergreen (Nowak *et al.*, 2011), which does not show large variance in tree canopy status over a year. Moreover, precipitation in LA County over the study period was in line with climate normals, with mild to moderate drought conditions observed in the summer of 2018, which likely promoted stable vegetation cover similar to that described in the 2014/15 LARIAC datasets.

As a final and potentially most consequential limitation we were often unable to tie the ECOSTRESS imagery to a consistent grid. This resulted in the rejection of some

otherwise sound images based on coregistration errors that could not be resolved using the spatial nudging routine. Moreover, we found persistent small pixel shifts (1-2 pixels) in many images. These shifts had a strong effect on our analysis of wall LSTs as we were only able to extract distributions of wall influenced impervious LSTs rather than pure wall LSTs. It also hampered our ability to attribute angular effects to seen wall fraction (i.e., per-pixel analysis) as wall fractions vary at very small scales (similar to shadowing) and we were not confident in the per-pixel geolocation accuracy of each of our images. While we do not believe that coregistration errors had a significant effect on our final analyses, it nevertheless impacted the types of analyses that we were able to perform.

5. Conclusions

In this paper, we used a combination of high spatial resolution land cover and surface structure datasets derived from LiDAR and aerial orthophotos to calculate sub-pixel wall fractions seen for a time series of ECOSTRESS imagery for a wide range of sun-surface-sensor geometries. We then used the time series of LST imagery, surface-sensor modeling, and cover/height datasets to (1) investigate seen wall fractions as a function of zenith angle and surface structure, (2) compare distributions of fractional wall LSTs to LSTs of other facets, and to (3) estimate and (4) map magnitudes of urban effective anisotropy. Our analyses showed complex relationships between surface structure, sun-surface sensor geometry, land cover and remotely measured urban LSTs. What follows is a summary of our main conclusions,

- Seen wall fraction increased linearly with sensor zenith angle and with surface structure (mean building height, λ_c). Seen wall fraction was as large as 0.95 for $\lambda_c > 50$ and sensor

zenith > 25, but at the neighborhood scale generally did not increase >0.3. We found that it was important to model using per-pixel surface-sensor geometry rather than scene averaged values as sensor zenith/azimuth can vary significantly at the scale of a city.

- Angular effects on LST and seen wall fractions were minimized for sensor zenith angles < 12 degrees for pixels with λ_c < ~50. In most cases, these can be considered equivalent to nadir imagery, particularly for low- to medium-rise neighborhoods.
- A combination of nadir and off-nadir views with fine land cover, surface structure, and surface-sensor modeling can be used to extract distributions of facet-scale LSTs. NYC and LA County showed similar patterns of facet-scale LSTs in the morning hours and at night, with differences observed in wall LSTs in the afternoon.
- Diurnal patterns of directional LSTs followed patterns observed for extracted wall LSTs. Contrasts in LSTs across off-nadir view directions increased with surface complexity (i.e., λ_c), particularly in the morning and afternoon hours as did contrasts between nadir views and off-nadir views. This supports increasing divergence between plan-area and complete LSTs as pixel zenith angle and λ_c increased, particularly in afternoon imagery.
- We observed a divergence between the two cities in patterns of directional LSTs and effective anisotropy in afternoon observations. West facing walls showed much warmer LSTs in NYC, which forced a relative hot spot in directional LSTs for west off-nadir views and strong positive anisotropy in the afternoon. In contrast, in LA County we observed cooler off-nadir LSTs in all directional off-nadir views, with anisotropy observed as slightly warmer (but still cooler than average) off-nadir LSTs for northwest sensor positions.
- Results were limited by incomplete seasonal/diurnal sampling, which restricted our ability to stratify across sun-surface-sensor geometries and over a diurnal cycle. This problem was most evident in NYC, where seasonal contrasts in LST are large. Inconsistent coregistration also presented a major challenge to pixel-scale analysis and while coregistration was

improved by implementing a spatial nudging routine, we were often unable to tie the imagery to a consistent spatial grid.

Overall, these results indicate measurable and consistent directional effects on ECOSTRESS LSTs that are attributable to neighborhood-scale parameters such as land cover and surface morphology. These directional impacts can be construed as a bias (i.e., effective anisotropy) or as an additional source of signal (i.e., extracted wall LST distributions). In this paper, we investigated and quantified both perspectives using two 2.5 year time series of thermal imagery. We present a framework for estimating (and potentially correcting) per-pixel angular effects on remotely sensed imagery and for extracting otherwise unavailable LSTs of vertical facets from imagery at city-scale. As the volume of remotely sensed thermal imagery increases and as planners and policymakers increasingly utilize these data to measure and project climate impacts on urban populations, it becomes increasingly important to bridge the gaps and quantify biases between fine-scale in-situ, modeled, and coarse-scale remotely sensed analyses. Sensors with unique orbital characteristics (such as ECOSTRESS) are well positioned to offer such capabilities.

Conclusions

This dissertation had two main goals. First, to quantify the sensitivity of urban vegetation cover, urban heat, and plant-temperature relationships to drought. Second, to exploit the unique orbital/sensor parameters of the new ECOSTRESS dataset to facilitate novel satellite-based assessment of fine-scale diurnal patterns of urban land surface temperature (LST) and to develop subpixel estimates of facet-scale LSTs (e.g., walls, roofs, roads, etc.) and thermal anisotropy over the course of a day and as a function of per-pixel surface-sensor relationships and surface morphology. In this final chapter, I begin by summarizing the main findings of Chapters 1-3 with respect to the science goals outlined above and finish with some concluding thoughts.

In Chapter 1, I found complex coupling between drought-intensity, GV cover, and tree/grass cooling capacity. Mean GV cover decreased by 4.7% over the 2012-16 California drought, with stronger reductions in GV cover observed for grass compared to tree. Drought-forced losses in GV cover were strongest in drier inland regions compared to coastal regions, with a net increase in GV cover pre- to post-drought near the coast and sustained losses of GV cover in inland regions. Cooling from GV cover decreased similarly, likely via a combination of reductions in overall GV cover and reduced evapotranspiration causing a shift in energy balance partitioning from latent heat to sensible heat. Reductions in cooling occurred faster and were stronger for grass compared to tree, but post-drought increases in cooling were stronger for grass, with relatively low cooling observed for tree a year after the end of the drought.

Within the drought itself, I observed strong spikes in GV cover following precipitation events. These spikes in GV cover were largely observed in expanses of

unmaintained low vegetation (e.g., grasses) rather than neighborhood vegetation (e.g., lawns, sparse trees), which translated into weak impacts on urban heat. Strong month-to-month variability in GV cover during the drought suggests that care should be taken to select image dates that are representative of the climate context, for example to ensure that drought sampling periods do not follow (even small) precipitation events.

In Chapter 2, I developed a fine spatial resolution diurnal time series of urban LST imagery using composited ECOSTRESS imagery. This represents the first fully observational 24-hour diurnal assessment of urban heat from fine-scale satellite imagery. The composited diurnal time series was able to replicate fine-scale and higher order features observed in ground-based thermography (e.g., tower-mounted cameras, vehicle traverses) including accurately depicting the timing of minimum and maximum temperatures for different land cover types and capturing asymmetry in morning heating and afternoon cooling rates. I found strong variability in the relative importance of topographic, morphological, and environmental drivers of LST over the course of the day. Notably, cooling from urban vegetation – which is often posed as an effective tool for heat mitigation – showed strong seasonal and diurnal variability in strength and a maximum cooling capacity of ~7 °C just after solar noon based on Spring-Summer composited means. Moreover, the results in this study show that cooling from vegetation was not detected for tree/grass fractions <25%, suggesting a minimum cover threshold for measurable microclimatic impacts.

I found that a two-hour bin size was optimal for a two-year data set of ECOSTRESS imagery over study areas (in this case, urbanized Los Angeles County) that were relatively seasonally isothermal. For continental climates, which have stronger seasonal contrasts in

temperature, the bin sizes will likely need to be wider and stratified by season. Strong correlation between concurrent ECOSTRESS and MODIS LSTs and similar diurnal curves to those observed from ground-based campaigns suggest that these compositing methods are likely generalizable to other cities and non-urban domains.

In Chapter 3, I used an expanded composited time series of ECOSTRESS imagery to investigate the diurnal course of thermal anisotropy of urban LSTs and to extract subpixel LSTs for systematically undersampled vertical and sloped facets of the urban surface. To do this, I developed a rasterized sun-surface-sensor parameterization to project the field-of-view (FOV) of the ECOSTRESS sensor onto a filtered DSM to estimate subpixel "seen" wall fractions and occluded surface proportions. These "tagged" subpixel areas were then aggregated to fractions at 70m and harmonized with existing fractional land cover datasets. I found that significant (>20-30% averaged across the New York City, NY, USA study area) proportions of the ECOSTRESS FOV were occupied by vertical facets such as walls, and that this proportion varied significantly with surface structure and view zenith angle. By estimating per-pixel wall FOV proportions, I was able to extract fractional wall LSTs that were distinct from other horizontal facets (and indeed, were district when viewed different sun-surface-sensor setups) and followed a similar diurnal pattern at city-scale compared to ground-based observations in the literature (Voogt and Oke, 1998b). By binning images based on time of day and, I observed strong thermal anisotropy (> 1 std of LST) in both New York and urbanized Los Angeles county, which followed slightly different diurnal courses. Finally, by stratifying by sub-pixel surface structure, I was also able to define functional relationships between surface morphology and average magnitudes of anisotropy for

morning, afternoon, and night observation times. Results were consistent with model- and ground-based studies of urban anisotropy (albeit slightly lower).

Taken together, these results raise two main synthesizing points for policymakers and for shaping future science missions. First, policymakers at many scales (e.g., municipal, state, national, international) are explicitly recognizing that impacts from climate change on human health, water/energy use, and livability are near-term problems that require near-term solutions (Cutter *et al.*, 2014; Broadbent *et al.*, 2020). In response, many cities include vegetation and tree planting as a large part of their climate action plans to mitigate extremes of temperature and to reduce disparities in access to green space (Norton *et al.*, 2015). This dissertation shows the importance of climate informed decision making, particularly with respect to urban vegetation planting, as the needs of water conservation (e.g., restricted outdoor irrigation during drought) will likely be at odds with increased water demand in newly planted areas in many arid cities. Moreover, I show that small (i.e., <25%) fractions of vegetation cover are likely ineffective as a heat mitigation tool. These points highlight the complexity of the nexus of climate change, heat mitigation, and water/energy use in cities. Effective policy decisions around urban greening must be data driven and account for heat mitigation needs, water conservation measures, historical disparities, and climate context when selecting sites, plant types, and maintenance regimes.

In addition, this research suggests that sub-monthly monitoring of urban vegetation cover is possible (particularly with satellite clusters, such as commercialized multi/hyperspectral VSWIR imagery) and would likely be an effective way to optimize both planting measures for reducing urban heat and for identifying areas of significant vegetation stress during low precipitation periods. Thermal imagery may be an additional tool for

accomplishing both goals as it can be used to measure both the spatial distribution of heat and for identifying water stressed vegetation patches.

Second, this research provides an important bridge between the growing catalogue of large-scale empirical studies of urban microclimates and ground-up process-based (often in-situ or model-based) micro-scale analyses of the same phenomena. My analysis shows that fine-scale time series thermal imagery – particularly from platforms with unique orbital characteristics – is highly effective for observing micro- and facet-scale functional relationships in urban microclimates and for bridging gaps in scale, methods, and understanding. However, the findings in Chapters 2 and 3 highlight the fact that many questions vis a vis the applicability of thermal remote sensing to study of urban phenomena remain unanswered (Roth *et al.*, 1989; Voogt and Oke, 2003). For example, the representivity and completeness of LST imagery varies within and between cities based on surface structure/materials and with sensor zenith and azimuth angle (which in turn, vary within and between images). These factors are generally only mentioned (rather than analyzed or corrected) in urban thermal remote sensing and have not been integrated into analysis-ready thermal products. While analogous directional impacts on VSWIR imagery have received significant attention (e.g., the Bidirectional Reflectance Distribution Function), these results reinforce the understanding that thermal remote sensing relies on the same laws of physics and is subject to the same effects (e.g., anisotropy) as those affecting VSWIR remote sensing. The analysis in Chapter 3 shows that fusing fine-scale thermal imagery with surface morphology data may be a first step to providing per-pixel documentation of the type of LST in each pixel (e.g., complete, plan-area, angular), sub-pixel proportions of different facets, and the range/magnitude of potential angular effects. This information could

potentially be delivered in a similar fashion to quality and cloud flags in image metadata and quality control rasters.

Overall, this dissertation highlights the importance of process-based understanding and analysis in urban remote sensing. Indeed, urban areas have a different structure, surface materials, climate-forcings, and anthropogenic effects compared to adjacent natural environments. This study (and many before it) show that these signals are detectable via remote sensing at multiple spatial and temporal scales and that accurate detection of different environmental, morphological, and anthropogenic signals on phenomena of interest forms the basis for comprehensive analysis of urban vegetation and urban microclimates. As the quality, granularity, and quality of thermal and VSWIR remotely sensed imagery increases so does its explanatory power for informing a process-based understanding of the urban environment. These data, when combined with ground-based sensor networks and ever-increasing computational power, are well positioned to provide key datasets and insights to aid in urban planning and in decision making to promote climate resilience and microclimatic equity in cities.

Appendix 1: Supplemental materials for Chapter 2

Figure S1 shows fractional land cover maps, distance to coast, elevation, and height above ground maps for the study area. These are described in the "Ancillary Data" section of Methods.

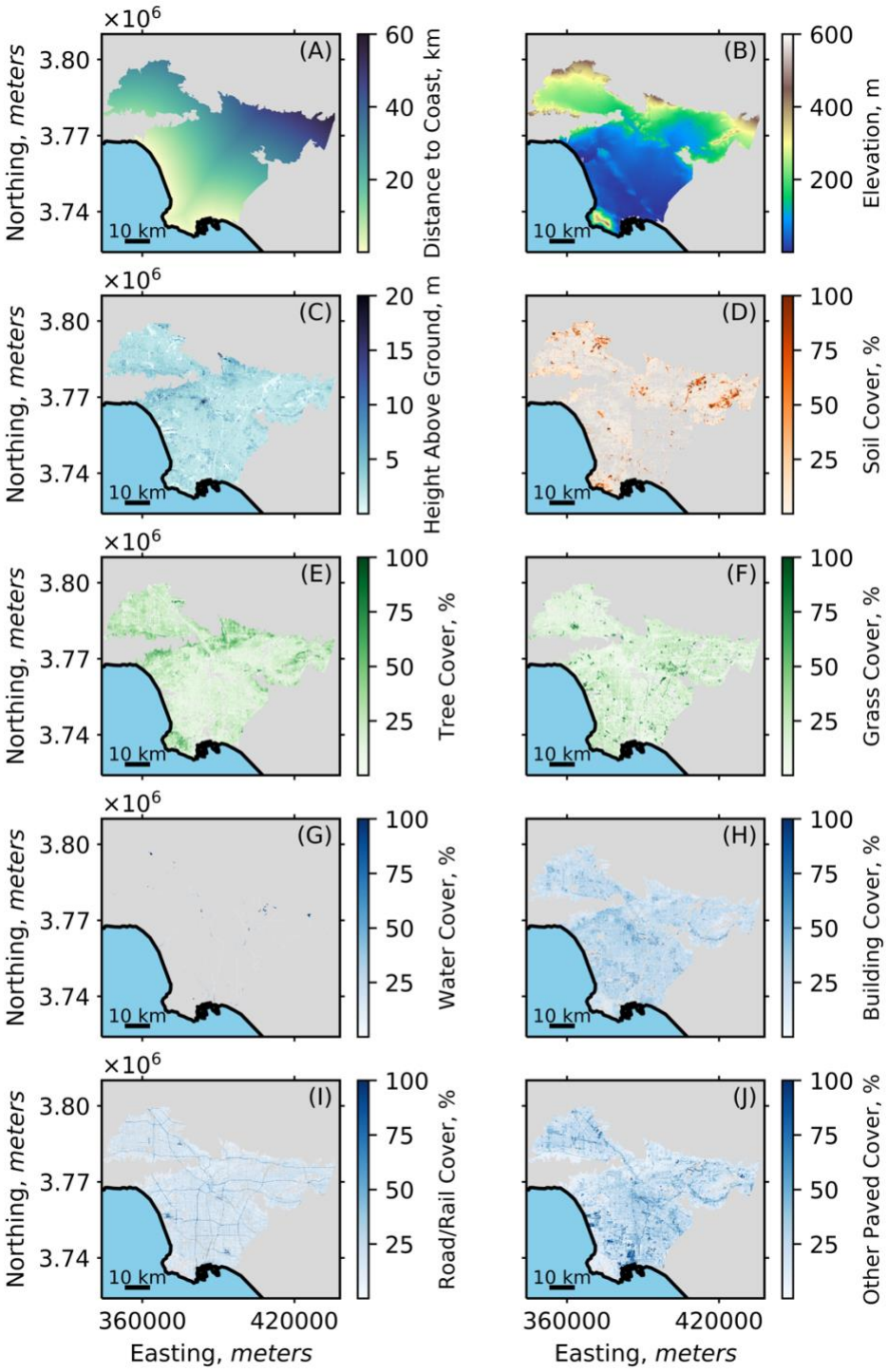

Figure S1: Maps of distance to coast, elevation, height above ground, and fractional land cover for each land cover class at 70 m for the Los Angeles County urbanized study area.

Appendix 2: Supplemental materials for Chapter 3

Sampling and extracting wall facet temperatures requires multi-directional imagery (nadir, west-facing off nadir, east-facing off nadir) and stratification for a given image for land cover and seen wall fraction. Table S1 shows counts of images for each direction and sampling period for both NYC and LA County. Nadir includes all images with mean view zenith < 12 degrees. The two off nadir views (east and west) include all images with mean view zenith > 12 degrees with sensor azimuth > 180 degrees for west and < 180 degrees for east. Morning includes all images from sunrise to noon, afternoon all images from noon to sunset, and night all images between 2 hours after sunset and sunrise.

Table S1. Counts of images for the three different binned sensor orientations and sampling times for NYC and LA County.

Direction	New York City	Los Angeles County
Nadir		
Morning	13	8
Afternoon	4	15
Night	7	21
Sensor East		
Morning	3	6
Afternoon	2	7
Night	3	9
Sensor West		
Morning	4	4
Afternoon	2	9
Night	4	9

Table S2 and S3 show pixel counts for sensitivity testing of wall fraction thresholds for Section 3.2. While we did not observe significant differences in results when varying wall fraction thresholds, we did observe linear reductions in pixel counts with increasing wall fraction. For example, separation between fractional wall LSTs and road/roof LSTs over a range of wall fraction thresholds (i.e., 0.15 to 0.3) was approximately the same, with generally wider distributions of wall LSTs at lower wall fraction thresholds. We ultimately chose a threshold of 0.2 to ensure consistent sampling in LA County with large enough wall fractional effect to observe the distinct course of west- and east-facing walls in both study areas.

Table S2. Counts of pixels for different wall fraction thresholds (0.15, 0.2, 0.3) for off nadir sensor orientations in NYC. These fractional thresholds represent the proportion of seen wall for pixels with > 75% impervious cover. Nadir Road and Roof counts are also included for reference.

Surface Type	Wall > 0.15	Wall > 0.20	Wall > 0.30
Sensor East	4157	2223	1238
Sensor West	2559	1046	458
Roof	5042	5216	5293
Road	36389	36451	34978

Table S3. Counts of pixels for different wall fraction thresholds (0.15, 0.2, 0.3) for off nadir sensor orientations in LA County. These fractional thresholds represent the proportion of seen wall for pixels with > 75% impervious cover. Nadir Road and Roof counts are also included for reference.

Surface Type	Wall > 0.15	Wall > 0.20	Wall > 0.30
Sensor East	131	59	26
Sensor West	102	34	10
Roof	21749	21763	21769
Road	158176	158182	158187

References

Adderley, C., Christen, A. and Voogt, J. A. (2015) 'The effect of radiometer placement and view on inferred directional and hemispheric radiometric temperatures of an urban canopy', *Atmospheric Measurement Techniques*, 8(2), pp. 1891–1933. doi: 10.5194/amtd-8-1891-2015.

AghaKouchak, A. *et al.* (2014) 'Global warming and changes in risk of concurrent climate extremes: Insights from the 2014 California drought', *Geophysical Research Letters*, 41(24), pp. 8847–8852. doi: 10.1002/2014GL062308.

Allen, M. A. (2017) *A Method for Hemispherical Ground Based Remote Sensing of Urban Surface Temperatures*. University of Western Ontario.

Allen, M. A., Roberts, D. A. and McFadden, J. P. (2021) 'Reduced urban green cover and daytime cooling capacity during the 2012–2016 California drought', *Urban Climate*, 36(March 2021), p. 100768. doi: 10.1016/j.uclim.2020.100768.

Aniello, C. *et al.* (1995) 'Mapping micro-urban heat islands using LANDSAT TM and a GIS', *Computers and Geosciences*, 21(8).

Arnold, C. L. and Gibbons, C. J. (1996) 'Impervious surface coverage : The emergence of a key environmental indicator', *Journal of the American Planning Association*, 62(2), pp. 243–258.

Asner, G. P. *et al.* (2016) 'Progressive forest canopy water loss during the 2012-2015 California drought', *Proceedings of the National Academy of Sciences of the United States of America*, 113(2), pp. E249–E255. doi: 10.1073/pnas.1523397113.

Avolio, M. *et al.* (2019) 'Urban plant diversity in Los Angeles, California: Species and functional type turnover in cultivated landscapes', *Plants, People, Planet*, 2(2), pp. 144–156. doi: 10.1002/ppp3.10067.

Bechtel, B. *et al.* (2019) 'SUHI analysis using Local Climate Zones - a comparison of 50 cities', *Urban Climate*, 28(June), p. NA. doi: 10.1016/j.uclim.2019.01.005.

Berg, N. and Hall, A. (2017) 'Anthropogenic warming impacts on California snowpack during drought', *Geophysical Research Letters*, 44(5), pp. 2511–2518. doi: 10.1002/2016GL072104.

Bergeron, O. and Strachan, I. B. (2012) 'Wintertime radiation and energy budget along an urbanization gradient in Montreal, Canada', *International Journal of Climatology*, 32(1), pp. 137–152. doi: 10.1002/joc.2246.

Berland, A. *et al.* (2017) 'The role of trees in urban stormwater management', *Landscape and Urban Planning*, 162, pp. 167–177. doi: 10.1016/j.landurbplan.2017.02.017.

Best, M. J. and Grimmond, C. S. B. (2016) 'Modeling the Partitioning of Turbulent Fluxes at Urban Sites with Varying Vegetation Cover', *Journal of Hydrometeorology*, 17(10), pp. 2537–2553. doi: 10.1175/JHM-D-15-0126.1.

Bijoor, N. S. *et al.* (2012) 'Water sources of urban trees in the Los Angeles metropolitan area', *Urban Ecosystems*, 15(1), pp. 195–214. doi: 10.1007/s11252-011-0196-1.

Bolund, P. and Hunhammar, S. (1999) 'Ecosystem services in urban areas', *Ecological Economics*, 29(2), pp. 293–301. doi: 10.1016/S0921-8009(99)00013-0.

Broadbent, A. M., Krayenhoff, E. S. and Georgescu, M. (2020) 'The motley drivers of heat and cold exposure in 21st century US cities', *Proceedings of the National Academy of Sciences of the United States of America*, 117(35), pp. 21108–21117. doi: 10.1073/pnas.2005492117.

Cao, B. *et al.* (2019) 'A review of earth surface thermal radiation directionality observing and modeling: Historical development, current status and perspectives', *Remote Sensing of Environment*, 232(May), p. 111304. doi: 10.1016/j.rse.2019.111304.

Cawse-Nicholson, K. *et al.* (2021) 'NASA's surface biology and geology designated observable: A perspective on surface imaging algorithms', *Remote Sensing of Environment*, 257. doi: 10.1016/j.rse.2021.112349.

Chen, Y. J. *et al.* (2015) 'Measuring Spatio-temporal Trends in Residential Landscape Irrigation Extent and Rate in Los Angeles, California Using SPOT-5 Satellite Imagery', *Water Resources Management*, 29(15), pp. 5749–5763. doi: 10.1007/s11269-015-1144-2.

Christen, A., Meier, F. and Scherer, D. (2012) 'High-frequency fluctuations of surface temperatures in an urban environment', *Theoretical and Applied Climatology*, 108(1–2), pp. 301–324. doi: 10.1007/s00704-011-0521-x.

Clarke, L. W., Jenerette, G. D. and Davila, A. (2013) 'The luxury of vegetation and the legacy of tree biodiversity in Los Angeles, CA', *Landscape and Urban Planning*, 116, pp. 48–59. doi: 10.1016/j.landurbplan.2013.04.006.

Clinton, N. and Gong, P. (2013) 'MODIS detected surface urban heat islands and sinks: Global locations and controls', *Remote Sensing of Environment*, 134, pp. 294–304. doi: 10.1016/j.rse.2013.03.008.

Crum, S. M. and Jenerette, G. D. (2017) 'Microclimate variation among urban land covers: The importance of vertical and horizontal structure in air and land surface temperature relationships', *Journal of Applied Meteorology and Climatology*, 56(9), pp. 2531–2543. doi: 10.1175/JAMC-D-17-0054.1.

Cutter, S. L. *et al.* (2014) 'Ch. 11: Urban Systems, Infrastructure, and Vulnerability. Climate Change Impacts in the United States', *The Third National Climate Assessment*, pp. 282–296. doi: 10.7930/J0F769GR.On.

Demuzere, M. *et al.* (2020) 'Combining expert and crowd-sourced training data to map urban form and functions for the continental US', *Scientific Data*, 7(1), pp. 1–13. doi: 10.1038/s41597-020-00605-z.

Dennison, P. E. and Roberts, D. A. (2003) 'Endmember selection for multiple endmember spectral mixture analysis using endmember average RMSE', *Remote Sensing of Environment*, 87(2–3), pp. 123–135. doi: 10.1016/S0034-4257(03)00135-4.

Diffenbaugh, N. S., Swain, D. L. and Touma, D. (2015) 'Anthropogenic warming has increased drought risk in California', *Proceedings of the National Academy of Sciences*, 112(13), pp. 3931–3936. doi: 10.1073/pnas.1422385112.

Dong, C. *et al.* (2019) 'Vegetation Responses to 2012–2016 Drought in Northern and Southern California', *Geophysical Research Letters*, 46(7), pp. 3810–3821. doi: 10.1029/2019GL082137.

Duncan, J. M. A. *et al.* (2019) 'Turning down the heat: An enhanced understanding of the relationship between urban vegetation and surface temperature at the city scale', *Science of the Total Environment*, 656, pp. 118–128. doi: 10.1016/j.scitotenv.2018.11.223.

Dyce, D. R. and Voogt, J. A. (2018) 'The influence of tree crowns on urban thermal effective anisotropy', *Urban Climate*, 23, pp. 91–113. doi: 10.1016/j.uclim.2017.02.006.

Fisher, J. B. *et al.* (2020) 'ECOSTRESS: NASA's Next Generation Mission to Measure Evapotranspiration From the International Space Station', *Water Resources Research*, 56(4), pp. 1–20. doi: 10.1029/2019wr026058.

Fraser, A. M. *et al.* (2017) 'Household accessibility to heat refuges: Residential air conditioning, public cooled space, and walkability', *Environment and Planning B: Urban Analytics and City Science*, 44(6), pp. 1036–1055. doi: 10.1177/0265813516657342.

Georgescu, M. *et al.* (2011) 'An alternative explanation of the semiarid urban area "oasis effect"', *Journal of Geophysical Research Atmospheres*, 116(24). doi: 10.1029/2011JD016720.

Gillespie, A. *et al.* (1998) 'A temperature and emissivity separation algorithm for advanced spaceborne thermal emission and reflection radiometer (ASTER) images', *IEEE Transactions on Geoscience and Remote Sensing*, 36(4), pp. 1113–1126. doi: 10.1109/36.700995.

Gonzales, P. and Ajami, N. (2017) 'Social and Structural Patterns of Drought-Related Water Conservation and Rebound', *Water Resources Research*, 53(12), pp. 10619–10634. doi: 10.1002/2017WR021852.

Griffin, D. and Anchukaitis, K. J. (2014) 'How unusual is the 2012 – 2014 California drought?', *Geophysical Research Letters*, 41, pp. 9017–9023. doi: 10.1002/2014GL062433.1.

Grimmond, S. B., Souch, C. and Hubble, M. (1996) 'Influence of tree cover on summertime surface energy balance fluxes, San Gabriel Valley, Los Angeles', *Climate Research*, 6(1), pp. 45–57. doi: 10.1007/BF00242527.

Gu, Y. *et al.* (2013) 'NDVI saturation adjustment: A new approach for improving cropland performance estimates in the Greater Platte River Basin, USA', *Ecological Indicators*, 30, pp. 1–6. doi: 10.1016/j.ecolind.2013.01.041.

Hilland, R. V. J. and Voogt, J. A. (2020) 'The effect of sub-facet scale surface structure on wall brightness temperatures at multiple scales', *Theoretical and Applied Climatology*, 140(1–2), pp. 767–785. doi: 10.1007/s00704-020-03094-7.

Hook, S. J. *et al.* (2020) 'In-Flight Validation of the ECOSTRESS, Landsats 7 and 8 Thermal Infrared Spectral Channels Using the Lake Tahoe CA/NV and Salton Sea CA Automated Validation Sites', *IEEE Transactions on Geoscience and Remote Sensing*, 58(2), pp. 1294–1302. doi: 10.1109/TGRS.2019.2945701.

Hrisko, J. *et al.* (2020) 'Urban air temperature model using GOES-16 LST and a diurnal regressive neural network algorithm', *Remote Sensing of Environment*, 237(February), p. 111495. doi: 10.1016/j.rse.2019.111495.

Hu, L. *et al.* (2016) 'A first satellite-based observational assessment of urban thermal anisotropy', *Remote Sensing of Environment*, 181, pp. 111–121. doi: 10.1016/j.rse.2016.03.043.

Hu, L. and Brunsell, N. A. (2013) 'The impact of temporal aggregation of land surface temperature data for surface urban heat island (SUHI) monitoring', *Remote Sensing of Environment*, 134, pp. 162–174. doi: 10.1016/j.rse.2013.02.022.

Hu, L. and Wendel, J. (2019) 'Analysis of urban surface morphologic effects on diurnal thermal directional anisotropy', *ISPRS Journal of Photogrammetry and Remote Sensing*, 148(September 2018), pp. 1–12. doi: 10.1016/j.isprsjprs.2018.12.004.

Huang, F. *et al.* (2016) 'Temporal upscaling of surface urban heat island by incorporating an annual temperature cycle model: A tale of two cities', *Remote Sensing of Environment*, 186, pp. 1–12. doi: 10.1016/j.rse.2016.08.009.

Hulley, G. *et al.* (2019) 'New ECOSTRESS and MODIS land surface temperature data reveal fine-scale heat vulnerability in cities: A case study for Los Angeles County, California', *Remote Sensing*, 11(18), pp. 6–8. doi: 10.3390/rs11182136.

Hulley, G. C., Dousset, B. and Kahn, B. H. (2020) 'Rising Trends in Heatwave Metrics Across Southern California', *Earth's Future*, 8(7), pp. 1–21. doi: 10.1029/2020EF001480.

Hulley, G. C., Hughes, C. G. and Hook, S. J. (2012) 'Quantifying uncertainties in land surface temperature and emissivity retrievals from ASTER and MODIS thermal infrared data', *Journal of Geophysical Research Atmospheres*, 117(23), pp. 1–18. doi: 10.1029/2012JD018506.

Hutyra, L. R. *et al.* (2014) 'Urbanization and the carbon cycle: Current capabilities and research outlook from the natural sciences perspective', *Earth's Future*, 2(10), pp. 473–495. doi: 10.1002/2014ef000255.

Jiang, L. *et al.* (2018) 'Remote estimation of complete urban surface temperature using only directional radiometric temperatures', *Building and Environment*, 135(December 2017), pp. 224–236. doi: 10.1016/j.buildenv.2018.03.005.

Krayenhoff, E. S. and Voogt, J. A. (2016) 'Daytime thermal anisotropy of urban neighbourhoods: Morphological causation', *Remote Sensing*, 8(2), pp. 1–22. doi: 10.3390/rs8020108.

Lagouarde, J. P. *et al.* (2004) 'Airborne experimental measurements of the angular variations in surface temperature over urban areas: Case study of Marseille (France)', *Remote Sensing of Environment*, 93(4), pp. 443–462. doi: 10.1016/j.rse.2003.12.011.

Lagouarde, J. P. *et al.* (2010) 'Modelling daytime thermal infrared directional anisotropy over Toulouse city centre', *Remote Sensing of Environment*, 114(1), pp. 87–105. doi: 10.1016/j.rse.2009.08.012.

Lagouarde, J. P. *et al.* (2012) 'Experimental characterization and modelling of the nighttime directional anisotropy of thermal infrared measurements over an urban area: Case study of Toulouse (France)', *Remote Sensing of Environment*, 117, pp. 19–33. doi: 10.1016/j.rse.2011.06.022.

Lee, C. M. *et al.* (2015) 'An introduction to the NASA Hyperspectral InfraRed Imager (HyspIRI) mission and preparatory activities', *Remote Sensing of Environment*, 167, pp. 6–19. doi: 10.1016/j.rse.2015.06.012.

Leuzinger, S., Vogt, R. and Körner, C. (2010) 'Tree surface temperature in an urban environment', *Agricultural and Forest Meteorology*, 150(1), pp. 56–62. doi: 10.1016/j.agrformet.2009.08.006.

Li, H., Harvey, J. and Kendall, A. (2013) 'Field measurement of albedo for different land cover materials and effects on thermal performance', *Building and Environment*, 59, pp. 536–546. doi: 10.1016/j.buildenv.2012.10.014.

Lindberg, F., Holmer, B. and Thorsson, S. (2008) 'SOLWEIG 1.0 - Modelling spatial variations of 3D radiant fluxes and mean radiant temperature in complex urban settings', *International Journal of Biometeorology*, 52(7), pp. 697–713. doi: 10.1007/s00484-008-0162-7.

Litvak, E. *et al.* (2017) 'Evapotranspiration of urban landscapes in Los Angeles, California at the municipal scale', *Water Resources Research*, pp. 4236–4252. doi: 10.1002/2013WR014979.Reply.

Di Lorenzo, E. and Mantua, N. (2016) 'Multi-year persistence of the 2014/15 North Pacific marine heatwave', *Nature Climate Change*, 6(11), pp. 1042–1047. doi:

10.1038/nclimate3082.

Los Angeles Region Imagery Acquisition Consortium (2015) *LARIAC 4 Deliverables*. Los Angeles, CA. Available at: https://egis3.lacounty.gov/dataportal/lariac/.

McPherson, E. G. *et al.* (2017) 'The structure, function and value of urban forests in California communities', *Urban Forestry and Urban Greening*, 28(July), pp. 43–53. doi: 10.1016/j.ufug.2017.09.013.

McPherson, E. G., Berry, A. M. and van Doorn, N. S. (2018) 'Performance testing to identify climate-ready trees', *Urban Forestry and Urban Greening*, 29(March 2017), pp. 28–39. doi: 10.1016/j.ufug.2017.09.003.

Meier, F. *et al.* (2011) 'Atmospheric correction of thermal-infrared imagery of the 3-D urban environment acquired in oblique viewing geometry', *Atmospheric Measurement Techniques*, 4(5), pp. 909–922. doi: 10.5194/amt-4-909-2011.

Miller, D. L. *et al.* (2020) 'Drought response of urban trees and turfgrass using airborne imaging spectroscopy', *Remote Sensing of Environment*, 240. doi: 10.1016/j.rse.2020.111646.

Mini, C., Hogue, T. S. and Pincetl, S. (2014) 'Estimation of residential outdoor water use in Los Angeles, California', *Landscape and Urban Planning*, 127, pp. 124–135. doi: 10.1016/j.landurbplan.2014.04.007.

Mitchell, D. *et al.* (2017) *Building Drought Resilience in California's Cities and Suburbs*, *Public Policy Institute of California*. doi: 10.13140/RG.2.2.12398.41288.

Morrison, W. *et al.* (2020) 'Atmospheric and emissivity corrections for ground-based thermography using 3D radiative transfer modelling', *Remote Sensing of Environment*, 237(September 2019), p. 111524. doi: 10.1016/j.rse.2019.111524.

Morrison, W., Kotthaus, S. and Grimmond, S. (2021) 'Urban surface temperature observations from ground-based thermography: intra- and inter-facet variability', *Urban Climate*, 35(November 2020), p. 100748. doi: 10.1016/j.uclim.2020.100748.

Norton, B. A. *et al.* (2015) 'Planning for cooler cities: A framework to prioritise green infrastructure to mitigate high temperatures in urban landscapes', *Landscape and Urban Planning*, 134, pp. 127–138. doi: 10.1016/j.landurbplan.2014.10.018.

Nowak, D. J. *et al.* (2011) *Assessing Urban Forest Effects and Values: Los Angeles' Urban Forest*. Available at: http://www.srs.fs.usda.gov/pubs/37671.

Oke, T. R. (1982) 'The energetic basis of the urban heat island', *Quarterly Journal of the Royal Meteorological Society*, 108, pp. 1–30.

Oke, T. R. (1987) *Boundary Layer Climates*. Routledge Books. doi: 10.1017/CBO9781107415324.004.

Oke, T. R. (1988) ‘Street design and urban canopy layer climate’, *Energy and Buildings*, 11(1–3), pp. 103–113. doi: 10.1016/0378-7788(88)90026-6.

Oke, T. R. *et al.* (1989) ‘The Micrometeorology of the Urban Forest’, *Philosophical Transactions of the Royal Society of London*, B324, pp. 335–349.

Oke, T. R. *et al.* (2017) *Urban Climates*. Cambridge University Press. doi: 10.1177/030913338400800101.

Palazzo, J. *et al.* (2017) ‘Urban responses to restrictive conservation policy during drought’, *Water Resources Research*, 53(5), pp. 4459–4475. doi: 10.1002/2016WR020136.

Palmer, W. C. (1965) ‘Meteorological Drought’, *U.S. Weather Bureau, Res. Pap. No. 45*, p. 58. Available at: https://www.ncdc.noaa.gov/temp-and-precip/drought/docs/palmer.pdf.

Pincetl, S. *et al.* (2019) ‘Landscape and Urban Planning Evaluating the effects of turf-replacement programs in Los Angeles’, *Landscape and Urban Planning*, 185(February), pp. 210–221. doi: 10.1016/j.landurbplan.2019.01.011.

Qian, Y. and Fry, J. D. (1997) ‘Water relations and drought tolerance of four turfgrasses’, *Journal of the American Society for Horticultural Science*, pp. 129–133. doi: 10.21273/jashs.122.1.129.

Quesnel, K. J. and Ajami, N. K. (2019) ‘Large Landscape Urban Irrigation: A Data-Driven Approach to Evaluate Conservation Behavior’, *Water Resources Research*, 55(1), pp. 771–786. doi: 10.1029/2018WR023549.

Quesnel, K. J., Ajami, N. and Marx, A. (2019) ‘Shifting landscapes: decoupled urban irrigation and greenness patterns during severe drought’, *Environmental Research Letters*, 14(6), p. 064012. doi: 10.1088/1748-9326/ab20d4.

Reyes, B. *et al.* (2020) ‘Urban irrigation in the modeling of a semi-arid urban environment : Ballona Creek watershed , Los Angeles , California’, *Hydrological Sciences Journal*, 65(8), pp. 1344–1357. doi: 10.1080/02626667.2020.1751846.

Reyes, B., Hogue, T. and Maxwell, R. (2018) ‘Urban irrigation suppresses land surface temperature and changes the hydrologic regime in semi-arid regions’, *Water*, 10(11). doi: 10.3390/w10111563.

Roberts, D. A. *et al.* (1998) ‘Mapping chaparral in the Santa Monica Mountains using multiple endmember spectral mixture models’, *Remote Sensing of Environment*, 65(3), pp. 267–279. doi: 10.1016/S0034-4257(98)00037-6.

Roberts, D. A. *et al.* (2015) ‘Relationships between dominant plant species, fractional cover and Land Surface Temperature in a Mediterranean ecosystem’, *Remote Sensing of Environment*, 167, pp. 152–167. doi: 10.1016/j.rse.2015.01.026.

Roberts, D. A., Smith, M. O. and Adams, J. B. (1993) ‘Green vegetation, nonphotosynthetic

vegetation, and soils in AVIRIS data', *Remote Sensing of Environment*, 44(2–3), pp. 255–269. doi: 10.1016/0034-4257(93)90020-X.

Rose, L. S. and Levinson, R. (2013) 'Analysis of the effect of vegetation on albedo in residential areas: Case studies in suburban Sacramento and Los Angeles, CA', *GIScience and Remote Sensing*, 50(1), pp. 64–77. doi: 10.1080/15481603.2013.778557.

Roth, M., Oke, T. R. and Emery, W. (1989) 'Satellite-derived urban heat islands from three coastal cities and the utilization of such data in urban climatology.', *International Journal of Remote Sensing*, 10(11), pp. 1699–1720. doi: http://dx.doi.org/10.1080/01431168908904002.

Sailor, D. J. (1995) 'Simulated Urban Climate Response to Modifications in Surface Albedo and Vegetative Cover', *Journal of Applied Meteorology*, 34(7), pp. 1694–1704. doi: 10.1175/1520-0450-34.7.1694.

Schwarz, N. *et al.* (2012) 'Relationship of land surface and air temperatures and its implications for quantifying urban heat island indicators - An application for the city of Leipzig (Germany)', *Ecological Indicators*, 18, pp. 693–704. doi: 10.1016/j.ecolind.2012.01.001.

Shashua-Bar, L., Pearlmutter, D. and Erell, E. (2011) 'The influence of trees and grass on outdoor thermal comfort in a hot-arid environment', *International Journal of Climatology*, 31(10), pp. 1498–1506. doi: 10.1002/joc.2177.

Shivers, S. W. *et al.* (2018) 'Using imaging spectrometry to study changes in crop area in California's Central Valley during Drought', *Remote Sensing*, 10(10). doi: 10.3390/rs10101556.

Silvestri, M. *et al.* (2020) 'First comparisons of surface temperature estimations between ECOSTRESS, ASTER and landsat 8 over Italian volcanic and geothermal areas', *Remote Sensing*, 12(1), pp. 1–11. doi: 10.3390/RS12010184.

Sismanidis, P. *et al.* (2016) 'Assessing the Capability of a Downscaled Urban Land Surface Temperature Time Series to Reproduce the Spatiotemporal Features of the Original Data', *Remote Sensing*, 8(4), p. 274. doi: 10.3390/rs8040274.

Sismanidis, P. *et al.* (2017) 'Improving the downscaling of diurnal land surface temperatures using the annual cycle parameters as disaggregation kernels', *Remote Sensing*, 9(1), pp. 1–20. doi: 10.3390/rs9010023.

Sismanidis, P., Keramitsoglou, I. and Kiranoudis, C. T. (2015) 'A satellite-based system for continuous monitoring of Surface Urban Heat Islands', *Urban Climate*, 14, pp. 141–153. doi: 10.1016/j.uclim.2015.06.001.

Sobrino, J. A. *et al.* (2012) 'Impact of spatial resolution and satellite overpass time on evaluation of the surface urban heat island effects', *Remote Sensing of Environment*, 117, pp. 50–56. doi: 10.1016/j.rse.2011.04.042.

Soux, A., Voogt, J. A. and Oke, T. R. (2004) ‘A model to calculate what a remote sensor “sees” of an urban surface’, *Boundary-Layer Meteorology*, 111(1), pp. 109–132. doi: 10.1023/B:BOUN.0000010995.62115.46.

Still, C. J. *et al.* (2021) ‘Imaging canopy temperature: shedding (thermal) light on ecosystem processes’, *New Phytologist*. doi: 10.1111/nph.17321.

Stoll, M. J. and Brazel, A. J. (1992) ‘Surface-air temperature relationship in the urban environment of Phoenix, Arizona’, *Physical Geography*, 13(2), pp. 160–179. doi: 10.1080/02723646.1992.10642451.

Tane, Z. *et al.* (2018) ‘A framework for detecting conifer mortality across an ecoregion using high spatial resolution spaceborne imaging spectroscopy’, *Remote Sensing of Environment*, 209(March), pp. 195–210. doi: 10.1016/j.rse.2018.02.073.

United Nations (2014) *World Urbanization Prospects: The 2014 Revision*. New York City, United States of America. doi: 10.4054/DemRes.2005.12.9.

Vahmani, P. and Ban-Weiss, G. (2016) ‘Climatic consequences of adopting drought-tolerant vegetation over Los Angeles as a response to California drought’, *Geophysical Research Letters*, 43(15), pp. 8240–8249. doi: 10.1002/2016GL069658.

Vahmani, P. and Hogue, T. S. (2015) ‘Urban irrigation effects on WRF-UCM summertime forecast skill over the Los Angeles metropolitan area’, *Journal of Geophysical Research: Atmospheres*, 120(19), pp. 9869–9881. doi: 10.1002/2015JD023239.

Voogt, J. A. (2000) ‘Image Representations of Complete Urban Surface Temperatures’, *Geocarto International*, 15(3), pp. 21–32. doi: 10.1080/10106040008542160.

Voogt, J. A. (2008) ‘Assessment of an Urban Sensor View Model for thermal anisotropy’, *Remote Sensing of Environment*, 112(2), pp. 482–495. doi: 10.1016/j.rse.2007.05.013.

Voogt, J. A. and Oke, T. R. (1998a) ‘Effects of urban surface geometry on remotely-sensed surface temperature’, *International Journal of Remote Sensing*, 19(February 2015), pp. 895–920. doi: 10.1080/014311698215784.

Voogt, J. A. and Oke, T. R. (1998b) ‘Radiometric temperatures of urban canyon walls obtained from vehicle traverses’, *Theoretical and Applied Climatology*, 60(1–4), pp. 199–217. doi: 10.1007/s007040050044.

Voogt, J. A. and Oke, T. R. (2003) ‘Thermal remote sensing of urban climates’, *Remote Sensing of Environment*, 86(3), pp. 370–384. doi: 10.1016/S0034-4257(03)00079-8.

Weng, Q. (2009) ‘Thermal infrared remote sensing for urban climate and environmental studies: Methods, applications, and trends’, *ISPRS Journal of Photogrammetry and Remote Sensing*, 64(4), pp. 335–344. doi: 10.1016/j.isprsjprs.2009.03.007.

Weng, Q. and Fu, P. (2014) ‘Modeling diurnal land temperature cycles over Los Angeles

using downscaled GOES imagery', *ISPRS Journal of Photogrammetry and Remote Sensing*, 97, pp. 78–88. doi: 10.1016/j.isprsjprs.2014.08.009.

Weng, Q., Lu, D. and Schubring, J. (2004) 'Estimation of land surface temperature-vegetation abundance relationship for urban heat island studies', *Remote Sensing of Environment*, 89(4), pp. 467–483. doi: 10.1016/j.rse.2003.11.005.

Wetherley, E. B. (2018) *Remote Sensing of Urban Climate and Vegetation in Los Angeles*. University of California Santa Barbara.

Wetherley, E. B. *et al.* (2021) 'Remote sensing and energy balance modeling of urban climate variability across a semi-arid megacity', *Urban Climate*, 35(December 2020), p. 100757. doi: 10.1016/j.uclim.2020.100757.

Wetherley, E. B., McFadden, J. P. and Roberts, D. A. (2018) 'Megacity-scale analysis of urban vegetation temperatures', *Remote Sensing of Environment*, 213(April), pp. 18–33. doi: 10.1016/j.rse.2018.04.051.

Wetherley, E. B., Roberts, D. A. and McFadden, J. P. (2017) 'Mapping spectrally similar urban materials at sub-pixel scales', *Remote Sensing of Environment*, 195, pp. 170–183. doi: 10.1016/j.rse.2017.04.013.

Yan, J., Zhou, W. and Jenerette, G. D. (2019) 'Testing an energy exchange and microclimate cooling hypothesis for the effect of vegetation configuration on urban heat', *Agricultural and Forest Meteorology*, 279(May), p. 107666. doi: 10.1016/j.agrformet.2019.107666.

Yang, J. *et al.* (2021) 'Assessing the impact of urban geometry on surface urban heat island using complete and nadir temperatures', *International Journal of Climatology*, 41(S1), pp. E3219–E3238. doi: 10.1002/joc.6919.

Zhang, X. *et al.* (2004) 'The footprint of urban climates on vegetation phenology', *Geophysical Research Letters*, 31(12), pp. 10–13. doi: 10.1029/2004GL020137.

Zhao, L. *et al.* (2014) 'Strong contributions of local background climate to urban heat islands', *Nature*, 511(7508), pp. 216–219. doi: 10.1038/nature13462.

Zhao, L. *et al.* (2018) 'Interactions between urban heat islands and heat waves', *Environmental Research Letters*, 13(3). doi: 10.1088/1748-9326/aa9f73.

Zhou, D. *et al.* (2019) 'Satellite remote sensing of surface urban heat islands: Progress, challenges, and perspectives', *Remote Sensing*, 11(1), pp. 1–36. doi: 10.3390/rs11010048.

Zhou, J. *et al.* (2013) 'Modelling the diurnal variations of urban heat islands with multi-source satellite data', *International Journal of Remote Sensing*, 34(21), pp. 7568–7588. doi: 10.1080/01431161.2013.821576.